UNIVERSITY OF CALIFORNIA

Los Angeles

Designing Novel Catalysts to Convert Green House Gas to Value-added Fuels and Feedstocks

A dissertation submitted in partial satisfaction of the

requirements for the degree Doctor of Philosophy

in Materials Science and Engineering

by

Chungsuk Choi

2020

ABSTRACT OF THE DISSERTATION

Designing Novel Catalysts to Convert Green House Gas to Value-added Fuels and Feedstocks

by

Chungsuk Choi

Doctor of Philosophy in Materials Science and Engineering

University of California, Los Angeles, 2020

Professor Yu Huang, Chair

Developing high-efficient catalysts for carbon dioxide reduction reaction (CO_2RR) to value-added fuels and chemicals could dissolve humanity facing problems of shortage of renewable energy sources and global climate change because of upwards of CO_2 emission from human activity.

The electrochemical approach is the easiest and cost-effective method for CO_2RR. Copper (Cu) is the only material to utilize electrochemical CO_2RR to potential fuels and hydrocarbons (especially methane (CH_4) and ethylene (C_2H_4)). However, a mixture of primary products, competition with hydrogen evolution reaction (HER), and high overpotential of CO_2RR from monometallic Cu is still challenging to develop high selectivity of Cu catalysts at less applied potentials. Surface defects have been considered the most attractive electrochemical CO_2RR since

grain boundaries (GBs) exhibited 2.5 times higher CO_2RR activity with a less competitive reaction (HER).

Thus, I have focused on designing and understanding high-efficiency electrochemical Cu catalysts having surface defects as active sites for CO_2RR. I designed two types of Cu-based catalysts; multi-twined nanoparticles (NPs) and Cu nanowires (NWs) with surface steps, which successfully develop CO_2RR performance. Electrochemical and other materials spectroscopies characterized the property of defect structures on the surface of catalysts. This research set improved the status of high-efficiency electrochemical catalysts for CO_2RR and developed the understanding of the effects of surface defect on CO_2RR.

The dissertation of Chungsuk Choi is approved.

Xiangfeng Duan

Yong Chen

Jaime Marian

Yu Huang, Committee Chair

University of California, Los Angeles

2020

Dedicated to my family

Kyung A Shin, Felicity (Eunseo) Choi, and Philip (Eunwoo) Choi

Table of Contents

List of Figures

List of Tables

Acknowledgements

I am pleased to write down acknowledgments for Ph.D. dissertation works at UCLA. Many things have been passing over my mind at this moment. The whole time for pursuing a Ph.D. degree at UCLA is so valuable and memorable in my life. It is unbelievable that I have finally been coming to a stage to complete my Ph.D. diploma. I would like to appreciate all advisors and peers who cooperate to finish up the dissertation works together.

First and foremost, I would like to sincerely express my appreciation to my graduate advisor " Prof. Yu Huang". I have believe that my dissertation works could not complete without great scientific advice and support from Prof. Yu Huang. I have always felt that my scientific capability has been growing under her guidance and insight. Her great scientific vision and understanding still inspire me to keep improving my scientific perspective and capacity. One of the most valuable things in my Ph.D. is that I joined Prof. Yu Huang's group and have taken research under Prof. Yu Huang's advice.

I am very thankful for Prof. Xiangfeng Duan's advice during the Ph.D. process. I have learned the attitude and sense of a scientist from his advice. He has especially provoked me to develop ways to move forward my research and develop a scientific idea. His scientific comments and advice could be more valuable in my future research life.

I genuinely appreciate Prof. William B Goddard in Caltech. I have admired his passion and insight into "science". I thank the chances to study computational theory with his invaluable advice in WAG group. Prof. William B Goddard has taught me a lot about how to learn "theory".

I would like to thank Prof. Yong Chen and Prof. Jaime Marian for being my committee members. Their guidance and comments for my dissertation works played an important role in finishing the dissertation up.

I also thank Dr. Soonho Kwon and Dr. Tao Cheng for contributing to quantum mechanics theory and writing computational parts in the dissertation. Without cooperation with them, I could not complete my dissertation works.

I have to thank Dr. Changsoo Lee, Dr. Huilong Fei, Dr. Michelle Flores Espinosa, and Dr. Jin Cai for contributing to my dissertation works.

I also thank Dr. Mingjie Xu and Dr. Peter Tieu for their help to obtain STEM and SEI images.

I cannot miss saying thank all group members and friends I have met at UCLA. They have filled value in the most crucial time in my life ever together.

Lastly, I appreciate John Wiley and Sons ("John Wiley and Sons") and “Springer Nature” for provided copyright to reproduce published papers into my dissertation thesis. Chapter two is a reproduced version of “*A Highly Active Star Decahedron Cu Nanocatalyst for Hydrocarbon Production at Low Overpotentials*” Chungseok Choi, Tao Cheng, Michelle Flores Espinosa, Huilong Fei, Xiangfeng Duan, William A Goddard III, Yu Huang Advanced Materials 31(6), 2019, 1805405 (https://doi.org/10.1002/adma.201805405).

“This Agreement between Dr. Chungsuk Choi ("You") and John Wiley and Sons ("John Wiley and Sons") consists of your license details and the terms and conditions provided by John Wiley and Sons and Copyright Clearance Center. License Number: 4942600877139 License date: Nov 05, 2020”

Chapter three is a reproduced version of "Highly Active and Stable Stepped Cu Surface for Enhanced Electrochemical CO_2 Reduction to C_2H_4" Chungseok Choi, Soonho Kwon, Tao Cheng, Mingjie Xu, Peter Tieu, Changsoo Lee, Jin Cai, Hyuck Mo Lee, Xiaoqing Pan, Xiangfeng Duan, William A Goddard III, Yu Huang Nature Catalysis 3(10), 2020, 804-812 (10.1038/s41929-020-00504-x).

"Nature Catalysis Publisher: Springer Nature, Date: Sep 7, 2020, Ownership of copyright in original research articles remains with the Author, and provided that, when reproducing the contribution or extracts from it or from the Supplementary Information, the Author acknowledges first and reference publication in the Journal."

VITA

2009 B.S. Materials Science and Engineering, Hanyang University, Republic of Korea
2011 M.S. Materials Science and Engineering, Korea Advanced Institute of Science and Technology (KAIST), Republic of Korea

PUBLICATIONS

1. Michelle M Flores Espinosa, Tao Cheng, Mingjie Xu, Luca Abatemarco, **Chungseok Choi**, Xiaoqing Pan, William A Goddard III, Zipeng Zhao, Yu Huang "Compressed Intermetallic PdCu for Enhanced Electrocatalysis" ***ACS Energy Letters*** *5 (2020) 3672 (https://doi.org/10.1021/acsenergylett.0c01959)*

2. Jin-Wook Lee, Shaun Tan, Tae-Hee Han, Rui Wang, Lizhi Zhang, Changwon Park, Mina Yoon, **Chungseok Choi**, Mingjie Xu, Michael E Liao, Sung-Joon Lee, Selbi Nuryyeva, Chenhui Zhu, Kenny Huynh, Mark S Goorsky, Yu Huang, Xiaoqing Pan, Yang Yang "Solid-phase hetero epitaxial growth of α-phase formamidinium perovskite" ***Nature communications*** *11 (2020) 1 (https://doi.org/10.1038/s41467-020-19237-3)*

3. **Chungseok Choi,** Soonho Kwon, Tao Cheng, Mingjie Xu, Peter Tieu, Changsoo Lee, Jin Cai, Hyuck Mo Lee, Xiaoqing Pan, Xiangfeng Duan, William A Goddard III, Yu Huang "Highly Active and Stable Stepped Cu Surface for Enhanced Electrochemical CO_2 Reduction to C_2H_4" ***Nature Catalysis*** *3 (2020) 804 (10.1038/s41929-020-00504-x)*

4. Tae-Hee Han, Jin-Wook Lee, Yung Ji Choi, **Chungseok Choi**, Shaun Tan, Sung-Joon Lee, Yepin Zhao, Yu Huang, Dongho Kim, Yang Yang "Surface-2D/Bulk-3D Heterophased Perovskite Nanograins for Long-Term-Stable Light-Emitting Diodes" ***Advanced Materials*** *32 (2020) 1905674* (https://doi.org/10.1002/adma.201905674)

5. Kim, Dong Hoe, Christopher P. Muzzillo, Jinhui Tong, Axel F. Palmstrom, Bryon W. Larson, **Chungseok Choi**, Steven P. Harvey, Stephen Glynn, James B. Whitaker, Fei Zhang, Zhen Li, Haipeng Lu, Maikel F.A.M. van Hest, Joseph J. Berry, Lorelle M. Mansfield, Yu Huang, Yanfa Yan and Kai Zhu, "Bimolecular Additives Improve Wide-Band-Gap Perovskites for Efficient Tandem Solar Cells with CIGS." ***Joule*** 3 *(2019)* 1734-1754 (https://doi.org/10.1016/j.joule.2019.04.012)

6**.**Tae-Hee Han, Jin-Wook Lee, **Chungseok Choi**, Shaun Tan, Changsoo Lee, Yepin Zhao, Zhenghong Dai, Nicholas De Marco, Sung-Joon Lee, Sang-Hoon Bae, Yonghai Yuan, Hyuck Mo Lee, Yu Huang, Yang Yang "Perovskite-polymer composite cross-linker approach for highly-stable and efficient perovskite solar cells" ***Nature Communications*** *10 (2019) 1-10* (https://www.nature.com/articles/s41467-019-08455-z)

7. **Chungseok Choi**, Tao Cheng, Michelle Flores Espinosa, Huilong Fei, Xiangfeng Duan, William A Goddard III, Yu Huang "A Highly Active Star Decahedron Cu Nanocatalyst for Hydrocarbon Production at Low Overpotentials" ***Advanced Materials*** *(2019) 1805405* (https://doi.org/10.1002/adma.201805405)

8. Jin-Wook Lee, Zhenghong Dai, Tae-Hee Han, **Chungseok Choi**, Sheng-Yung Chang, Sung-Joon Lee, Nicholas De Marco, Hongxiang Zhao, Pengyu Sun, Yu Huang, Yang Yang "2D perovskite stabilized phase-pure formamidinium perovskite solar cells" ***Nature Communications*** *9 (2018) 3021*(https://www.nature.com/articles/s41467-018-05454-4)

9**. Chung Seok Choi**, Sang Chul Yeo, Dowan Kim, Jongchae Kim, Hyuck Mo Lee and Kyungdong Yoo "Study of Shallow Backside Junctions for Backside Illumination of CMOS Image Sensors" ***Journal of Electronic Materials*** *43 (2014) 3933 (*http://link.springer.com/article/10.1007/s11664-014-3336-6)

10. **Chung Seok Choi**, Young Uk Park, Hyungsub Kim, Narae Kim, Kisuk Kang, and Hyuck Mo Lee "Three Dimensional Sponge-Like Architectured Cupric Oxides as High-Power and Long-Life Anodes for Lithium Rechargeable Batteries" ***Electrochimica Acta*** *70 (2012) 98* (http://dx.doi.org/10.1016/j.electacta.2012.03.037)

11. **Chung Seok Choi**, Yun Hwan Jo, Min Gyu Kim, and Hyuck Mo Lee "Control of Chemical Kinetics for Sub-10 nm Cu Nanoparticles to Fabricate Highly Conductive Ink below 150°C" ***Nanotechnology*** *23 (2012) 065601(* http://stacks.iop.org/Nano/23/065601)

12. Yun Hwan Jo, Inyu Jung, **Chung Seok Choi**, Inyoung Kim, and Hyuck Mo Lee "Synthesis and Characterization of Low Temperature Sn Nanoparticles for the Fabrication of Highly Conductive Ink" ***Nanotechnology*** *22 (2011) 225701* (doi:10.1088/0957-4484/22/22/225701)

1 Chapter 1. Introduction

1.1 Importance of CO_2 Reduction Reaction(CO_2RR)

1.1.1 Global warming

Global warming has been one of the detrimental reasons for Earth's climate changes. Since the emergence of the industrial period, ever-rising fossil fuel consumption by human actives has aggravated global warming because of heating trapping by greenhouse gas in Earth's atmosphere. The estimated carbon dioxide level is rose from 280 ppm to 450 ppm in the atmosphere since the pre-industrial levels period (between 1850 and 1900)[1], inducing an increased global temperature by about 1 degree Celsius. Besides, enhanced human activities with greenhouse gas emissions like CO_2 have chronically increased global temperature by 0.2 degrees Celsius per decade.

Global warming has induced environmental disasters on Earth, including acidic oceans, weather changes, and higher sea levels, and so on. By emitting more CO_2 gas in the atmosphere, the ocean's pH level has been more acidic because of the acidification of water with CO_2 gas. The underwater life and marine ecosystems are under an environmental crisis. Mainly, the ocean's life with calcium carbonate shells or skeletons has been threatened by accelerating acidification. The warmer climate has also changed the climate pattern of Earth. A higher CO_2 level in the atmosphere collects water more, retains moisture longer, and drops water more. Thus, the wet areas have more rain, whereas the dry regions have less rain. The most detrimental effects on Earth's environment from global warming are rising temperature in polar reasons, causing an increase in Earth's sea levels. The measured temperature of the Arctic is increasing twice faster than in other regions, which accelerates the melting of ice sheets. The estimated sea level becomes one to four feet higher in 2100, frightening human society on the island nation and cities.

1.1.2 Alternative fuels

Another humane facing problem is the depletion of energy sources in our society. Fossil fuel accounted for about 85% of the energy source in 2018[2]. Even though fossil fuels continually replenish through natural processes, fossil fuels' consumption rate overwhelms the replenishment rate. The energy consumption rate has been rising faster than before. 2.9% growth rate of energy consumption in the world was reported in 2018[3], which was about double higher than the average growth rate over ten years. Fossil fuels will eventually deplete and become critical issues in 100 years.

The need for alternative fuels has been growing with the expected depletion of fossil fuels. The primary fossil fuels will run out over 50 years. Specifically, the oil, one of the primary energy sources, will be depleted over 53 years. The gas reserver could sustain by 52 years more[4].

Alternative fuels should have no relation to fossil fuels, less greenhouse gas emissions, and be sustainable. There are many candidates for alternative fuels like ethanol, methanol, natural gas, electricity, hydrogen, and propane. Sustainable energy sources like green energy from wind and solar power have been paid more attention to as the ideal alternative fuels.

1.1.3 Carbon recycle loop

Inventing a closed-loop system to recycle CO_2 to value-added fuels is a promising option to mitigate global warming and grant inexhaustible energy sources. The closed-loop system for recycling CO_2 will mimic the natural carbon recycling loop, capturing emitted CO_2, offering clean water and photons or electrons, and a catalyst system for CO_2 conversion. The essential part of the closed-loop system for recycling CO_2 is an effective catalyst to convert the emitted CO_2 gas to

fuels. Electrochemical and photocatalytic methods have been rising to reduce CO_2 to alternative fuels such as ethylene and ethanol.

To reach a cost-competitive carbon recycling loop, all parts of the closing loop should take more steps toward the advanced level. Low-cost CO_2 captured from the flue and following the purification process are essential for consideration of cost. High selectivity for target production and long-term stability ability is a prerequisite for the carbon recycling loops to commercialize the electrochemical CO_2 reduction system.

1.2 Background Information about General Catalyst

1.2.1 Catalysis

Catalysis accelerates the chemical reaction rate by interacting between a catalyst and reactants. The catalysis process reduces the energy of transition states from a high kinetic barrier to a lower kinetic barrier, which improves the possibility for reactants to jump the kinetic barrier. Thus, the catalyst promotes blocked or slowed chemical reactions, changing the reaction path and enhancing the total chemical reaction rate. Figure 1-1 illustrates the catalysis process. Reactants A and B have a reduced energy barrier with catalysts, and then the chemical process accelerates to product C.

The kinetic barriers are mainly related to the enthalpy of reactants, and the enthalpy is bond strength in reactants and pressure change timed volume changes. Therefore, reducing the kinetic barrier means decreasing bond strength in reactants, commonly called “activation state” for catalytic reactions.

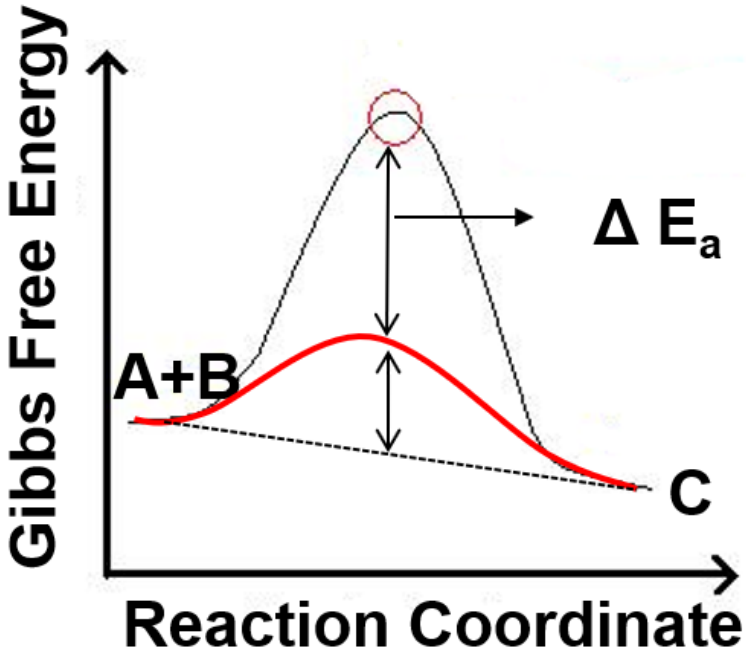

Figure 1-1. Illustration of catalysis mechanism

1.2.2 Activation state of catalysis

"Activation state" is the initial step for catalytic reactions, which relates with changing bonding orders of reactants. Without catalysts, the reactant commonly has a stable chemical structure with a low Gibbs free energy. The activation process begins with the adsorption of reactants on the catalyst's surface in figure 1-2a. The electron transfer from the catalyst to the antibonding orbital of the adsorbed reactant molecule generally increases the reactant's bonding order in figure 1-2b. The bonding order is defined as:

$$\textit{Bonding order} = (\textit{numbers of electrons on bonding state} - \textit{numbers of electrons on antibonding sate})/2 \quad (1\text{-}1)$$

The transferred electron to antibonding orbitals of reactant molecules induces higher bonding order. Thus, the reactant could join the chemical reaction with lower activation barriers due to the reduced bonding energy in the reactant.

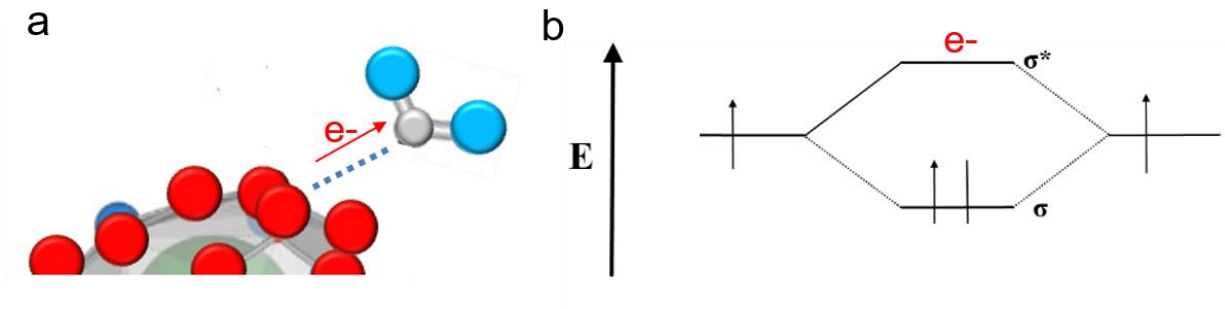

Figure 1-2. Illustration of the activation state of catalysis, a) A schematic of reaction between catalyst and reactant molecule, red is a surface of the catalyst, blue and gray is reactant molecules, b) Reactant orbital diagram after an electron transfer from the catalyst.

1.2.3 Types of catalysts.

Catalysts are categorized into "heterogeneous catalysts" and "homogeneous catalysts." Heterogeneous catalysts have a different phase in comparison with reactants. In general, most of the heterogeneous catalysts are solid phase, which reacts with gas or liquid phase reactants. The active sites on the heterogeneous catalysts are only small areas on the surface of the catalysts. The large active areas are one of the critical factors in the heterogeneous catalysts. Thus, most of the heterogeneous catalysts with high activity are nanomaterials, which have a large surface and volume ratio. Typical heterogeneous catalysis systems are electrochemical catalysts and photosynthesis catalysts.

In contrast, homogeneous catalysts and reactants have the same phase in the catalysis. Commonly, homogeneous catalysts dissolve in solution and react with a reactant in solution. Most parts of catalysts are considered as active sites, providing high contact angles and bonding strength with reactants. Homogenous catalysis systems are typically electrochemical catalysis, photosynthesis, and biocatalysts. Table 1-1 shows the difference between heterogeneous and homogenous catalysts.

Table 1-1. Illustration of the comparison between heterogeneous and homogenous catalysts.

	Heterogeneous Catalysts	**Homogeneous Catalysts**
Definition	Catalysts and reactants have different phases.	Catalysts and reactants have the same different phases.
Cons	1)High separation rate due to weak bonding strength as a result of different phases between catalysts and products 2)High catalyst stability because of no strong adsorption between catalysts and products	1)High efficiency because most parts of catalyst are active sites 2)High selectivity because the active sites are well known; thus, we can easily select products. 3)High activity because of high contact areas and strong bonding
Pros	1)Small active areas and low catalyst efficiency because only parts of the surface are active sites 2)Low selectivity	1)Hard separation due to strong bonding energy 2)Low catalyst stability because the temperature for distillation destroys the catalyst 3)Poisoning by reactants due to strong bonding energy

1.3 Electrochemical CO_2 reduction reaction

1.3.1 Challenging in electrochemical CO_2 reduction reactions

CO_2 is one of the stablest carbon-based molecules at room temperature and atmospheric pressure because the CO_2 molecule has a linear nonpolar structure, closed-shell structure, low repulsive charges, and fully oxidized state of carbon. The stable CO_2 molecule structure causes most CO_2 reduction reactions to be thermodynamically unfavorable with positive free energy in table 1-2. Some CO_2 reduction reactions have a thermodynamically favorable process with negative free energy. The many electron transfer and protonation steps during the electrochemical

CO_2 reduction reaction make other types of problems such as kinetic problems. The kinetic issues could slow down the whole reaction rate. In a worse case, the electrochemical CO_2 reduction reaction is blocked by the kinetic barrier. Thus, many researchers have made efforts to develop electrochemical CO_2RR by handling the thermodynamics and kinetic problems during electrochemical CO_2 reduction reaction. However, more fundamental designing catalysts are still necessary to improve the intrinsic activity and selectivity of CO_2RR.

Table 1-2. Illustration of the thermodynamic CO_2 reduction reaction. Copyright © 1996 Published by Elsevier B.V. "Surface chemistry of carbon dioxide"[5]

	△H°	-T△S°	△G°
$H_2(g)+CO_2(g) \rightarrow CO(g)+H_2O(g)$	41.2	22.6	18.60
$H_2(g)+CO_2(g) \rightarrow CO(g)+H_2O(l)$	-2.80	22.8	20.00
$H_2(g)+CO_2(g) \rightarrow HCOOH$	-31.20	64.2	33.00
$2H_2(g)+CO_2(g) \rightarrow CH_2O(g)+H_2O(l)$	-9.00	55.0	44.00
$3H_2(g)+CO_2(g) \rightarrow CH_3OH(g)+H_2O(l)$	-131.30	122.1	-9.20
$4H_2(g)+CO_2(g) \rightarrow CH_4(g)+2H_2O(l)$	-252.90	122.1	-130.80

1.3.2 Heterogeneous catalysts for electrochemical CO_2 reduction reactions

Several heterogeneous metal catalysts are known to reduce CO_2 in aqueous solutions, which can be classified into two groups: carbon monoxide (CO) production metals (Cu, Au, Ag, Zn, Pd, Ga, Ni, and Pt) and formic acid production metals (Pb, Hg, In, Sn, Cd, and Ti). Cu is the unique heterogeneous metal catalyst to reduce CO_2 toward hydrocarbons or alcohol products with significant activity and efficiency. However, a mixture of primary products, competition with

hydrogen evolution reaction (HER), and high overpotential CO_2RR from monometallic Cu is still challenging to develop less overpotential and high selectivity of Cu catalysts.

1.3.3 Designing copper-based catalysts for electrochemical CO_2 reduction reactions

Developing Cu catalysts have been devoted to modifying structure defects, shapes, size, and chemical states in a decade. Surface defects have been considered as the most attractive sites for electrochemical CO_2RR. Grain boundaries (GBs) exhibited 2.5 times higher CO_2RR activity with a less competitive reaction[6]. Cheng et al. reported that Cu's surface steps having a combination of one strong and one weak CO binding site reduces the *OCCOH formation energy to 0.52 eV[7].

1.4 Motivation and research scope of the dissertation

Developing high-efficient catalysts for CO_2 reduction reaction to value-added fuels and chemicals could dissolve humanity facing problems of shortage of renewable energy sources and global climate change because of upwards of CO_2 emission from human activity. The easiest and cost-effective method for CO_2RR is the electrochemical approach. Even though engineering an electrochemical device for CO_2RR has achieved high efficiencies and long life CO_2RR productions, more fundamental designing catalysts are necessary to improve intrinsic activity and selectivity of CO_2RR further. Cu is the special catalysts to electrochemically reduce CO_2 to potential fuels and hydrocarbons. However, Cu catalysts are still challenging to develop high selectivity at lower overpotential with long-term stability. Many researchers have made efforts to improve the problems of Cu catalysts. Surface defects have been considered as the most attractive sites for electrochemical CO_2RR among the various catalyst design methods.

My research involves inducing structural defects on Cu's surface using solution-based synthesis and an in-situ electrochemical activation process and understanding the effects of the

surface defect on CO_2RR. The dissertation studies experimentally design two types of defective Cu-based catalysts. Multi-twined nanoparticles with stacking faults and stepped surface of Cu nanowires successfully develop CO_2RR performance. In the primary contexts, I studied Cu NPs catalyst and CuNWs by following three categories; 1) synthesis of catalysts decorated with surface defect, 2) measurement of CO_2RR performance, 3) characterize the fundamental mechanism of the developed CO_2RR performance.

1.5 Chapter 1. Reference

[1] Jones, N. “How the World Passed a Carbon Threshold and Why It Matters.” https://e360.yale.edu/features/how-the-world-passed-a-carbon-threshold-400ppm-and-why-it-matters Retrieved 26 January 2017.

[2] BP Statistical Review of World Energy 2019 "Primary energy: consumption by fuel." Retrieved 7 January 2020.

[3] BP Statistical Review of World Energy 2019 "2018 at a glance". Retrieved 7 January 2020.

[4] De Luna, P., Hahn, C., Higgins, D., Jaffer, S. A., Jaramillo, T. F., & Sargent, E. H. What would it take for renewably powered electrosynthesis to displace petrochemical processes? *Science* **364**, 6438 (2019).

[5] Freund, H. J., & Roberts, M. W. Surface chemistry of carbon dioxide. *Surface Science Reports*, **25**, 225-273 (1996).

[6] Mariano, R. G., McKelvey, K., White, H. S., & Kanan, M. W. Selective increase in CO_2 electroreduction activity at grain-boundary surface terminations. *Science* 358, 1187-1192 (2017).

[7] Cheng, T., Xiao, H., & Goddard, W. A. Nature of the active sites for CO reduction on copper nanoparticles; suggestions for optimizing performance. *Journal of the American Chemical Society* **139**, 11642-11645 (2017).

2 Chapter 2. Star Decahedron Cu Nanoparticle (SD-Cu NPs) for CO_2RR

2.1 Introduction

The ever-rising population and fossil fuel consumption present humanity with two major societal challenges: the brink of fossil fuel exhaustion and global climate change. A promising option to mitigate global warming and grant inexhaustible energy sources is to developing materials that efficiently catalyze greenhouse gas to value-added fuels and chemical feedstocks[1-4]. Starting with the pioneering electrochemical CO_2 reduction reaction in aqueous solutions by Hori and co-workers[5], several other materials capable of reducing CO_2 have been identified[6-8].

The most widely used CO_2RR catalysts are copper-based materials, which are the only catalysts shown to produce hydrocarbons (such as CH_4 and C_2H_4) with appreciable reaction rates and efficiency[9-11]. At pH 6.8, electrochemical CO_2RR to CH_4 or C_2H_4 are thermodynamically favorable at 0.17 V and 0.08 V vs. RHE (reversible hydrogen electrode, referenced to all potentials[9]. However, in order to attain high specific activity (SA) and high Faradaic efficiency of CO_2RR, commercial Cu foils and NPs require high applied overpotentials (l >1.0 V l) due to the kinetically sluggish reaction pathways[12]. Unfortunately, such high applied potential also causes Cu electrochemical migration, dissolution, and redeposition that sinter the Cu NPs[10,13].

Thus, developing Cu electrocatalysts for CO_2RR with high selectivity and current density at low overpotentials remains a grand challenge, stimulating great scientific endeavors. Numerous chemical modifications and nano-structuring approaches have led to improvements in product selectivity and catalytic activity[3-5,7,12,14-15]. Since the study showing a linear correlation between grain boundary density and CO_2RR performance by Li et al.[16], grain boundaries have been explored as highly active catalytic sites for both CO_2RR and carbon monoxide reduction (CORR), which promoted the production of CO and formic acid[2,12]. Promotion of C2 production on Cu grain

boundaries has been predicted by Cheng et al, although in Li's studies the production of ethylene is low[17]. Cheng et al. also reported a theoretical study showing that highly active twin boundaries (TBs) on the Au surface can be superior to grain boundaries and other defects for CO_2RR[18]. Hence it would be interesting to realize Cu nanostructures with high TB for CO_2RR.

Multiple-twinned NPs such as icosahedron and star decahedron NPs are ideal structures to provide surface TBs, which have demonstrated enhanced performance in catalytic performance in various reactions[19-25]. Icosahedral and decahedral noble metal NPs (Ag, Au, Pt, and Pd) have been reported[20-25]; however, synthesis of multiple-twinned Cu NPs without rod structure has remained a challenge due to the high reactivity and oxidation tendency of Cu[20,26]. TBs of Cu are more susceptible to oxidation than bulk Cu, leading to the etching of TB-rich NPs during the nucleation stage[20,26]. Another reason for the difficulty of creating Cu TB-rich NPs is the relatively high internal strain energy of Cu compared to Ag and Au because of the relatively high Young's modulus of Cu[27,28].

Herein, I report the synthesis of five-fold twinned star decahedron Cu nanoparticles that greatly enhanced CO_2RR performance compared to commercial Cu NPs. Specifically, SD-Cu NPs showed 0.149 V lower onset potential for CH_4 production compared to commercial Cu NPs, as well as a high FE in the C_2H_4 production of 52.43% at -0.993±0.0129 V compared to 37.08±6.87% at -1.009±0.0113 V for commercial Cu NPs. Quantum Mechanics (QM) calculations suggest that the surface TBs and multiple stacking faults on the surface of the SD-Cu NPs lead to the observed improvement.

2.2 Experimental Section

2.2.1 Preparation of SD-Cu NPs

Copper(II) acetylacetonate ($Cu(acac)_2$, 99.9%), L-Ascorbic acid (> 99%), Oleylamine (OAm) (> 70%), Ethanol (200 proof) were all purchased from Sigma-Aldrich. The deionized (DI) water (18.2 MΩ cm^{-1}) used in aqueous solutions was prepared by using an ultra-pure purification system (Aqua Solutions). I used oleylamine (OAm) as a capping agent and solvent; L-Ascorbic acid serves as a reducing agent, and $Cu(acac)_2$ is the precursor. In a typical synthesis of SD-Cu NPs catalyst, $Cu(acac)_2$ (11 mg), L-Ascorbic acid (52.6 mg) were pre-dissolved in OAm (5 mL) containing 30 ml vial. The mixture was sonicated for 15 min and transferred to an oil bath. The oil bath was heated at 130 °C for 4 h and cooled to room temperature. The synthesized colloidal products were washed five times with hexane/ethanol solvents and collected by centrifuge at 9500 rpm.

2.2.2 Materials characterizations

TEM samples were prepared by dropping and drying ethanol dispersion of catalysts onto carbon-coated copper TEM grids (Ted Pella, Redding, CA) under room temperature. Transmission electron microscopy (TEM) images were taken on an FEI CM120 transmission electron microscope operated at 120 kV. High-resolution TEM images (HRTEM) were carried out on an FEI Titan transmission electron microscope operated at 300 kV. The size of SD-Cu NPs was measured by the longest distance from one corner to one center of the edge. Powder X-ray diffraction (PXRD) patterns were analyzed with a Panalytical X'Pert Pro X-ray Powder Diffractometer with Cu-Kα radiation. Ultraviolet photoelectron spectroscopy (UPS) tests were conducted on Kratos AXIS Ultra DLD spectrometer. To make sure UPS data, we analyzed Cu(100)

foil and d-band of Cu(100), which are well-matched with the d-band shape of Cu(100) foil compared to a published paper[29]; Cu 4s band around 9 eV, d-band starting 1.94 eV below Fermi level, 2.62 d-band widths and higher intensity at the leading edge as included in figure 2-1. The Shirley background was subtracted to calculate the d-band center. The concentration of catalysts was measured by inductively coupled plasma atomic emission spectroscopy (TJA RADIAL IRIS 1000 ICP-AES).

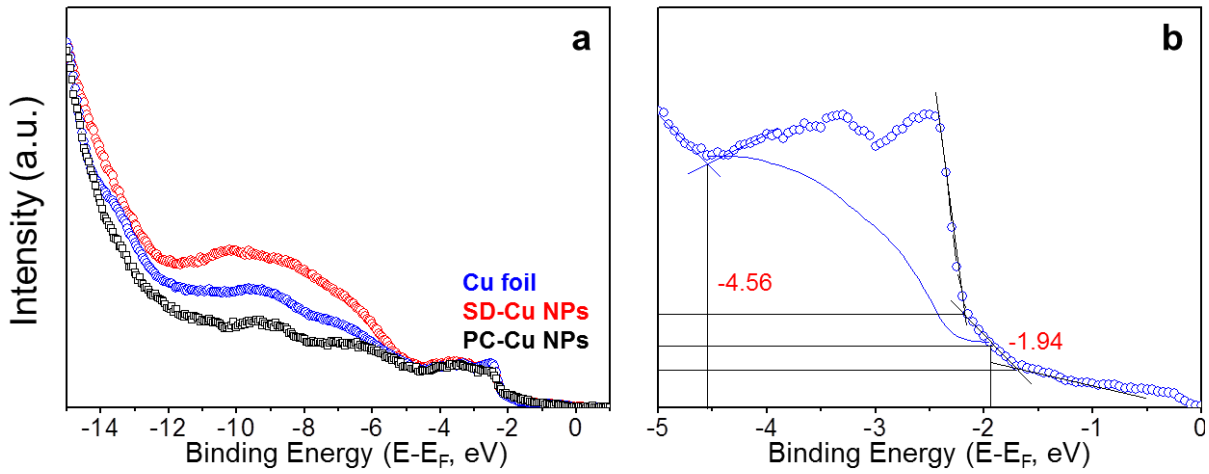

Figure 2-1. (a) Entire UPS spectra measured for Cu(100) foil, SD-Cu NPs, and PC-Cu NPs, (b) D-band spectra of Cu(100) foil.

2.2.3 Electrochemical measurements

Current densities were measured by using a three-electrode cell. A glassy-carbon rotating disk electrode (RDE) (diameter: 5 mm, area: 0.196 cm^2) from Pine Instruments was used as a working electrode. Consumed charges for calculating Faradaic efficiency were collected by using a gas-tight electrolysis H cell (Pine research) separated with anion exchange membrane from Princeton Applied Research VersaSTAT 4 workstation. In a typical setup, 1x1 cm^2 glassy-carbon electrode, Ag/AgCl (1 M KCl) electrode, and Pt wire electrode were used as working, reference,

and counter electrode, respectively. Every electrochemical CO_2RR was conducted with the 0.1 M $KHCO_3$ electrolyte solution. CO_2 (Air gas, 99.999%) was bubbled for 30 minutes before CO_2RR; CO_2 was continuously purged into the cathodic compartment at 10 sccm. Cyclic voltammetry (CV) was performed in CO_2-saturated 0.1 M $KHCO_3$ electrolyte with a potential scan rate of 5 mV s^{-1}. All discussed potentials were converted to those against reversible hydrogen electrode (RHE) after iR corrected during the measurement. The electrochemically active surface area (ECSA) measurements were carried out by Pb under-potential deposition (Pb UPD). The ECSA was determined by subtracting the background current from integrating the Pb desorption charge on the CV at room temperature in nitrogen saturated $HClO_4$ (0.1 M) + $Pb(ClO_4)_2$ solution (0.001 M)[31].

2.2.4 Electrochemical CO_2RR measurements

An outlet gas line from the gas-tight H cell was directly routed to a p-type Hastelloy 6 port sampling loop (1.5 ml). A data point was obtained after applied a constant potential for 35 ± 1 min. 1.5 ml effluence gas was analyzed on Shimadzu Tracera Gas Chromatography Barrier Ionization Discharge (GC-BID) 2010Plus (Shimadzu) equipped with a Restek Micropacked GC column every 35 ± 1 min. The GC-BID detector was calibrated by two standard gases and two different sampling volumes (20 µl and 1.5 ml). Helium was used as the carrier gas (Air gas, 99.9999%). The FE was calculated as below[32]:

$$FE_J = \frac{nFv_J G p_0}{RT_0 i_{total}} \times 100\% \quad (2\text{-}1)$$

where:

n = the number of electrons for a given product.

V_J (vol%) = volume concentration of gas products in the effluence gas from the electrochemical cell (GC data)

G (ml min^{-1} at room temperature and ambient pressure) = Gas flow rate measured by a ProFlow 6000 electronic flow meter (Restek) at the exit of the electrochemical cell

i_{total} (mA) = steady-state cell current

p_0=1.01 x 105 Pa, T_0= 298.15 K, F = 96485 C•mol^{-1}, R = 8.314 J• mol^{-1}• K^{-1}

The liquid product was analyzed by quantitative NMR (Bruker AV-600). For instance, 0.9 mL of the reacted electrolyte was mixed with D_2O (0.1 mL), and 10 μl of dimethyl sulfoxide (25 mM) was added to the mixture as an internal standard. The 1D 1H spectrum was measured with a pre-water saturation method. Densities were measured by using a three-electrode cell. A glassy-carbon rotating disk electrode from Pine Instruments was used as a working electrode. Consumed charges for calculating faradaic efficiency

2.2.5 Computational details

The quantum mechanics calculations were carried out using the VASP software at the version of 5.4.4[33-35], with the Perdew, Burke, and Ernzerhof (PBE) flavor[36] of density functional theory (DFT). The projector augmented wave (PAW) method[37] was used to account for core-valence interactions. The kinetic energy cutoff for plane wave expansions was set to 400 eV, and reciprocal space was sampled by the Γ-centered Monkhorst-Pack scheme with a grid of 3×3×1. The vacuum layer is at least 15 Å above the surface. The convergence criteria are 1×10^{-7} eV energy differences for solving the electronic wave function. The Methfessel-Paxton smearing of second order with a width of 0.1 eV was applied. All geometries (atomic coordinates) were converged to within 1×10^{-2} eV $Å^{-1}$ for maximal components of forces. A post-stage vdW DFT-D3 method with Becke-Jonson damping was applied[38].

The Gibbs free energies were calculated at 298 K and 1 atm as outlined in (2-2):

$$G = H - T \triangle S = E_{DFT} + E_{ZPE} + E_{solv} + \int_0^{298} C_V dT - T \triangle S \quad (2\text{-}2)$$

Where E_{DFT} is the DFT-optimized total energy, E_{ZPE} is the zero-point vibrational energy, E_{solv} is the solvation energy. $\int_0^{298} C_V dT$ is the heat capacity, T is the temperature, and ΔS is the entropy. Gas-phase molecules such as CO were treated using the ideal gas approximation, whereas adsorbents were treated using a harmonic approximation. The solvation was treated implicitly using the CANDLE[39] method using the JDFTx simulation package. The GBRV[40] ultrasoft pseudopotentials (USPP) were used, with a plane wave cutoff of 544 eV (20 a.u.). All other settings are similar to those in VASP calculations.

2.3 Result and Discussion

2.3.1 Synthesis of SD-CuNPs

In our experiments, to reduce the presence of oxygen in the solvent, I heated OAm at 70 °C for 30 min. During colloid nucleation and growth, the twinned seeds are generally preferred at smaller sizes and transform into a single crystal when they grow bigger. Hence slow growth rate and capping agent are typically used to arrest twinned nanostructures during the colloidal growth process[20,29]. To this end, I used a weak reduction agent (L-Ascorbic acid), a low (Cu(II) acetylacetonate) concentration, and a low synthesis temperature (130 °C). When the reaction temperature was increased from 130 °C to 150 °C or 170 °C in figure 2-2, the twinned structures disappear due to a higher growth rate that leads to bigger nanoparticle size and the transformation from the twinned structure to the polycrystalline structure.

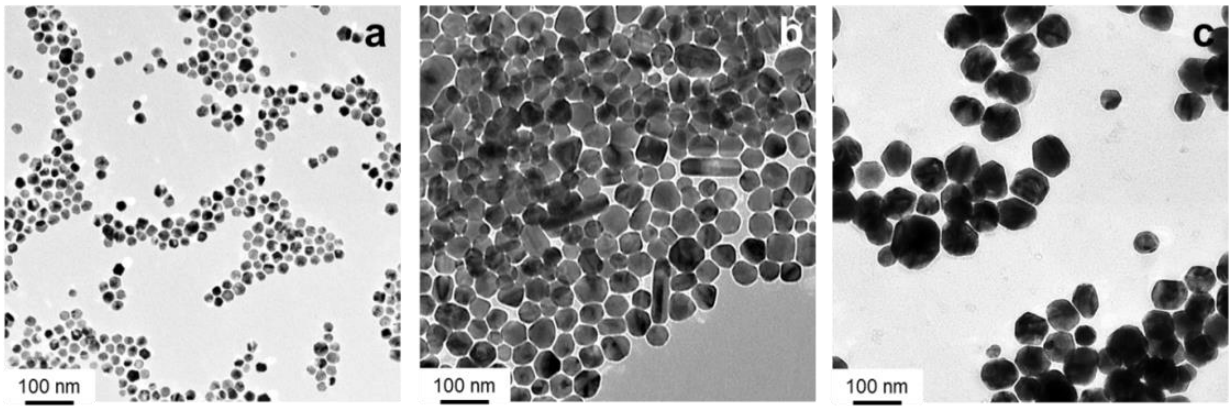

Figure 2-2. Low magnification TEM images of Cu NPs by different reaction temperatures, (a) Synthesis of Cu NPs with Cu $(acac)_2$/oleylamine (0.22 mg/ml) at 130 °C, (b) Synthesis of Cu NPs with Cu $(acac)_2$/oleylamine (0.22 mg/ml) at 150 °C, (c) Synthesis of Cu NPs with Cu $(acac)_2$/oleylamine (0.22 mg/ml) at 170 °C.

2.3.2 Phase and size of SD-Cu NPs

The prepared SD-Cu NPs were characterized by transmission electron microscopy and high-resolution TEM and powder X-ray diffraction. The PXRD patterns of the colloidal products matched with that of the Cu JCPDS (#00-004-0836) in figure 2-3. The average size of the Cu NPs was determined to be 30 nm±1.89 nm, averaging over more than 100 particles in figure 2-4.

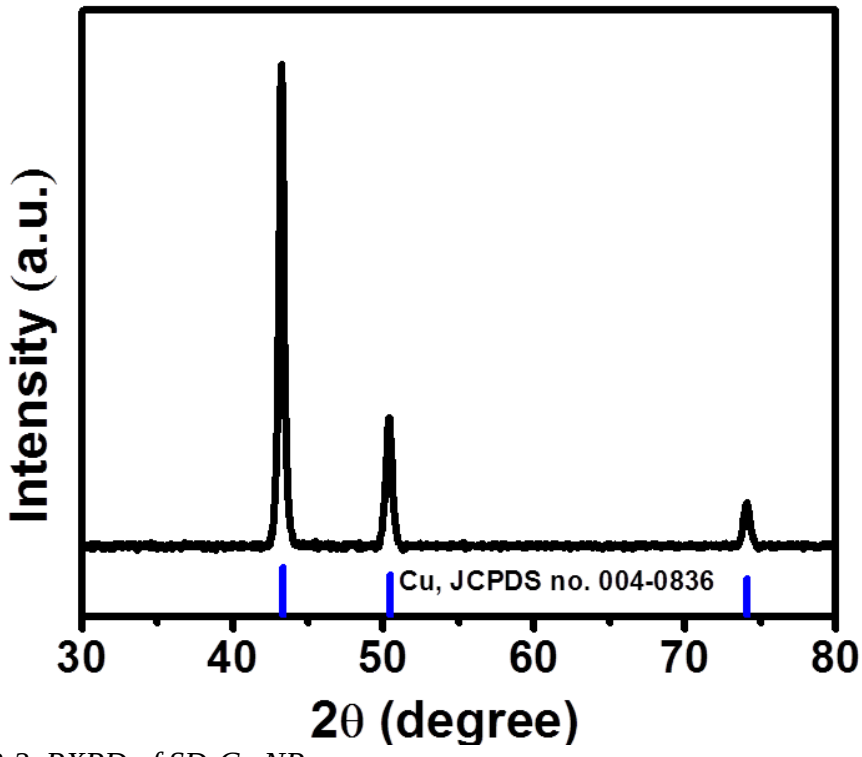

Figure 2-3. PXRD of SD-Cu NPs.

2.3.3 Characterization of SD-Cu NPs by TEM and HRTEM

The HRTEM images show that Cu NPs exhibit a typical star shape with 5-fold TBs crossing the edges of a decahedron in figure 2-5b, c, d[41]. The measured angles between two adjacent TBs are 71.5~72.5°, matching star decahedrons in figure 2-5c, d. The structure of the Cu NPs was further analyzed by fast Fourier transform (FFT)[41]. Within an SD-Cu NP, each TB was denoted OA, OB, OC, OD, and OE, respectively (figure 2-5c, d). The FFT of two typical SD-Cu NPs (figure 2-5c, d) are shown in figure 2-5e and figure 2-5f, respectively.

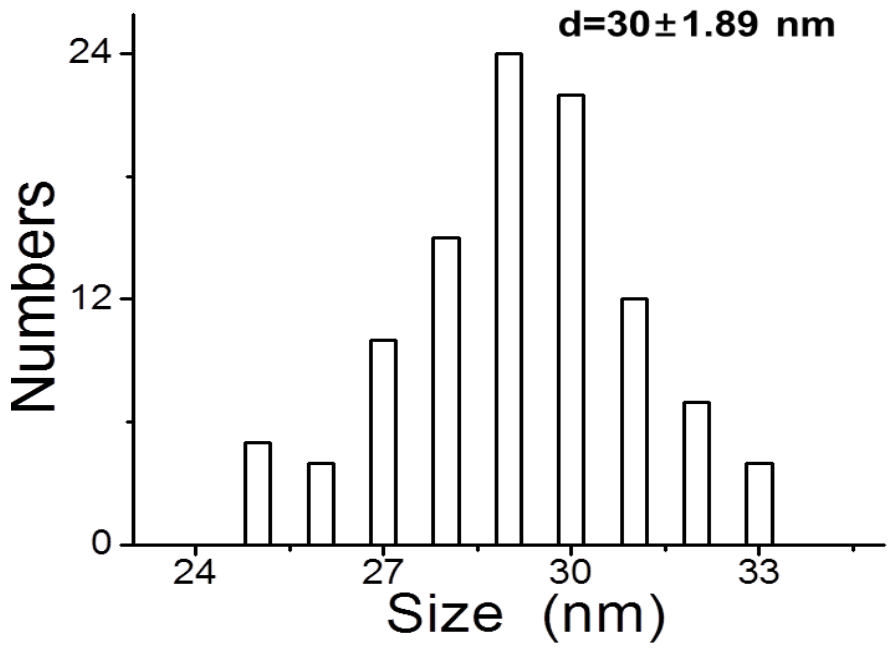

Figure 2-4. Size distribution of SD-Cu NPs.

The FFTs show corresponding five-fold symmetry of {111} spots where A, B, C, D, and E are formed by each OA, OB, OC, OD, and OE TBs. Both HRTEM and FFT images matched well with that of five-fold twinned decahedron structure[42,43]. The complex splitting of FFT spots indicates the formation of bands of twin defects, and the elongation of spots in FFT images suggests steps on the SD-Cu NPs in figure 2-5e, f[42,43]. I also applied inverse FFT at the Bragg spots (B, E) (figure 2-5e) and (A, B, D, and E) (figure 2-5f) on FFT images to generate selectively filtered power spectrum on TBs[44]. The results confirm the bands of thin twin defects observed on HRTEM images (figure 2-5g, h), and the inverse FFT TBs show well-matched angle (figure 2-5g, h) with those in HRTEM (figure 2-5c, d).

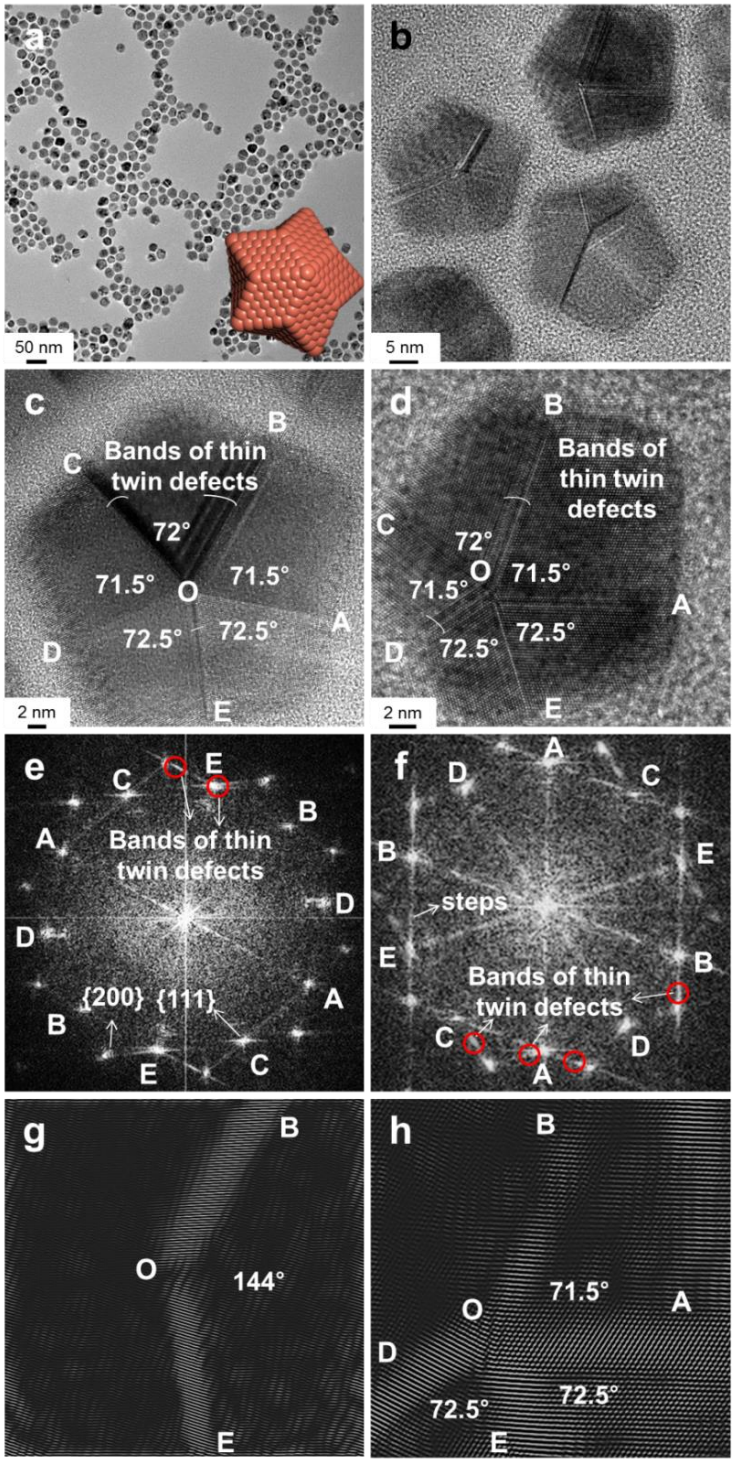

Figure 2-5. (a) Low magnification TEM image of SD-Cu NPs (inset is a schemed atomic structure), (b) HRTEM image of SD-Cu NPs, (c), (d) Fivefold twin symmetry on HRTEM images of SD-Cu

NPs, (e), (f) Fivefold twin symmetry on FFT images of SD-Cu NPs, (g), (h) Inverse FFT of bands of thin twin defects on SD-Cu NPs.

2.3.4 Electrochemical CO_2RR

I studied the CO_2RR performance for these SD-Cu NPs with a gas-tight H cell by analyzing gas and liquid products at different applied potentials between -0.6 and -1.05 V in CO_2 saturated 0.1 M $KHCO_3$ (pH 6.8) at room temperature under atmospheric pressure. 0.01 mg Cu was loaded to the rotating disk electrode and measured by inductively coupled plasma atomic emission spectroscopy to evaluate the current density and the electrochemically active surface area in figure 2-6.

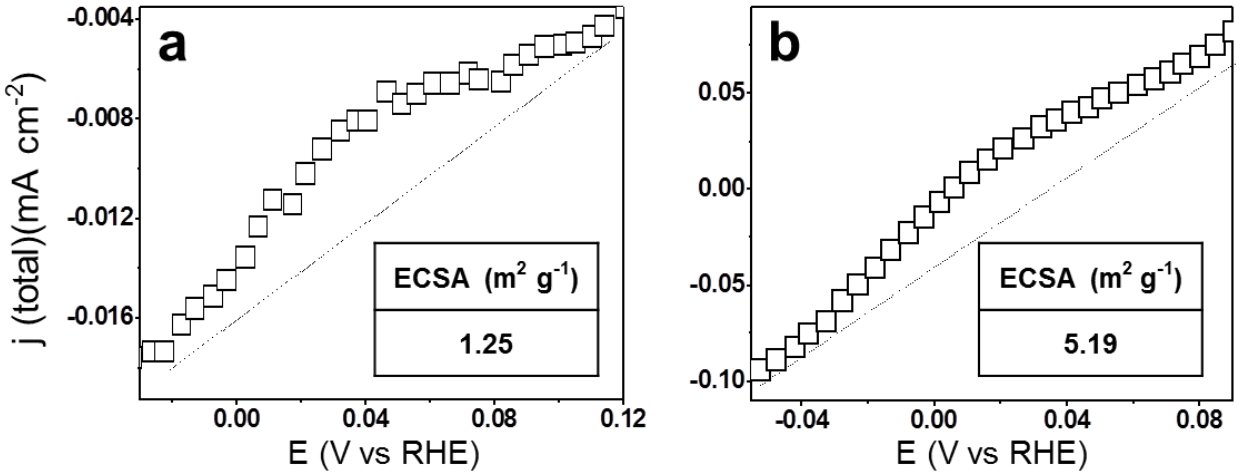

Figure 2-6. Measurement of ECSA by using a Pb under potential method, (a) SD-Cu NPs, (b) PC-Cu NPs.

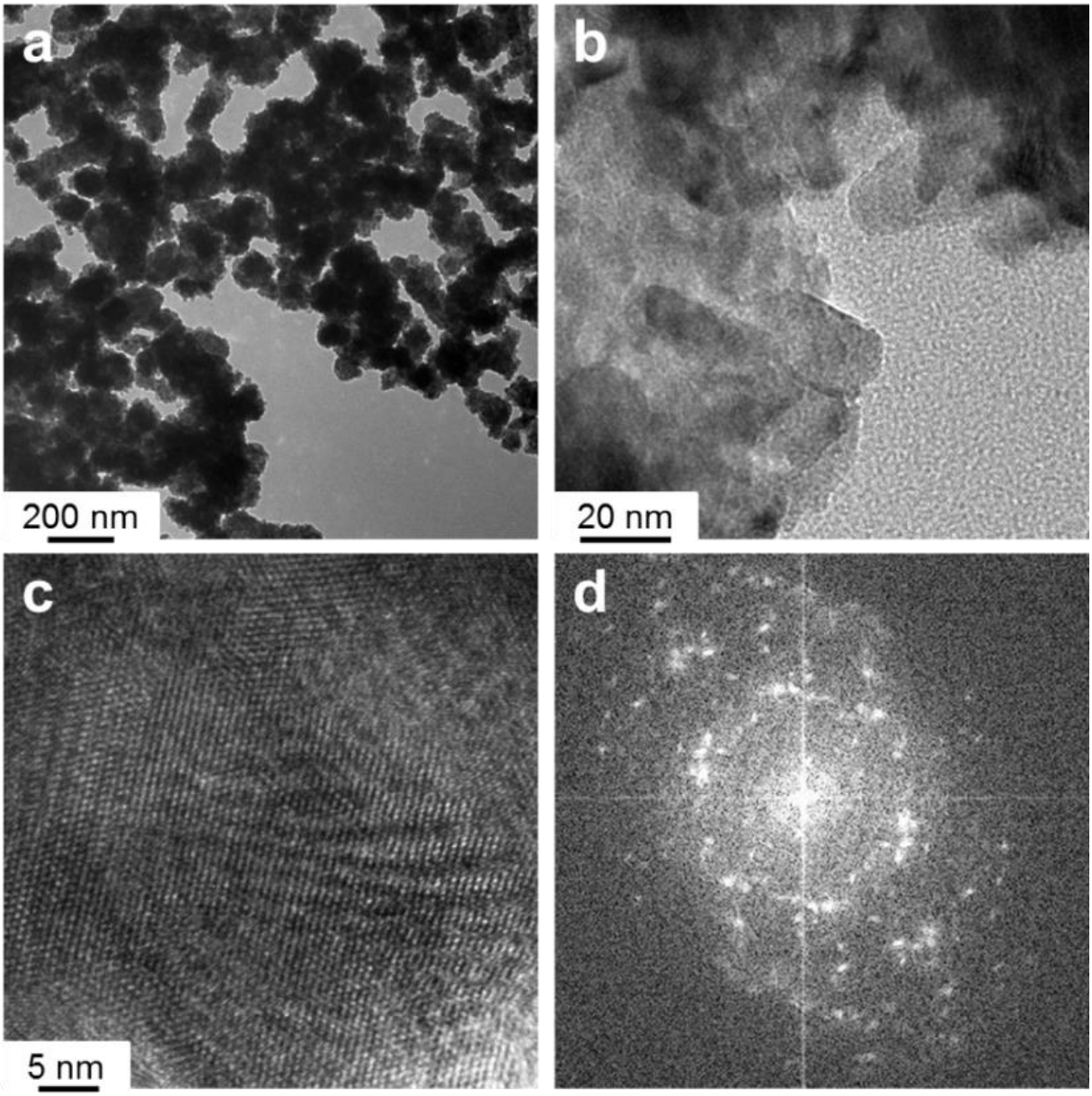

Figure 2-7. Polycrystalline structure of Cu NPs (PC-Cu NPs), (a), (b), (c) TEM images with increasing magnifications, (d) FFT image.

Most products from these reactions were in the gas phase. In general, the SD-Cu NPs showed better performance for CO_2RR than the polycrystalline structure of commercial Cu NPs (PC-Cu NPs in figure 2-7). Figure 2-8a and b show the FE of SD-Cu NPs and PC-Cu NPs,

respectively. The major CO_2RR products from SD-Cu NPs were CH_4 and C_2H_4. Specifically, the formation of CH_4 started at -0.645 V (figure 2-8a, c), and the FE of CH_4 remained below 10% up to -0.98 V (figure 2-8a). At ca. -0.75 V, C_2H_4 formation initiated, with the FE escalating to 50.7% from -0.92 V to -0.98 V (figure 2-8a). The parallel production of C_2H_4 and CH_4 is similar to previously reported observations for a Cu foil[6]. In contrast, C_2H_4 was the primary CO_2RR product from commercial Cu NPs (figure 2-8b), showing 20.90% and 40.92% C_2H_4 produced at -0.93 V and -1.01 V (figure 2-8b), consistent with the CO_2RR performance reported for commercial Cu NPs[45].

Table 2-1. FE for SD-Cu NPs.

V [RHE]	H_2 [%]	CO [%]	CH_4 [%]	C_2H_4 [%]	Ethanol [%]	Acetate [%]	Formate [%]	Total [%]
-0.664 ±0.00594	74.3±11.52	5.5±1.2	3.06±0.56	0	2.5	3.2	2.18	82.86±10.95
-0.759 ±0.00721	82.92±3.61	11.04±1.8	1.94±0.81	1.1±0.144	4.2	2.34	2.78	96.25±5.77
-0.85	58.38	17.03	4	5.56	0.04	0	0.02	84.97
-0.935 ±0.00167	59.93±11.12	16.50±3.51	2.76±1.56	28.42±5.82	0.03	0	0	107.61±6.87
-0.993 ±0.0129	33.47±4.76	6.79 ±3.03	6.58±1.99	52.43±2.72	0	0.5	0	97.63±5.86
-1.029 ±0.0178	29.62±8.8	4.96±2.03	7.81±4.314	51.98±3.72				91.78±10.41

Table 2-2. FE for PC-Cu NPs.

V [RHE]	H_2 [%]	CO [%]	CH_4 [%]	C_2H_4 [%]	Ethanol [%]	Acetate [%]	Formate [%]	Total [%]
-0.662 ±0.0136	80.74±11.78	9.75±1.29	0	0	0	0	8.14	98.63±12.75
-0.749 ±0.009	78.13±5.20	10.92±1.06	0	1.09± 1.89	0.77	0.27	8.25	99.44±7.8
-0.83	80.17	11.93	0	5.91	0	0.46	13	111.47
-0.915 ±0.0128	56.46±3.90	13.60±4.76	0.761 ±0.88	14.21 ±9.88	2.3	1.44	6.3	95.09±11.6
-1.009 ±0.0113	39.08±10.05	8.21±4.83	6.99± 5.15	37.08 ±6.87	2.14	6.54	1.5	101.54± 9.8

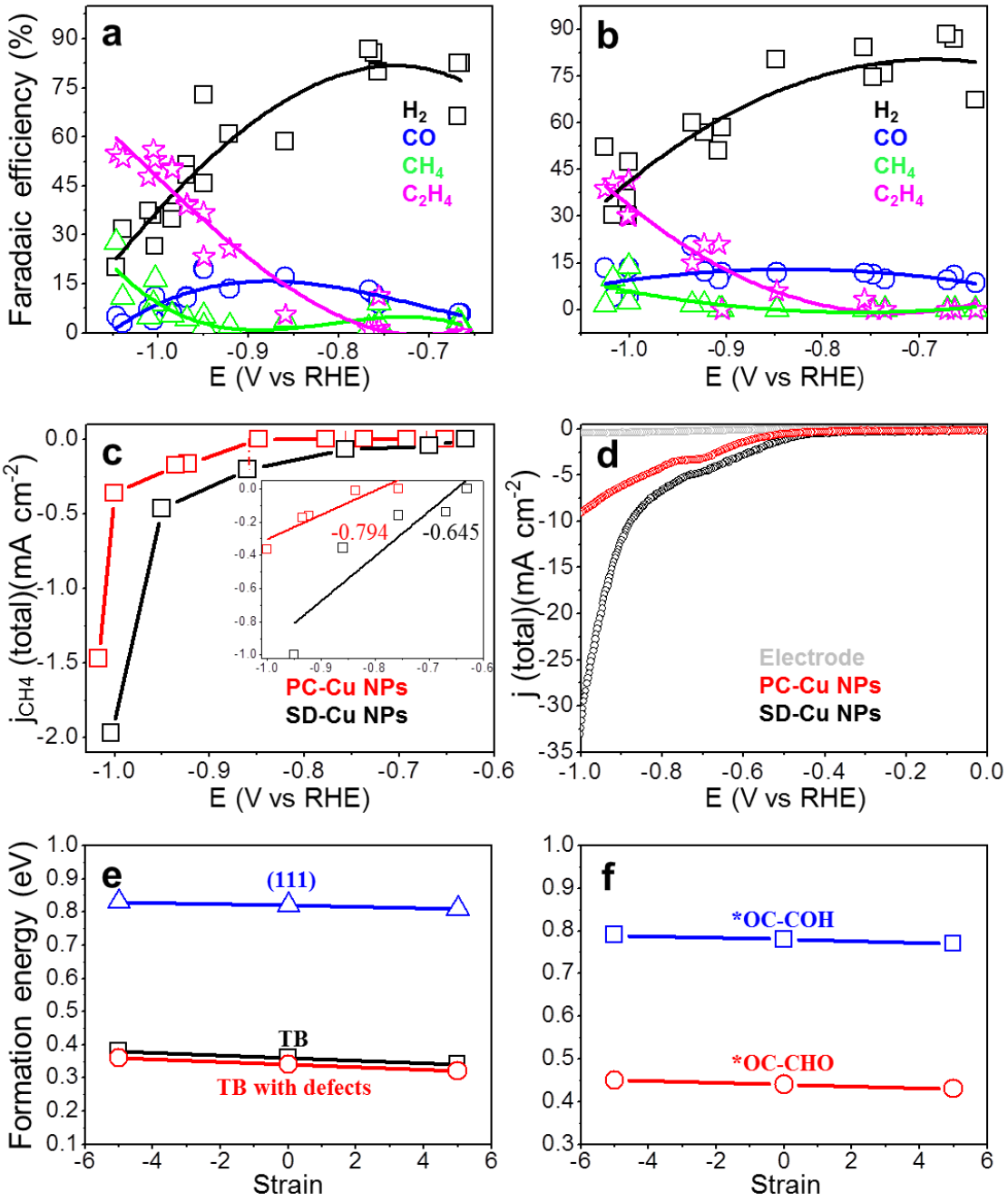

*Figure 2-8. (a) FE of SD-Cu NPs, (b) FE of PC-Cu NPs, (c) ECSA normalized CH_4 partial current density, (d) ECSA normalized total current density, (e) The formation energy of *CHO on TB and TB with surface defects, and formation energy of *COH on Cu(111) as a function of surface strain,*

*(f) The formation energy of *OC-COH and *OC-CHO intermediates on TB as a function of surface strain.*

The polycrystalline structure of commercial Cu NPs and the grain boundaries may contribute to the observed difference in C_2H_4 production[46]. Consistently, our SD-Cu NPs showed larger CH_4 partial current densities at all applied potentials than PC-Cu NPs (figure 2-8c). Notably, the onset potential of CH_4 on SD-Cu NPs was only around -0.645 V, which is 0.149 V lower than that of the PC-Cu NPs (-0.794 V) in figure 2-8c. The onset potential for CH_4 was measured by using an interpolation method with linear fitting to initial CH_4 partial current density. The ECSA normalized current densities of SD-Cu NPs also exhibited higher current densities than PC-Cu NPs at all measured potentials (figure 2-8d). In addition, the partial current density plot behavior[47,48] for both C_2H_4 and CH_4 shows that SD-Cu NPs consistently exhibit a significantly higher intrinsic activity than PC-Cu NPs in figure 2-9.

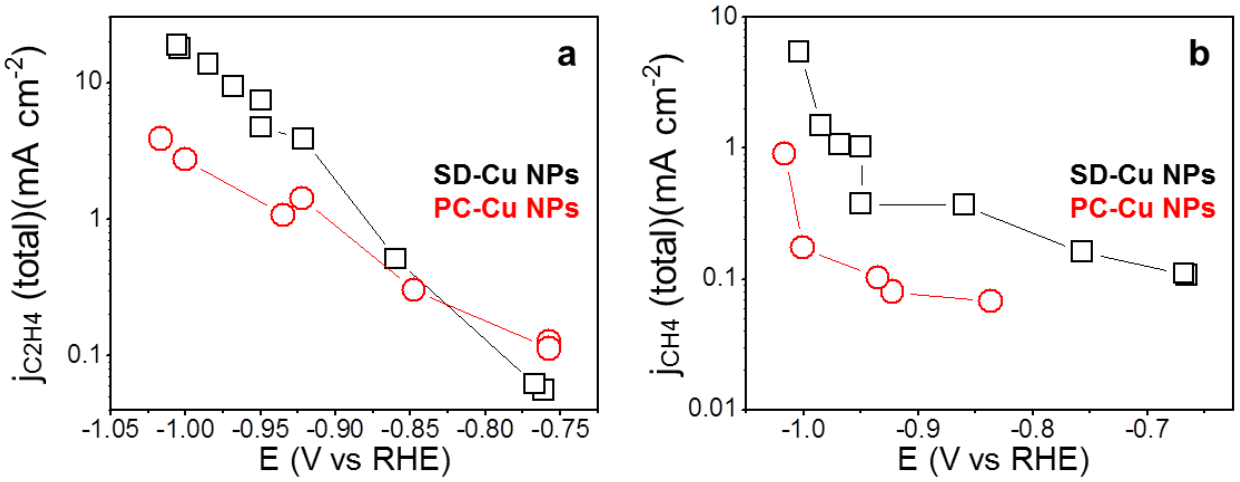

Figure 2-9. Partial current densities to CH_4 and C_2H_4, (a) C_2H_4 partial current densities, (b) CH_4 partial current densities.

To understand the origin for the superior performance of SD-Cu NPs towards CO_2RR to CH_4, we carried out density functional theory calculations using the level of Perdew-Burke-Ernzerhof functional (with Becke-Jonson damping D3 vdW correction) to investigate the critical reactive intermediates in the reaction pathway. As found in our previous work, in the reaction pathway for CH_4 formation via either *CHO formation or *COH formation, depending on the facet, determines the onset potential[46,49]. For the TB, we considered both possibilities in DFT calculations and found that the formation energy of *CHO is 0.36 eV, which is considerably less than the formation energy of 0.89 eV for *COH. Thus, the DFT calculations predict that CH_4 formation on TBs is through *CHO. Furthermore, from nudged elastic band calculations, we calculated an energy barrier of 0.67 eV for the formation of CH_4, which is 0.13 eV lower than the 0.80 eV energy barrier for the rate determining step of the CH_4 formation on Cu(111), obtained previously from the same level of DFT (figure 2-10)[49].

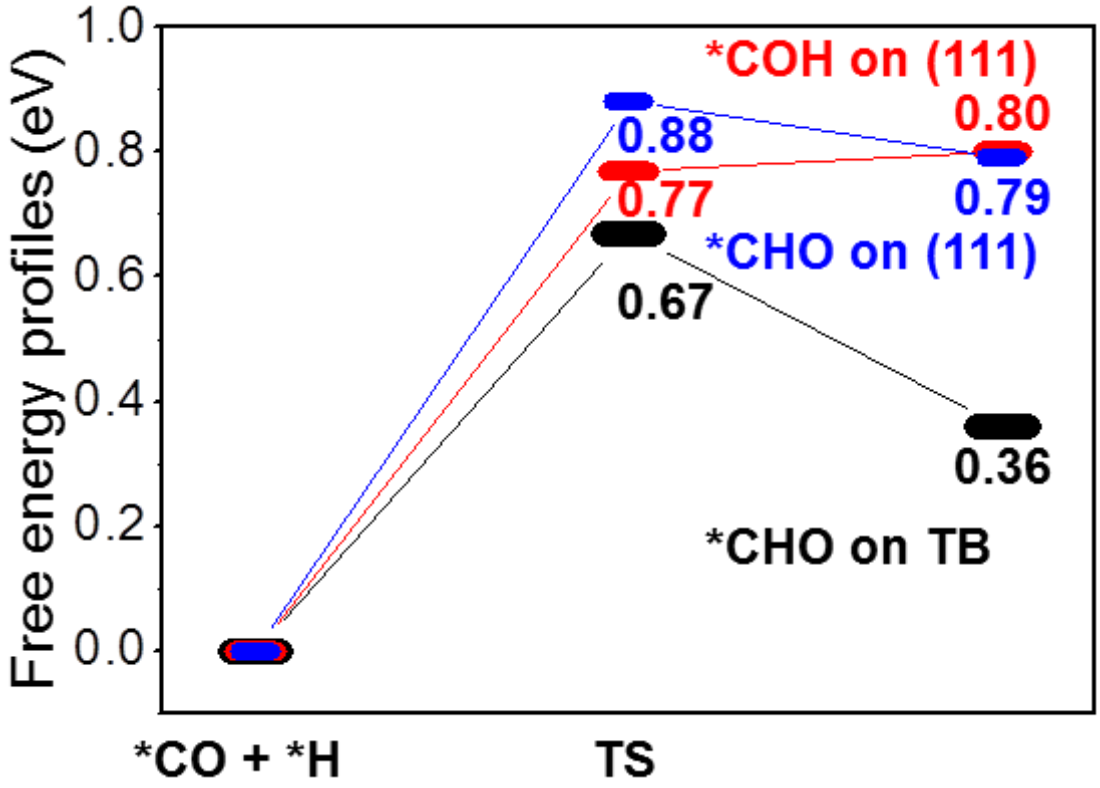

*Figure 2-10. TS and formation energy of *COH on (111), *CHO on (111) and *CHO on TB. Data for *COH on (111).*

This indicates an increase in the reaction rate. It is known that the (111) surface is a stable surface under the operando condition as confirmed by Kim et al.[50] and that the (111) surface selectively reduces CO_2 to CH_4[51]. Accordingly, it is reasonable to consider that the (111) surface represents poly-crystalline Cu despite the presence of other minor sites (such as steps sites)[52]. Figure 2-8e and 2-10 show that compared with (111), the TB decreases both the reaction energy and the energy barrier of CH_4 formation, which explains the lower onset potential of CH_4 formation we observed.

Another feature of figure 2-8a is the competition between CH_4 and C_2H_4 as the applied potential goes more negative (<-0.75 V). To investigate the formation of C_2H_4 on TB, we carried out DFT calculations for the two possible steps that might become rate limiting: the formation of *OC-COH and the formation of *OC-CHO[46]. DFT calculations show that on the TB the formation energy of *OC-CHO is 0.44 eV while the formation energy of *OC-COH is 0.78 eV (figure 2-8f). Thus, C_2H_4 formation through *OC-CHO is dramatically favored on the TB. This intermediate is formed from the coupling of *CO and *CHO. Since *CHO also is an intermediate in CH_4 formation, we consider *CHO as the common intermediate for both CH_4 and C_2H_4 formation in figure 2-11, which explains the experimental observations as follows: CH_4 likely dominates at low CO coverage, but C_2H_4 may dominate at high coverage.

At high overpotentials, however, the TB alone cannot explain the superior C_2H_4 production of SD-Cu NPs over most previously reported Cu based catalysts. It is well-established that as multiple-twinned NPs grow larger, the internal strain on the surface increases[42,43]. Larger strain destabilizes multiple-twinned NPs, causing several stress release mechanisms on the surface of

NPs to ameliorate the increasing internal stress. Interestingly, the stress-release mechanism induces grooving edges on multiple-twinned NPs and additional structural defects on such surfaces as steps and stacking faults[42,43].

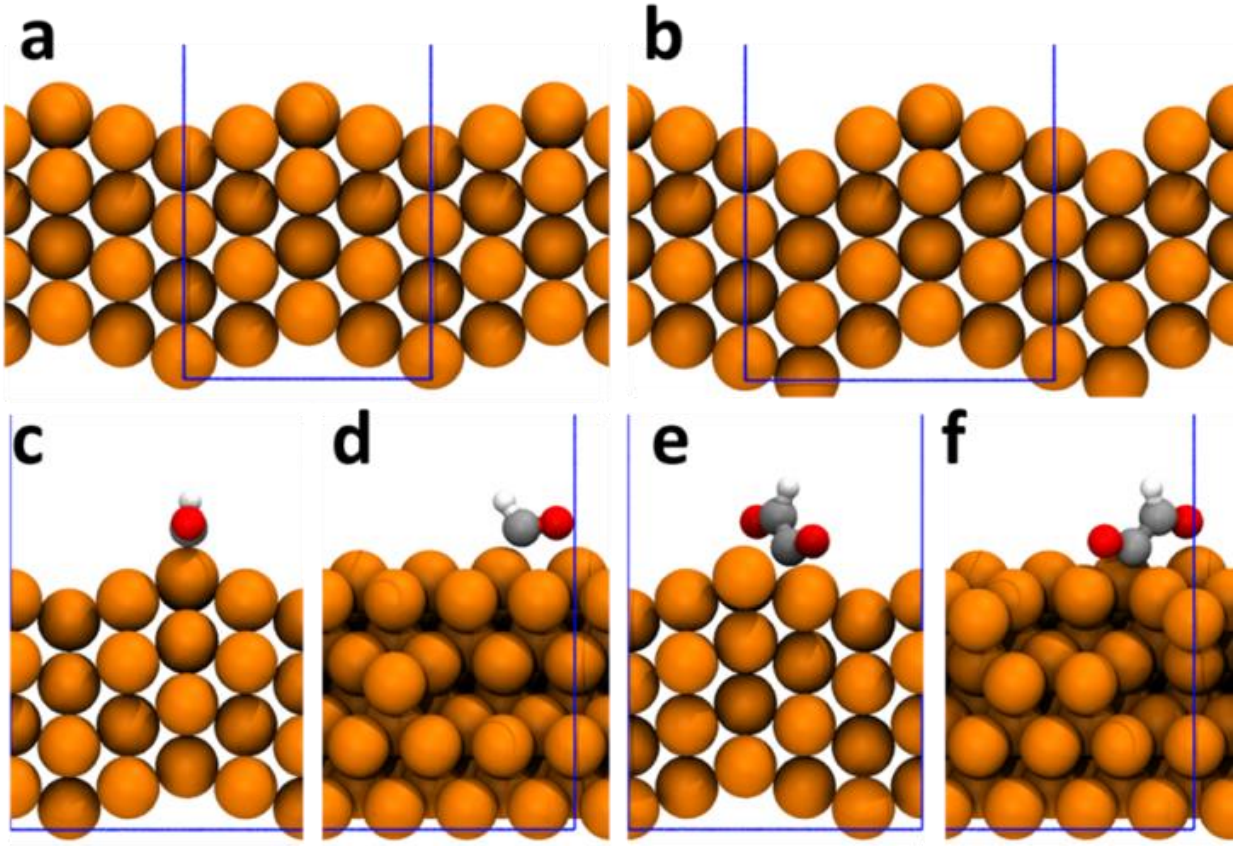

*Figure 2-11. The atomic simulation model of (a) TB, (b) TB with stacking defect, (c) The optimized geometry of *CHO on TB from side view, (d) Rotated by 90° along z-axis, (e) The optimized geometry of *OC-CHO on TB from side view, (f) Rotated by 90° along z-axis.*

Furthermore, the formation of the bands of thin twin layers in one of the {111} sections on the decahedrons could cause HCP stacking faults enclosing the parallel thin twin layers[43,53]. It has been estimated that Cu decahedrons NPs can maintain a balance between surface energy and strain

energy in size that is less than ~30,000 atoms (~ 13 nm)[54]. Indeed our 30 nm SD-Cu NPs, bands of TBs (figure 2-8), clearly exhibit rich stacking faults (figure 2-12a, b, c) and small surface strain (figure 2-12f) as a result of releasing of internal stress.

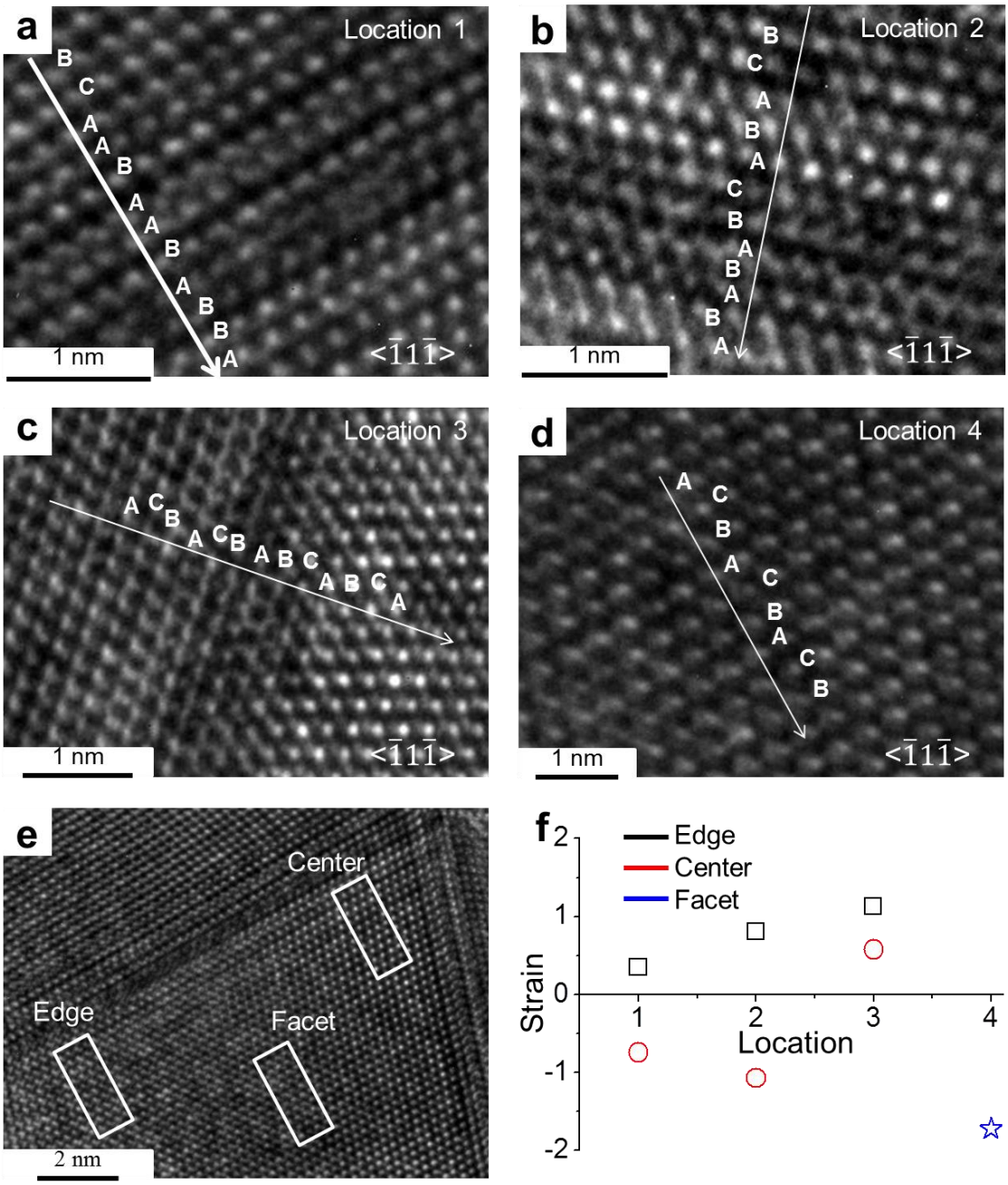

Figure 2-12. Four types of TB areas, (a) Parallel TB, (b) TB with HCP stacking faults, (c) Single TB, (d) Center of (-11-1) facet, (e) Strain analysis points: top, edge, and center, (f) Strain measured at each above stacking.

Three typical types of TBs in SD-Cu NPs are present in figure 2-12a, b, c: parallel twin boundary, a twin boundary with HCP stacking faults, and a single twin boundary. I determined the stacking sequence by assigning one layer as A and the subsequent layers as B, C and so forth[55]. I analyzed the surface strain of SD-Cu NPs for these three types of TBs as well as at the (111) facet (figure 2-12e, f). All measured strains near the edge of the SD-Cu NPs show tension strains, while strains near the center of the SD-Cu show compression strains except for the case of a single TB (location 3), which is consistent with measured strains in the 2D projection TEM reported for gold decahedron NPs[56,57]. The single TB shows the highest tension strain (+1.128%) and the strains tend to decrease with bands of thin twin defects and with stacking faults, consistent with the stress release mechanism. Theoretical studies had predicted that only 1% surface strain could shift the d-band center of Pt by about 0.1 eV, which has a pronounced effect on the binding strength of reactive adsorbates[57,58]. Similarly, the relatively high d-band center to the Fermi level in Cu NPs may lead to higher binding due to a less degree of occupancy of the anti-bonding states[59].

Both structure defects on catalyst surfaces (point, line, and planar defects) and applied tension strains are known to shift upward the d-band center of surface atoms, which results in increased binding energy between the catalysts and the reacting molecules[59]. By using He I-ion ultraviolet source, valence-level electrons of Cu NPs were scanned from 0 to 16 eV, and the valence band spectra from each Cu NPs catalysts were measured by ultraviolet photoelectron spectroscopy in figure 2-1 and 2-12a.

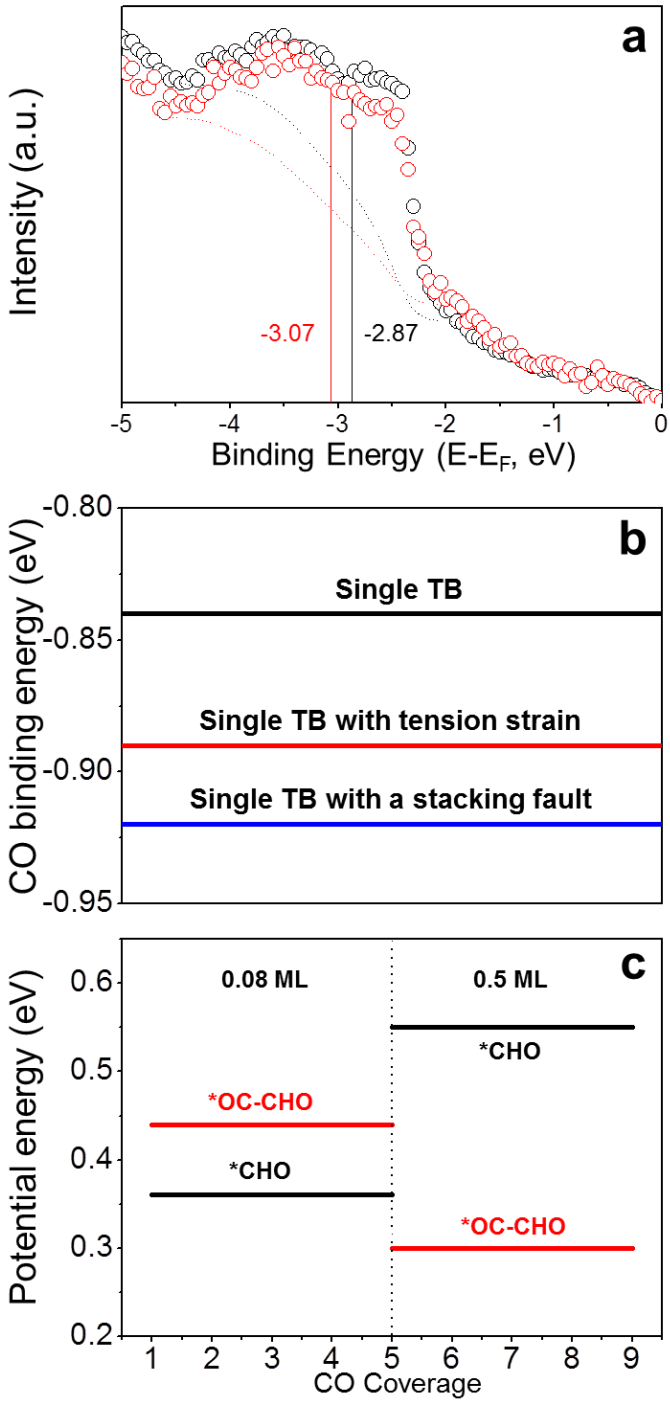

Figure 2-13. (a) D-band center of SD-Cu NPs (black) and PC-Cu NPs (red), (b) DFT energetics for various defect structures. Most stable is TB with a stacking fault, (c) DFT relative energies for

surface species. Low coverage favors CHO, the intermediate for CH_4 production, and high coverage favors OC-CHO, the intermediate for C_2H_4.

I observed that SD-Cu NPs exhibit 0.2 eV higher d-band center than that of the PC-Cu NPs. The combined surface tension strains and generation of structural defects from stress releasing in SD-Cu NPs may contribute to the upshift of the d-band center that enhanced the binding of the catalyst surface to surface adsorbates[59]. Thus, a possible driving force of the increased C_2H_4 production observed in SD-Cu NPs may be the higher CO binding energy and increased CO coverage on the surface[60].

DFT calculations were performed to elucidate these effects by constructing three types of TB atomic models; single TB, single TB with the tension strain, and single TB with the stacking fault. We found that a stacking defect with a single TB leads to a CO binding energy of -0.92 eV, which is about 0.08 eV stronger than a single TB on Cu (111) surface in figure 2-13b. We also found that enrichment of CO concentration on Cu surface promotes C-C coupling to produce C_2H_4 in figure 2-13c. For 0.5 monolayer (ML), $\Delta E^*_{OC\text{-}CHO}$ decreases to 0.30 eV, 0.14 eV lower than that in the dilute surface. However, ΔE^*_{CHO} increases to 0.54 eV in figure 2-13c. Because $\Delta E^*_{OC\text{-}CHO}$ is now lower than ΔE^*_{CHO}, these QM calculations suggest that TB with higher CO concentration reduces CO_2 to C_2H_4 instead of CH_4, explaining the high FE of C_2H_4 and the suppression of CH_4 in SD-Cu NPs at higher potentials. In order to determine any structural changes induced by the CO_2RR, I analyzed the SD-Cu NPs after CO_2RR at -1 V for 1 h by using FFT, inverse FFT, and HRTEM in figure 2-14. Figure 2-14a illustrates no apparent change of SD-Cu NPs after 1 h of reaction. The bands of twin defects are still clear in figure 2-14b, which are marked clearly in the FFT, the inverse FFT images in figures 2-14c, d.

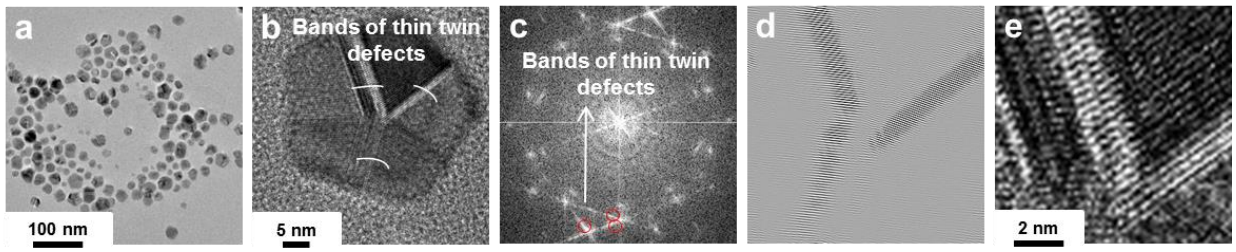

Figure 2-14. Analysis of SD-Cu NPs after electrochemical CO_2RR at -1 V for 1 h, (a) Low magnification TEM image of SD-Cu NPs after 1 h, (b) HRTEM image of SD-Cu NPs after 1 h, (c) FFT of SD-Cu NPs after 1 h, (d) Inverse FFT of SD-Cu NPs after 1 h, (e) Bands of twin defects after 1 h.

To test the long-term operating ability of SD-Cu NPs, we performed the stability test under applied -1 V (RHE) for 12 h. I found that the FE_{C2H4} remained over 50% and the current remained 17 mA cm^{-2} up to 12 h, as shown in figure 2-15, confirming the high stability of the SD-Cu NPs with high FE_{C2H4} (over 50%).

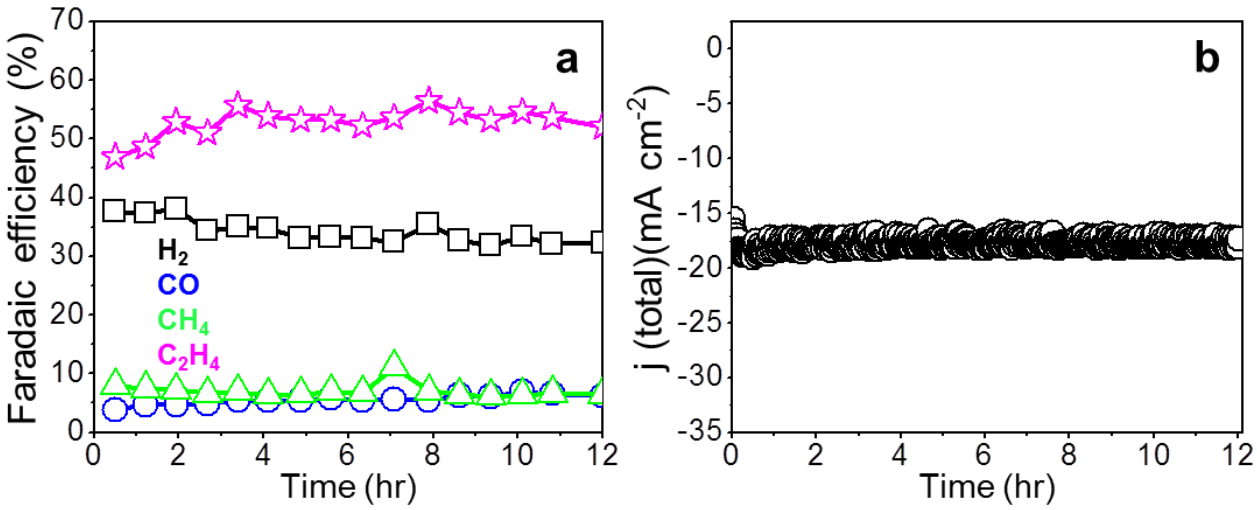

Figure 2-15. Stability test of SD-Cu NPs under -1 V (RHE) for 12 h, (a) FE of SD-Cu NPs, (b) Geometric area normalized current density of SD-Cu NPs.

I also carefully analyzed structures of SD-Cu NPs after the 12 h stability test (figure 2-16). Compared to the 1 h reaction, I observed that SD-Cu NPs experienced some degree of aggregation, but individual SD-Cu NPs within the aggregate still maintained their morphology after 12 h. More importantly, TBs and bands of twin defect in SD-Cu NPs were clearly visible up to 12 h, and they remained apparent even in the aggregated SD-Cu NPs in figures 2-16. Thus, I attribute the long-term sustained activity of SD-Cu NPs (over 50% FE_{C2H4}) to the stability of the created TBs and bands of twin defects even during NP aggregation.

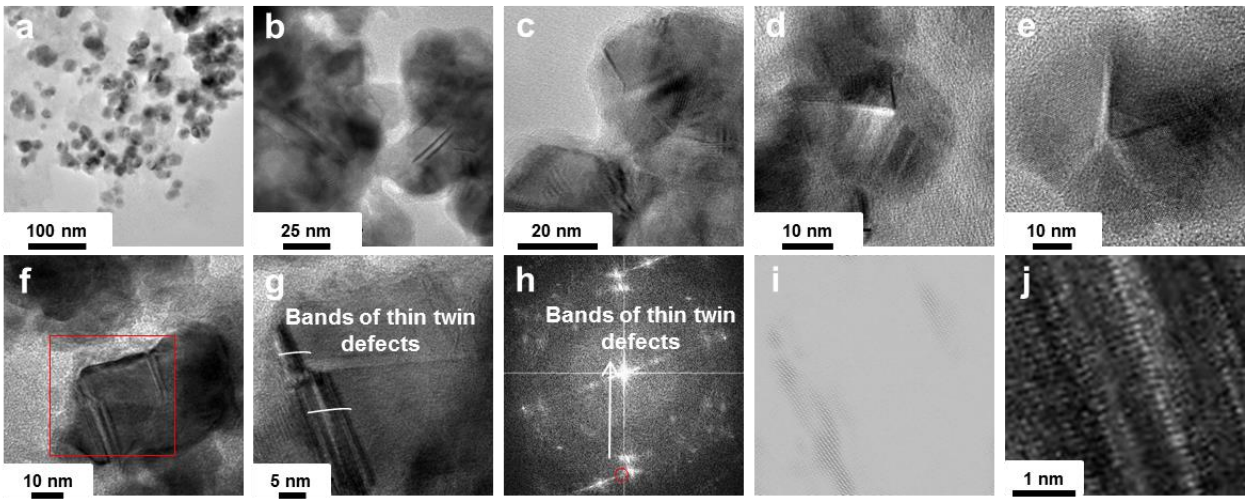

Figure 2-16. Analysis of SD-Cu NPs after electrochemical CO_2RR at -1 V for 12 h, (a) Low magnification TEM image of SD-Cu NPs after 12 h, (b, c, d, e, f) HRTEM image of SD-Cu NPs after 12 h, (g) HRTEM images of SD-Cu NPs after 12 h (extending of a red box in figure 2-16f), (h) FFT of SD-Cu NPs after 12 h, (i) Inverse FFT of SD-Cu NPs after 12 h, (j) Bands of twin defects after 12 h.

2.4 Conclusion

To summarize, I synthesized multiple-twined SD-Cu NPs with surface defects and tension strains. These SD-Cu NPs show an onset potential of -0.645 V, which is -0.149 V lower than for PC-Cu NPs. I found TBs on Cu NPs decrease the onset potential for CO_2RR to CH_4. Interestingly, I found that TBs combined with additional surface tension strain and stacking faults play essential roles in the increased FE for C_2H_4 formation and the suppression of CH_4 production. SD-Cu NPs show a dramatic improvement in C_2H_4 production in the potential range from -0.92 V to -0.98 V with a concomitant decrease in CH_4 production by -0.98 V. DFT calculations show that the existence of TB significantly decreases the formation energy of *CHO, which facilities the formation of CH_4 at low overpotential. At high overpotential *CHO becomes a common intermediate for forming both CH_4 and C_2H_4, which explains the competition between CH_4 and C_2H_4.

2.5 Chapter 2. Reference

[1] DiMeglio, J. L., & Rosenthal, J. Selective conversion of CO_2 to CO with high efficiency using an inexpensive bismuth-based electrocatalyst. *Journal of the American Chemical Society* **135**, 8798-8801 (2013).

[2] Li, C. W., & Kanan, M. W. CO_2 reduction at low overpotential on Cu electrodes resulting from the reduction of thick Cu_2O films. *Journal of the American Chemical Society* **134**, 7231-7234 (2012).

[3] Chen, Y., Li, C. W., & Kanan, M. W. Aqueous CO_2 reduction at very low overpotential on oxide-derived Au nanoparticles. *Journal of the American Chemical Society* **134**, 19969-19972 (2012).

[4] Chen, Y., & Kanan, M. W. Tin oxide dependence of the CO_2 reduction efficiency on tin electrodes and enhanced activity for tin/tin oxide thin-film catalysts. *Journal of the American Chemical Society* **134**, 1986-1989 (2012).

[5] Hori, Y., Kikuchi, K., & Suzuki, S. Production of CO and CH_4 in electrochemical reduction of CO_2 at metal electrodes in aqueous hydrogen carbonate solution. *Chemistry Letters* **14**, 1695-1698 (1985).

[6] Hori, Y., Wakebe, H., Tsukamoto, T., & Koga, O. Electrocatalytic process of CO selectivity in electrochemical reduction of CO_2 at metal electrodes in aqueous media. *Electrochimica Acta* **39**, 1833-1839 (1994).

[7] Hori, Y. I. Electrochemical CO_2 reduction on metal electrodes. In Modern aspects of electrochemistry (pp. 89-189). Springer, New York, NY (2008).

[8] Lee, H. E., Yang, K. D., Yoon, S. M., Ahn, H. Y., Lee, Y. Y., Chang, H., ... & Nam, K. T. Concave rhombic dodecahedral Au nanocatalyst with multiple high-index facets for CO_2 reduction. *ACS nano* **9**, 8384-8393 (2015).

[9] Kuhl, K. P., Cave, E. R., Abram, D. N., & Jaramillo, T. F. New insights into the electrochemical reduction of carbon dioxide on metallic copper surfaces. Energy & Environmental *Science* **5**, 7050-7059 (2012).

[10] Manthiram, K., Beberwyck, B. J., & Alivisatos, A. P. Enhanced electrochemical methanation of carbon dioxide with a dispersible nanoscale copper catalyst. *Journal of the American Chemical Society* **136**, 13319-13325 (2014).

[11] Hori, Y., Takahashi, R., Yoshinami, Y., & Murata, A. Electrochemical reduction of CO at a copper electrode. *The Journal of Physical Chemistry B* **101**, 7075-7081 (1997).

[12] Feng, X., Jiang, K., Fan, S., & Kanan, M. W. A direct grain-boundary-activity correlation for CO electroreduction on Cu nanoparticles. *ACS Central Science* **2**, 169-174 (2016).

[13] Huang, J., Hörmann, N., Oveisi, E., Loiudice, A., De Gregorio, G. L., Andreussi, O., ... & Buonsanti, R. Potential-induced nanoclustering of metallic catalysts during electrochemical CO_2 reduction. *Nature Communications* **9**, 1-9 (2018).

[14] Khan, M. U., Wang, L., Liu, Z., Gao, Z., Wang, S., Li, H., ... & Zeng, J. Pt_3Co octapods as superior catalysts of CO_2 hydrogenation. *Angewandte Chemie International Edition* **55**, 9548-9552 (2016).

[15] Asadi, M., Kim, K., Liu, C., Addepalli, A. V., Abbasi, P., Yasaei, P., ... & Zapol, P. Nanostructured transition metal dichalcogenide electrocatalysts for CO_2 reduction in ionic liquid. *Science* **353**, 467-470 (2016).

[16] Li, C. W., Ciston, J., & Kanan, M. W. Electroreduction of carbon monoxide to liquid fuel on oxide-derived nanocrystalline copper. *Nature* **508**, 504-507 (2014).

[17] Cheng, T., Xiao, H., & Goddard, W. A. Nature of the active sites for CO reduction on copper nanoparticles; suggestions for optimizing performance. *Journal of the American Chemical Society* **139**, 11642-11645 (2017).

[18] Cheng, T., Huang, Y., Xiao, H., & Goddard III, W. A. Predicted structures of the active sites responsible for the improved reduction of carbon dioxide by gold nanoparticles. *The Journal of Physical Chemistry Letters* **8**, 3317-3320 (2017).

[19] Ruan, L., Ramezani-Dakhel, H., Lee, C., Li, Y., Duan, X., Heinz, H., & Huang, Y. A rational biomimetic approach to structure defect generation in colloidal nanocrystals. *ACS nano* **8**, 6934-6944 (2014).

[20] Wu, J., Qi, L., You, H., Gross, A., Li, J., & Yang, H. Icosahedral platinum alloy nanocrystals with enhanced electrocatalytic activities. *Journal of the American Chemical Society* **134**, 11880-11883 (2012).

[21] Johnson, C. L., Snoeck, E., Ezcurdia, M., Rodríguez-González, B., Pastoriza-Santos, I., Liz-Marzán, L. M., & Hÿtch, M. J. Effects of elastic anisotropy on strain distributions in decahedral gold nanoparticles. *Nature materials* **7**, 120-124 (2008).

[22] Ruan, L., Chiu, C. Y., Li, Y., & Huang, Y. Synthesis of platinum single-twinned right bipyramid and {111}-bipyramid through targeted control over both nucleation and growth using specific peptides. *Nano letters* **11**, 3040-3046 (2011).

[23] Huang, H., Jia, H., Liu, Z., Gao, P., Zhao, J., Luo, Z., ... & Zeng, J. Understanding of strain effects in the electrochemical reduction of CO_2: using Pd nanostructures as an ideal platform. *Angewandte Chemie International Edition* **129**, 3648-3652 (2017).

[24] Ruan, L., Zhu, E., Chen, Y., Lin, Z., Huang, X., Duan, X., & Huang, Y. Biomimetic synthesis of an ultrathin platinum nanowire network with a high twin density for enhanced electrocatalytic activity and durability. *Angewandte Chemie International Edition* **125**, 12809-12813 (2013).

[25] Wang, C., Yin, H., Chan, R., Peng, S., Dai, S., & Sun, S. One-pot synthesis of oleylamine coated AuAg alloy NPs and their catalysis for CO oxidation. *Chemistry of Materials* **21**, 433-435 (2009).

[26] Xia, Y., Xiong, Y., Lim, B., & Skrabalak, S. E. Shape-controlled synthesis of metal nanocrystals: simple chemistry meets complex physics? *Angewandte Chemie International Edition* **48**, 60-103 (2009).

[27] B. Merle, *Mechanical Properties of Thin Films Studied by Bulge Testing* (Ph.D. thesis, Erlangen FAU Univ.) (2013).

[28] Huang, H., & Spaepen, F. Tensile testing of free-standing Cu, Ag and Al thin films and Ag/Cu multilayers. *Acta Materialia* **48**, 3261-3269 (2000).

[29] Ma, Y., Zeng, J., Li, W., McKiernan, M., Xie, Z., & Xia, Y. Seed-mediated synthesis of truncated gold decahedrons with a AuCl/oleylamine complex as precursor. *Acta Materialia* **22**, 1930-1934 (2010).

[30] Lloyd, D. R., Quinn, C. M., & Richardson, N. V. Angular-resolved HeI photoelectron spectra for the (001) face of a copper single crystal. Journal of Physics C: *Solid State Physics* **8**, L371 (1975).

[31] Baturina, O. A., Lu, Q., Padilla, M. A., Xin, L., Li, W., Serov, A., ... & Brintlinger, T. CO_2 electroreduction to hydrocarbons on carbon-supported Cu nanoparticles. *ACS Catalysis* **4**, 3682-3695 (2014).

[32] Zhu, W., Michalsky, R., Metin, O., Lv, H., Guo, S., Wright, C. J., ... & Sun, S. Monodisperse Au nanoparticles for selective electrocatalytic reduction of CO_2 to CO. *Journal of the American Chemical Society* **135**, 16833-16836 (2013).

[33] Kern, G., Kresse, G., & Hafner, J. J. P. R. B. Ab initio calculation of the lattice dynamics and phase diagram of boron nitride. *Physical Review B* **59**, 8551 (1999).

[34] Kresse, G., & Furthmüller, J. Efficiency of ab-initio total energy calculations for metals and semiconductors using a plane-wave basis set. *Computational materials science* **6**, 15-50 (1996).

[35] Kresse, G., & Furthmüller, J. Efficient iterative schemes for ab initio total-energy calculations using a plane-wave basis set. *Physical review B* **54**, 11169 (1996).

[36] Perdew, J. P., Burke, K., & Ernzerhof, M. Generalized gradient approximation made simple *Physical review letters* **77**, 3865 (1996).

[37] Kresse, G., & Joubert, D. From ultrasoft pseudopotentials to the projector augmented-wave method. *Physical review B* **59**, 1758 (1999).

[38] Grimme, S., Antony, J., Ehrlich, S., & Krieg, H. A consistent and accurate ab initio parametrization of density functional dispersion correction (DFT-D) for the 94 elements H-Pu. *The Journal of chemical physics* **132**, 154104 (2010).

[39] Sundararaman, R., & Goddard III, W. A. The charge-asymmetric nonlocally determined local-electric (CANDLE) solvation model. *The Journal of chemical physics* **142**, 064107 (2015).

[40] Garrity, K. F., Bennett, J. W., Rabe, K. M., & Vanderbilt, D. Pseudopotentials for high-throughput DFT calculations. *Computational Materials Science* **81,** 446-452 (2014).

[41] De Jong, A. F., Coene, W., & Van Dyck, D. Image processing of HRTEM images with non-periodic features. *Ultramicroscopy* **27**, 53-65 (1989).

[42] Yacamán, M. J., Ascencio, J. A., Liu, H. B., & Gardea-Torresdey, J. Structure shape and stability of nanometric sized particles. *Journal of Vacuum Science & Technology B: Microelectronics and Nanometer Structures Processing, Measurement, and Phenomena* **19**, 1091-1103 (2001).

[43] Gryaznov, V. G., Kaprelov, A. M., Romanov, A. E., & Polonskii, I. A. Channels of relaxation of elastic stresses in pentagonal nanoparticles. *physica status solidi (b)* **167**, 441-450 (1991).

[44] Sun, S., & Wang, Z. L. Shapes, multiple twins and surface structures of monodisperse FePt magnetic nanocrystals. *Surface Science* **505**, 325-335 (2002).

[45] Dinh, C. T., Burdyny, T., Kibria, M. G., Seifitokaldani, A., Gabardo, C. M., De Arquer, F. P. G., ... & Zou, C. CO_2 electroreduction to ethylene via hydroxide-mediated copper catalysis at an abrupt interface. *Science* **360**, 783-787 (2018).

[46] Cheng, T., Xiao, H., & Goddard, W. A. Full atomistic reaction mechanism with kinetics for CO reduction on Cu (100) from ab initio molecular dynamics free-energy calculations at 298 K. *Proceedings of the National Academy of Sciences* **114**, 1795-1800 (2017).

[47] Clark, E. L., Resasco, J., Landers, A., Lin, J., Chung, L. T., Walton, A., ... & Bell, A. T. Standards and protocols for data acquisition and reporting for studies of the electrochemical reduction of carbon dioxide. *ACS Catalysis* **8**, 6560-6570 (2018).

[48] Singh, M. R., Clark, E. L., & Bell, A. T. Effects of electrolyte, catalyst, and membrane composition and operating conditions on the performance of solar-driven electrochemical reduction of carbon dioxide. *Physical Chemistry Chemical Physics* **17**, 18924-18936 (2015).

[49] Xiao, H., Cheng, T., Goddard III, W. A., & Sundararaman, R. Mechanistic explanation of the pH dependence and onset potentials for hydrocarbon products from electrochemical reduction of CO on Cu (111). *Journal of the American Chemical Society* **138**, 483-486 (2016).

[50] Kim, Y. G., Javier, A., Baricuatro, J. H., Torelli, D., Cummins, K. D., Tsang, C. F., ... & Soriaga, M. P. Reprint of Surface reconstruction of pure-Cu single-crystal electrodes under CO-reduction potentials in alkaline solutions: A study by seriatim ECSTM-DEMS. *Journal of Electroanalytical Chemistry* **793**, 113-118 (2017).

[51] Schouten, K. J. P., Qin, Z., Pérez Gallent, E., & Koper, M. T. Two pathways for the formation of ethylene in CO reduction on single-crystal copper electrodes. *Journal of the American Chemical Society* **134**, 9864-9867 (2012).

[52] Liu, X., Xiao, J., Peng, H., Hong, X., Chan, K., & Nørskov, J. K. Understanding trends in electrochemical carbon dioxide reduction rates. *Nature communications* **8**, 1-7 (2017).

[53] Lucadamo, G., & Medlin, D. L. Geometric origin of hexagonal close packing at a grain boundary in gold. *Science* **300**, 1272-1275 (2003).

[54] Baletto, F., & Ferrando, R. Structural properties of nanoclusters: Energetic, thermodynamic, and kinetic effects. *Reviews of modern physics* **77**, 371 (2005).

[55] H. S. Nalwa; *Encyclopedia of Nanoscience and Nanotechnology* **3**, 431, (2004).

[56] Walsh, M. J., Yoshida, K., Kuwabara, A., Pay, M. L., Gai, P. L., & Boyes, E. D. On the structural origin of the catalytic properties of inherently strained ultrasmall decahedral gold nanoparticles. *Nano letters* **12**, 2027-2031 (2012).

[57] Goris, B., De Beenhouwer, J., De Backer, A., Zanaga, D., Batenburg, K. J., Sánchez-Iglesias, A., ... & Van Tendeloo, G. Measuring lattice strain in three dimensions through electron microscopy. *Nano letters* **15**, 6996-7001 (2015).

[58] Strasser, P., Koh, S., Anniyev, T., Greeley, J., More, K., Yu, C., ... & Toney, M. F. Lattice-strain control of the activity in dealloyed core-shell fuel cell catalysts. *Nature chemistry* **2**, 454-460 (2010).

[59] Hammer, B., & Nørskov, J. K. Theoretical surface science and catalysis calculations and concepts. *Advances in catalysis* **45**, 71-129 (2000).

[60] Huang, Y., Handoko, A. D., Hirunsit, P., & Yeo, B. S. Electrochemical reduction of CO_2 using copper single-crystal surfaces: effects of CO* coverage on the selective formation of ethylene. *ACS Catalysis* **7**, 1749-1756 (2017).

3 Chapter 3. Cu Nanowires with Rich Surface Steps for CO_2RR

3.1 Introduction

Developing highly-efficient electrocatalysts for the carbon dioxide reduction reaction to value-added fuels and chemicals could remediate problems caused by the ever-increasing CO_2 emission from human activities[1-3]. Several metal electrodes are known to reduce CO_2 in aqueous solutions[4]. Among the catalysts explored to date, Cu is the only well-known electrocatalytic material that converts CO_2 to hydrocarbons or alcohol products with significant activity and efficiency[5]. Also, due to Cu's natural abundance[6,7] and low cost, it has been intensively studied for CO_2RR for decades[6,8-19]. However, the low product selectivity towards valuable fuel products and the lack of long-term stability remain major challenges for Cu based catalysts[20]. Various approaches have been developed to address these challenges[8-19,21-33]. For example, Kanan and coworkers reported that the grain boundaries on Cu film[28-30] and surface defects[31] promote productions of hydrocarbons with one-carbon (C1 product)[19] (~ 45% CO ca. −0.5 V and ~33% HCO_2H ca. −0.65 V versus the reversible hydrogen electrode (RHE), referenced to for all potentials in this article unless otherwise specified). Moreover, residual surface copper oxides[21-26] have been suggested to enhance hydrocarbons having two carbons (C2)[21].

Among major gaseous products, ethylene (C_2H_4) is desirable since it is a basic building block to produce various plastics, solvents, and cosmetics. In 2020 alone, 158 million tons of C_2H_4 global market is estimated, and the annual demand for C_2H_4 is expected to grow ~4.5% through to 2027[34]. However, the low CO_2RR selectivity towards C_2H_4 production remains a challenge, with competition from the hydrogen evolution reaction and methane (CH_4) production[35]. It has been predicted and shown with single-crystal studies that the formation of specific surface step sites on Cu catalysts can lower the barrier for CO dimerization to promote C2 productions over C1

products[36,37]. Indeed, Cheng et al. performed a thorough DFT screening of active defect sites for electrochemical CORR to C2 products at GBs of Cu nanoparticles grown from chemical vapor deposition (CVD) on a carbon nanofiber[36]. They found that the most active surface sites for C2 productions on GBs of Cu NPs combine one strong CO binding site next to one weak CO binding site, dramatically reducing the energy of the *OCCHO transition state, making it active toward C2 production[36].

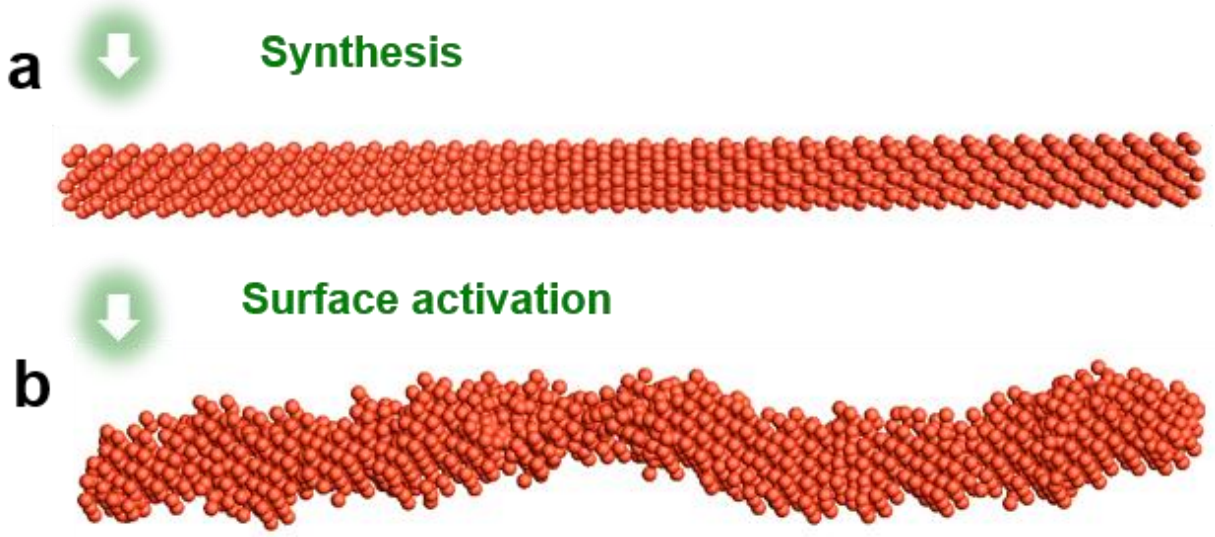

Figure 3-1. Schematic of preparing CuNWs with surface steps. (a) The as-synthesized CuNWs with {100} surface, (b) The CuNWs is activated in situ during the electrochemical CO_2RR to form surface steps.

In this study, I report the preparation of Cu nanowires with highly active stepped surfaces through the in situ electrochemical activation of pregrown CuNWs with {100} surfaces in figure 3-1. The electrochemical CO_2RR studies demonstrate a remarkably high C2 selectivity with a Faradaic efficiency towards C_2H_4 (FE_{C2H4} > 70%), as well as exceptionally high stability for ~200

hours. The high C_2H_4 selectivity is attributed to the unique surface structure of the CuNWs with abundant stepped sites. Our DFT studies showed that the Cu(511) plane [3(100)×(111)] stepped surface is thermodynamically favored at CO_2RR conditions over either Cu(100) or Cu(111) under the operating conditions, which explains the experimentally observed long-term stability. The calculations also revealed a higher barrier for the C1 path, along with a slower HER on Cu(511) compared with that of C2, which leads to the greatly enhanced selectivity towards C_2H_4.

3.2 Experimental Section

3.2.1 Preparation of CuNWs

Copper(II) chloride dihydrate ($CuCl_2 \cdot 2H_2O$, 99.999%), D-(+)-Glucose (> 99.5%), Hexadecylamine(HDA)(> 98 %), Ethanol (200 proof), 25 nm Cu NPs were all purchased from Sigma-Aldrich. Potassium hydroxide (KOH) and Hexane (99.9%) were purchased from Fisher Chemical. All chemicals were used without purification. Ultra-pure purification system (Milli-Q advantage A10) produced the DI water (18.2 MΩ/cm) used in making solutions. The 99.9% Cu foil from Metal Remnants, Inc. cut to 1 cm^2, and mechanically polished by 400G sandpaper from 3M, and electrochemically polished in 85% phosphoric acid under -1 V (RHE) for 5 min. The Cu foil was subsequently rinsed with DI water and used for CO_2RR. In a typical synthesis of CuNW catalysts, 22 mg $CuCl_2 \cdot 2H_2O$, 50 mg D-(+)-Glucose, 180 mg HDA were pre-dissolved in 10 mL DI water in 30 mL vial. The chemical solution was mixed in the sonication for 15 min and then transferred to an oil bath. The mixture was heated from room temperature to 100 °C for 8 h and cooled to room temperature. The synthesized CuNWs were washed five times with sonication in hexane/ethanol (1:1 volume) solvent for 20 min. The CuNWs were collected by centrifuge at 9500 rpm.

3.2.2 Materials characterization

Hexane dispersion of catalysts was dropped and dried onto carbon-coated copper TEM grids (Ted Pella, Redding, CA) under room temperature to prepare TEM samples. The FEI CM120 TEM at 120 kV was used for low-resolution TEM images. The FEI Titan TEM operating at 300 kV was used to take HRTEM. Dark field scanning TEM image was taken by JEM-ARM300F Grand ARM TEM at 300 kV. Scanning electron microscopy images were taken by Nova Nano 230, and SEI was taken by JEOL 2800 TEM with 200 kV. The size of CuNWs was measured by the largest diameter within the CuNWs. The size was determined by averaging more than 100 NWs. A Panalytical X'Pert Pro X-ray Powder Diffractometer with Cu-Kα radiation was used for PXRD patterns. ICP-AES (TJA RADIAL IRIS 1000) was conducted to determine the metal concentration in the catalysts used.

3.2.3 Electrode preparation and electrochemical CO_2RR measurements

4 mg of dried CuNWs was mixed with 1 mL ethanol and ultrasonication for 1 h. Subsequently, 10 μL of Nafion (5 wt%) was added and kept ultrasonication for an extra 10 min. 10 μL of the catalysts ink was dropped onto electrodes using a pipette and dried under ambient air. The 10 μL of the catalysts ink contained 0.04 mg Cu, which was measured by ICP-AES.

To activate CuNW catalysts and measure FE, a gas-tight electrolysis H-Cell (WizMac) separated with the Nafion ion exchange membrane (Sigma Aldrich) was used. The working electrode coated with catalysts was a L-type glassy-carbon electrode (diameter: 5 mm, area: 0.196 cm^2) from WizMac. The Pt coil from Pine Instruments was used as a counter electrode. The 4 M KCl Ag/AgCl electrode from Pine Instruments was used as a reference electrode. The impedance of each solution was tested on a Princeton VersaSTAT 4 electrochemistry workstation. After iR correction, all discussed potentials were converted to those against RHE.

The 0.1 M $KHCO_3$ electrolyte solution was used for every electrochemical CO_2RR. Before CO_2RR, I bubbled CO_2 (Air gas, 99.99%) for 30 min to reach saturation, and I kept purging CO_2 into the cathodic compartment at 15 sccm with stirring a stir bar (1200 rpm) during CO_2RR. The activation of CuNW catalysts was conducted with chronoamperometry (CA) in CO_2-saturated 0.1 M $KHCO_3$ solution at -1.05 V (RHE) over 1 h. We measured FE by using CA for 30 - 40 min at each applied potential except for the synthesized Cu nanowires (termed Syn-CuNWs) catalysts. The FEs of Syn-CuNW catalysts were measured in 10 min to prevent any activation of CuNW catalysts. For the long-term stability test, the CO_2 saturated 0.1 M $KHCO_3$ electrolyte was replaced every 12 h and applied pulse potentials (~ -0.97 V (RHE) for 600 s and 0.32 V (RHE) for 10 s) to remove possible surface poisoning from the produced formate[38,39]. The FEs was measured roughly every 2 - 3 h during the stability test except for during the night shift. The stability test was performed at room temperature and under atmospheric pressure.

Gas product analysis was done with a Shimadzu Tracera gas chromatography barrier ionization discharge 2010 Plus (Shimadzu) equipped with a Restek micropacked GC column. The standard curve of GC-BID was calibrated by five standard gases (Air gas). The carrier gas was helium (Air gas, 99.9999 %). A p-type Hastelloy 6 port sampling loop (1.5 mL) was directly routed to an outlet gas line of gas-tight H cell. 1.5 mL effluence gas was analyzed with the Shimadzu Tracera GC-BID 2010 Plus. The FE was calculated as below:[40]

$$FE_J = \frac{nFv_J G p_0}{RT_0 i_{total}} \times 100\% \quad (3\text{-}1)$$

where:

n = the number of electrons for a given product.

v_J (vol.%) = The volume concentration of gas products(CO, H_2, CH_4, and C_2H_4) in the effluence gas from the electrochemical cell (GC data)

G (ml/min at room temperature and ambient pressure) = Gas flow rate measured by a ProFlow 6000 electronic flow meter (Restek) at the exit of the electrochemical cell

i_{total} (mA) = steady-state cell current

p_0=1.01 x 105 Pa, T_0= 298.15 K, F = 96485 C•mol^{-1}, R = 8.314 J• mol^{-1}• K^{-1}

Quantitative NMR (Bruker AV-600) was conducted to analyze the liquid product. Specifically, 0.3 mL of D_2O was added to 0.65 mL of the reacted electrolyte, and 50 μL of dimethyl sulfoxide (0.512 μM/mL) was also mixed as an internal standard. The 1D 1H spectrum was measured with a pre-water saturation method.

3.2.4 Electrochemical measurements

Before I carried out OH_{ad} on CuNWs, the CuNWs on the L-type glassy carbon electrode was activated in H-cell with CO_2 saturated 0.1 M $KHCO_3$ by purging CO_2 gas. Then, the catalysts on the L-type glassy carbon electrode were transferred to a three-electrode cell.

For OH^- adsorption reaction, we conducted OH^- adsorption reaction CV in 0.1 M KOH at 100 mV/s scan rate with Hg/HgO reference electrode (CH Instrument). The OH^- adsorption reaction is described accurately by one electron process as follows[41].

$Cu^* + OH^- \leftrightarrow Cu^*(OH)_{ad} + e^-$ (3-2)

$Cu + OH^- \leftrightarrow Cu(OH)_{ad} + e^-$ (3-3)

To calculate the number of OH^- adsorptions on each Cu planes on the CV scan, the linear background was subtracted[42]. I integrated currents corresponding to the assigned Cu{100} facets, Cu{110} facets, Cu{111} facets, and A-(hkl) by each peak scan time as follows;

$$\frac{\int IdV}{v \times e} = \text{The numbers of OH adsorption on Cu facets} \quad (3\text{-}4)$$

Where:

I (C/s) = the current under OH^- absorption peak corresponding to each Cu facets

dV (V) = voltage of each Cu facets, v (V/s) = scan rate of OH^- adsorption CV scan, e = electric charge (1.602×10^{-19} C)

For the total current densities and ECSA measurement, the three-electrode cell was used. The working electrode was a glassy-carbon RDE (diameter: 5 mm, area: 0.196 cm^2) from Pine Instruments coated with catalysts. The graphite rod was used as the counter electrode. The double junction Ag/AgCl (the inner filling 4 M KCl and the outer filling 10% KNO_3) electrode from Pine Instruments was the reference electrode. The total current densities were measured from CV scans between 0 V to -1.1 V (RHE) at 50 mV/s with rotating RDE at 1200 rpm in CO_2 saturated 0.1 M $KHCO_3$. Subsequently, the ECSA of the CuNWs was measured by Pb UPD. The background current was measured in N_2-saturated 0.1 M $HClO_4$ between 0.26 V to -0.38 V (RHE) at 10 mV/s. In N_2-saturated 0.1 M $HClO_4$ + 0.001 M $Pb(ClO_4)_2$ solution at room temperature, the ECSA was carried out by subtracting the background current from the integrated Pb desorption charge on the CV between 0.26 V to -0.38 V (RHE) at 10 mV/s[43]. A conversion factor of 310 μC/cm^2 is based on a monolayer of Pb adatoms coverage over Cu and $2e^-$ Pb oxidation[43].

3.2.5 Computational details

The quantum mechanics calculations were carried out using the VASP software at the version of 5.4.4[44-46], with the Perdew, Burke, and Ernzerhof flavor[47] of DFT. The projector augmented wave method[48] was used to account for core-valence interactions. The kinetic energy cutoff for plane wave expansions was set to 500 eV, and reciprocal space was sampled by the Monkhorst-Pack scheme with a grid of 3×3×1 and 2×3×1 for Cu(100) and Cu(511), respectively. The vacuum layer is at least 20 Å above the surface. The convergence criteria are 1×10^{-5} eV energy differences for solving the electronic wave function. The Methfessel-Paxton smearing of

second order with a width of 0.1 eV was applied. All geometries (atomic coordinates) were converged to within 0.03 eV $Å^{-1}$ for maximal components of forces. A post-stage vdW DFT-D3 method with Becke-Jonson damping was applied[49]. The solvation was treated implicitly using the VASPsol[50] method.

We employed CI-NEB method[51] with five images to find potential energy surface along with the reaction coordinates, and the subsequent dimer method was applied near the saddle point to find the transition state until force converges < 0.01 eV/Å. All transition state has only one imaginary frequency.

All Gibbs free energy includes vibrational contributions of zero-point energy, enthalpy, and entropy. To compare all surfaces, we normalized the Gibbs free energy to its surface area in table 3-1. The Gibbs free energies were calculated at 298 K and 1 atm as outlined in:

$$\mathrm{G} = \mathrm{H} - \mathrm{T}\Delta\mathrm{S} = \mathrm{E_{DFT}} + \mathrm{E_{ZPE}} + \mathrm{E_{solv}} + \int_0^{298} \mathrm{C_v}\,\mathrm{dT} - \mathrm{T}\Delta\mathrm{S} \quad (3\text{-}5)$$

Where E_{DFT} is the DFT-optimized total energy, E_{ZPE} is the zero-point vibrational energy, E_{solv} is the solvation energy. $\int_0^{298} \mathrm{C_v}\,\mathrm{dT}$ is the heat capacity, T is the temperature, and ΔS is the entropy.

For the surface phase diagram, Gibbs free energy change is calculated at 298 K, pH 7 as outlined:

$$\Delta G_{surf} = G_{surf-sol} - G_{bulk-sol} - NG_{H2O-sol} + n\left(\frac{1}{2}G^{\circ}_{H_2} + k_B T \ln a_{H^+} - eU\right) \quad (3\text{-}6)$$

Where G is the Gibbs free energy, kB is the Boltzmann constant, T is the temperature, a_{H+} is the proton activity, U is an applied potential.

Table 3-1. Free energy, Frequency, Zero-point energy, Enthalpy (Cv), Entropy of all states in DFT calculations.

			Energy [eV]	Frequency [cm^{-1}]	ZPE [eV]	Cv [eV]	TS [eV]
Cu(100)	C1	IS	-263.645	3719.04	1.606498	0.170446	0.232887
		TS	-262.971	3643.092	1.473867	0.179751	0.250323
		FS	-263.98	3716.55	1.731384	0.179365	0.249453
	C2	IS	-263.878	2697.653	0.630043	0.167448	0.253563
		TS	-263.45	2757.024	0.613232	0.13664	0.189569
		FS	-264.291	2751.579	0.674542	0.148478	0.22949
Cu(511)	C1	IS	-207.912	3711.546	1.435686	0.159278	0.221053
		TS	-207.204	3762.022	1.348848	0.189453	0.279913
		FS	-208.391	3759.418	1.583465	0.156297	0.230906
	C2	IS	-208.175	2704.296	0.641028	0.162215	0.24363
		TS	-207.709	2709.244	0.617154	0.140325	0.20639
		FS	-208.316	2813.459	0.680842	0.122072	0.179666

3.3 Result and discussion

3.3.1 Synthesis of CuNWs(Syn-CuNWs) and activation of CuNWs(A-CuNWs)

In a typical synthesis of CuNWs catalyst, 22 mg $CuCl_2 \cdot 2H_2O$, 50 mg of glucose, and 150 mg of hexadecylamine were pre-dissolved in 10 mL deionized water (18.2 MΩ/cm)[52]. The mixture was sonicated for 15 min, heated from room temperature to 100 °C, and kept there for 8 h in an oil bath. The Syn-CuNWs were collected by centrifuge and washed five times with hexane/ethanol mixture. The structure of Syn-CuNWs was characterized by transmission electron microscopy, scanning electron imaging (SEI), and powder X-ray diffraction. The PXRD peaks of the prepared products match well with those of the Cu JCPDS (#00-004-0836) in figure 3-2a. The average size of these Syn-CuNWs was determined to be 25 nm ± 7.7 nm in diameter in figure 3-2b.

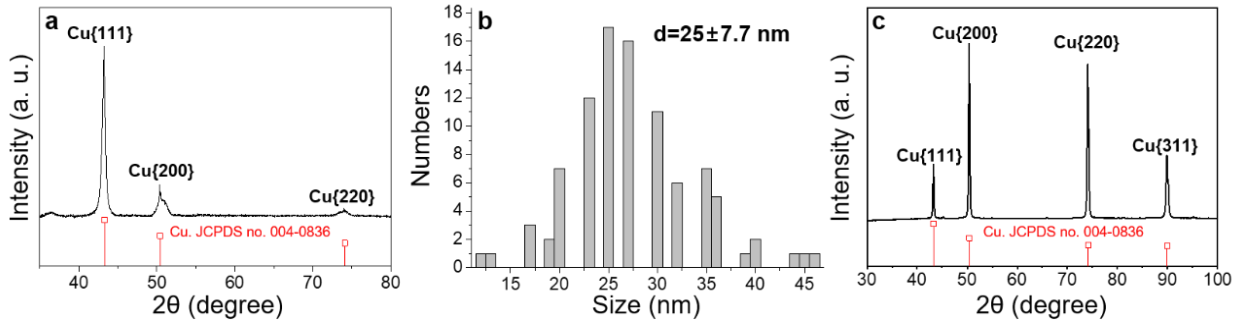

Figure 3-2. (a) PXRD of Syn-CuNWs, (b) Size of Syn-CuNWs. The size was determined by averaging more than 100 NWs. (c) PXRD of polycrystalline Cu-foil.

High-resolution TEM shows that these NWs have flat surfaces containing surface oxidation and amorphous carbons in figure 3-3a. A fast Fourier transform of the surface of Syn-CuNWs in figure 3-3a exhibits a superimposition of two face-centered cubic (FCC) patterns, i.e. [001] zone axis (T1, twin 1) and [112] zone axis (T2, twin 2)[53], indicating the [110] growth direction of the

Syn-CuNW with twin planes. Figure 3-3a shows the Cu(220) index, matching with the CuNWs growth direction[52].

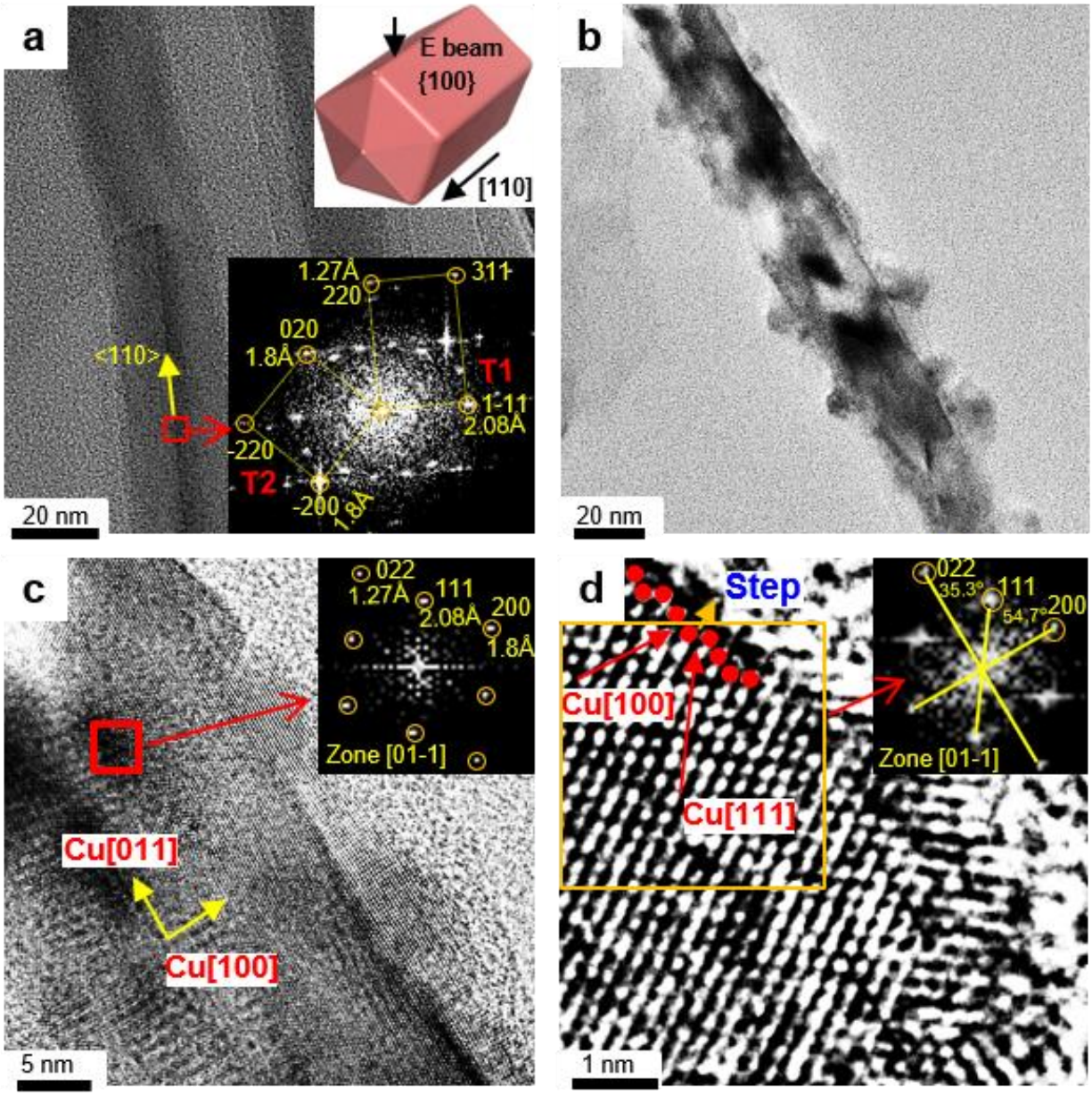

Figure 3-3. TEM characterizations of the Syn-CuNW and A-CuNW. (a) Low magnification TEM image of Syn-CuNWs (insets: schematic illustration (top) and FFT (bottom) of a Syn-CuNW, showing electron beam direction, <110> NW axial growth direction and expressed {100} side

facets), (b) Low magnification TEM image of A-CuNW, (c) HRTEM image of A-CuNW (inset: FFT of the corresponding Cu phase, indicating <110> axial direction and expression of {100} planes on the side surface. (d) HRTEM image of an A-CuNW surface indicating step structure (insert: FFT from yellow box).

To activate the CuNWs surface for generation of rich surface steps, the prepared 10 µL Syn-CuNWs catalyst ink was deposited on the 5 mm diameter glassy carbon electrode and was subsequently subject to a high reduction bias (V= -1.05 V) over 1 h. After this electrochemical activation, activated CuNWs (termed A-CuNWs) showed highly uneven surfaces in figure 3-3b and figure 3-4.

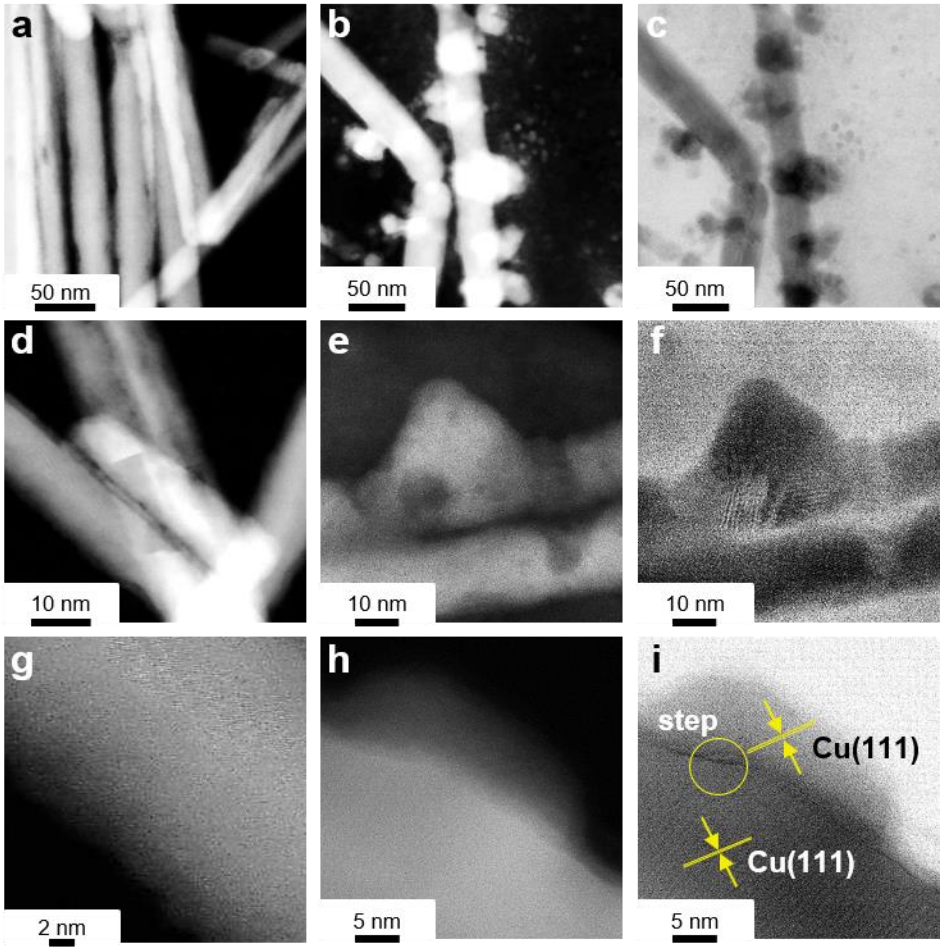

Figure 3-4. CuNWs structure change after the activation process, (a) Low magnification dark field STEM image of Syn-CuNWs, (b) Low magnification dark field STEM image of A-CuNWs, (c) Low magnification bright field STEM image of A-CuNWs, (d) Dark field STEM image of Syn-CuNWs, (e) Dark field STEM image of A-CuNWs, (f) Bright field STEM image of A-CuNWs, (g) Surface of Syn-CuNWs, (h) High magnification dark field STEM image of A-CuNWs, (i) High magnification bright field STEM image of A-CuNWs.

HRTEM of A-CuNWs after one hour of activation showed zone [01-1] of fast Fourier transform spots. The plane spacing in zone [01-1] of the FFT spots shows 2.08 Å, 1.80 Å and 1.27 Å, which were indexed as Cu{111}, Cu{200} and Cu{220}, respectively[52,53]. Both the Cu_2O and Cu phases were found on the A-CuNW surface with the <110> axial direction and <100> towards the sides, which suggests a {100}-rich side surface in figure 3-3c and figure 3-5. The Cu_2O observed in HRTEM on the surface of the A-CuNWs was probably due to the instant surface oxidation after removing the reduction potential[22], which will convert back to Cu under applied reduction potentials of about −0.8 to −1.1 V[54]. The HRTEM images indicate surface steps in the form of S-[n(100) x m(111)] and S-[n(111) x m(100)] on the A-CuNWs surface in figure 3-3d and figure 3-5f.

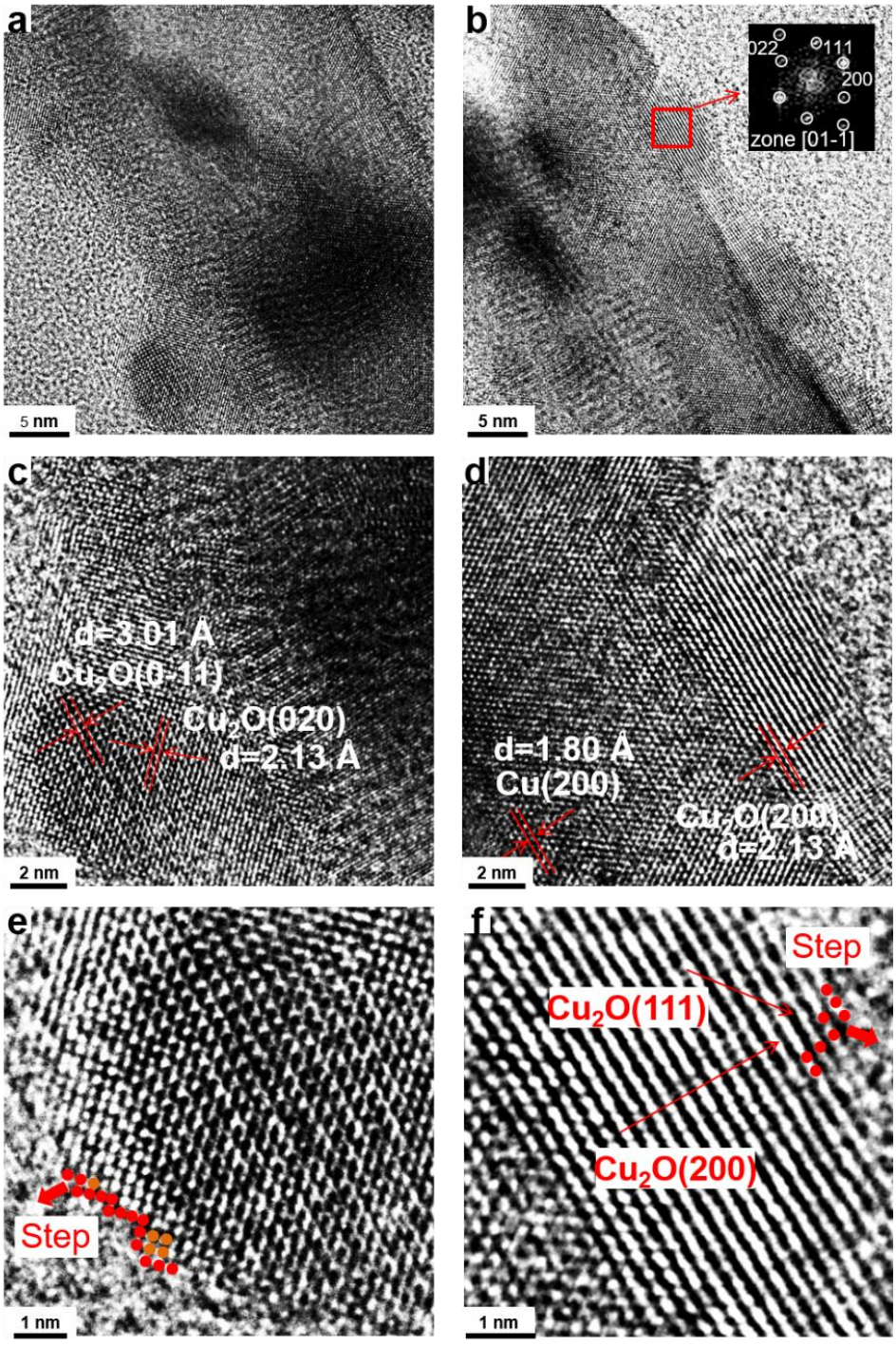

Figure 3-5. The highly stepped surface of A-CuNWs after the activation process, (a), (b) FFT on parts of A-CuNW, (c), (d) HRTEM images of the surface of A-CuNW, (e) [n(001) x (011)] steps on the surface of A-CuNW, (f) [n(100) x (111)] on the surface of A-CuNW.

I also observed (100) terraces next to n multiple steps of (110) (S-[n(100) x (110)]) in figure 3-5e. Secondary electron imaging from scanning transmission electron microscopy mode also confirms pronounced surface step morphology of the A-CuNWs compared to Syn-CuNWs in figure 3-6.

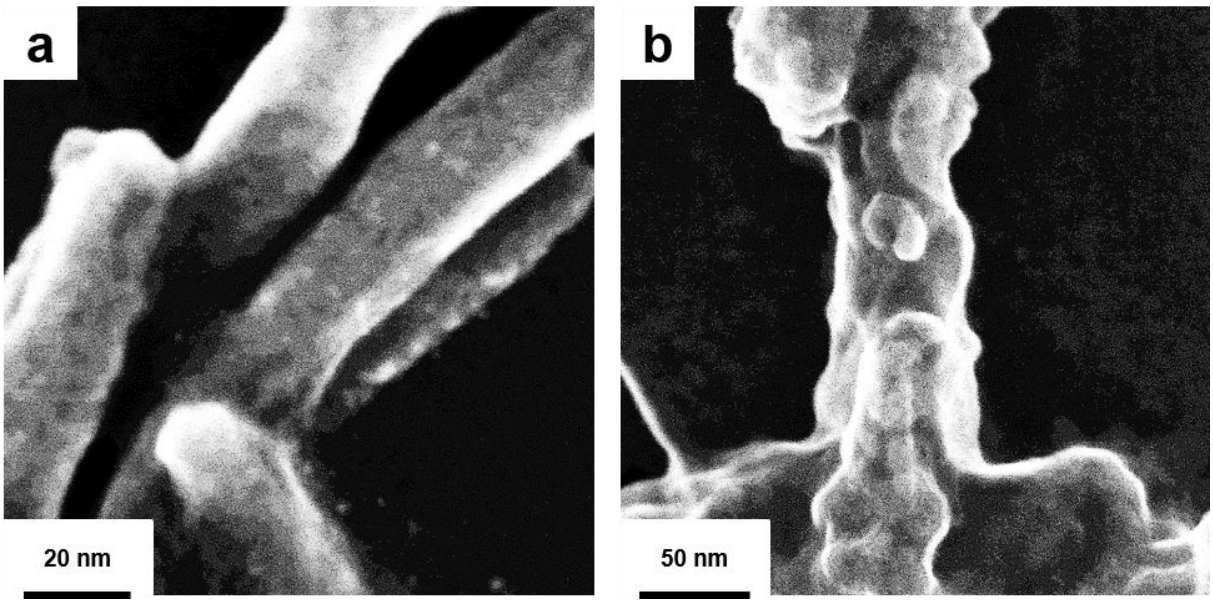

Figure 3-6. (a) SEI of Syn-CuNWs, (b) SEI of A-CuNWs.

In addition, Pb under potential deposition at room temperature in N_2-saturated 0.1 M $HClO_4$ + 0.001 M $Pb(ClO_4)_2$ solution[43] in figure 3-7 reveals that the electrochemical surface area of the A-CuNWs is higher than that of the Syn-CuNWs (1.68 $m^2/g \rightarrow 3.07$ m^2/g) in figure 3-7. Thus, the surface activating process produced A-CuNWs with stepped surfaces and larger ECSA compared to the Syn-CuNWs catalyst. Besides, electrochemical impedance spectroscopy (EIS) showed that the A-CuNWs catalyst demonstrated similar and slightly lower ohmic resistance (3 Ω less) than that of the Syn-CuNWs in figure 3-8

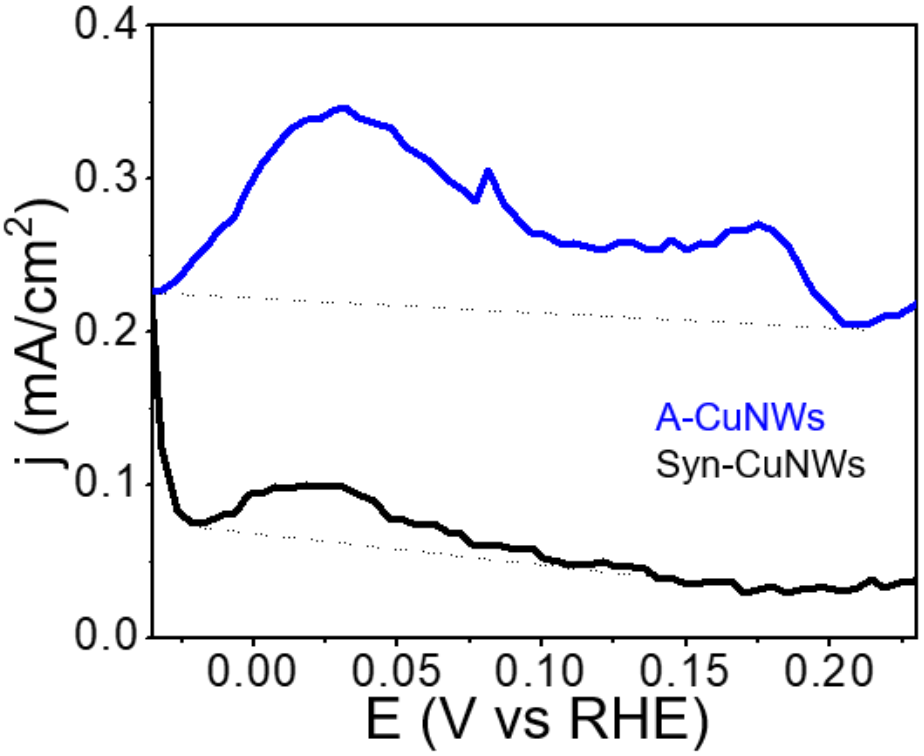

Figure 3-7. Pb under-potential deposition of Syn-CuNWs (black line) and A-CuNWs (blue line) to extract ECSA measured in N_2-saturated 0.1 M $HClO_4$ + 0.001 M $Pb(ClO_4)_2$ solution at room temperature. The background current (dotted lines) were measured in N_2-saturated 0.1 M $HClO_4$.

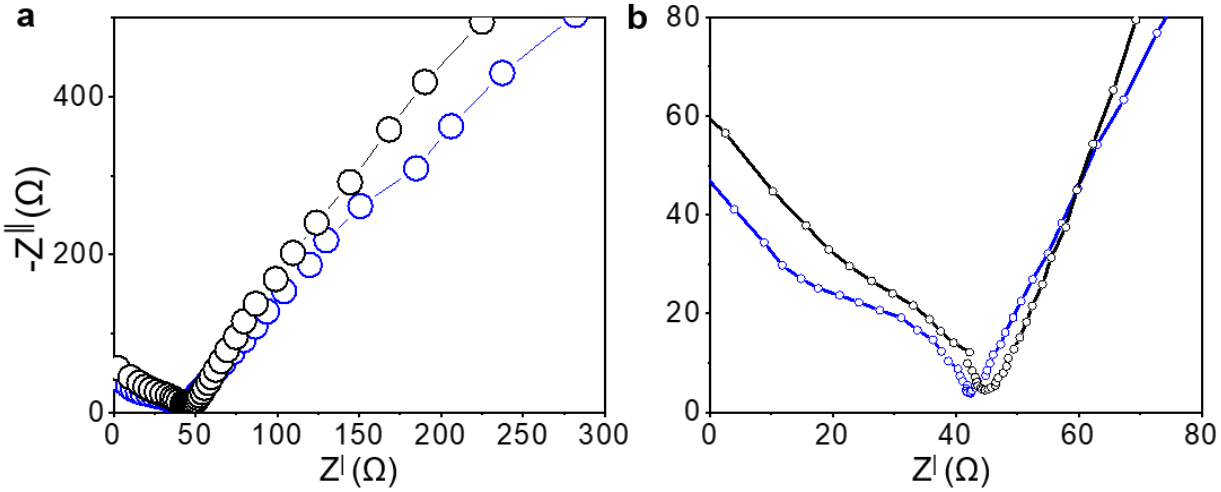

Figure 3-8. (a, b) Nyquist plot of Syn-CuNWs (black) and A-CuNWs (blue).

3.3.2 Characterization of the stepped surface

To further evaluate the CuNWs surfaces, we conducted a $Cu \leftrightarrow Cu_2O$ redox reaction cyclic voltammetry in 0.1 M KOH from 0.13 V to 0.68 V at 100 mV/s scan rate in figure 3-9. Before the activation process, the Syn-CuNWs catalyst showed OH^- adsorption peaks at 0.362 and ~ 0.395 in figure 3-10a, which matches well with the OH^- adsorption sites on Cu facets ($Cu(OH)_{ad}$) reported in the previous studies[42,55-57]. A very sharp adsorption peak at 0.362 V matches with the OH^- adsorption on Cu{100} facet perfectly, and the ~ 0.395 V peak matches with the OH^- adsorption on the Cu{110} facet[55-57].

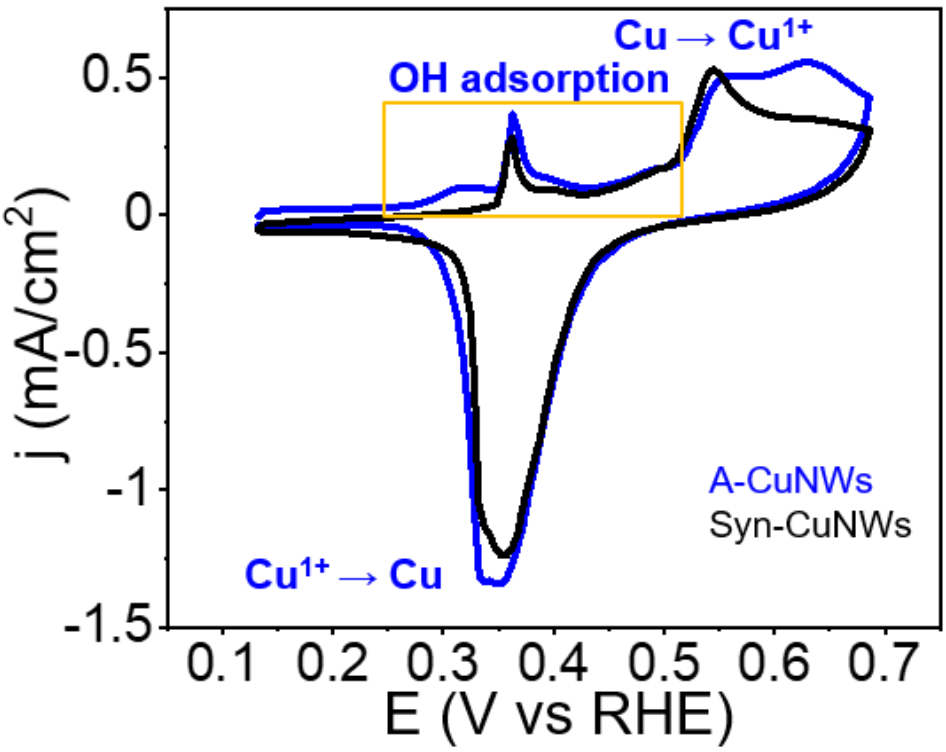

Figure 3-9. Redox reaction of Syn-CuNWs and A-CuNWs in 0.1 M KOH at 100 mV/s scan rate. Cu(100) at ~0.362 V, Cu(110) at 0.395 – 0.43 V, Cu(111) at ~0.492 V, and A-(hkl) (high energy steps) at a negative shift from Cu(100)).

Importantly, the A-CuNWs catalyst exhibits an apparent strong OH^- adsorption peak at 0.316 V in figure 3-10c. This additional peak (assigned here to A-(hkl)) appears at a more negative potential than those of the low index facets of Cu, indicating stronger OH^- adsorption[41,58]. The stronger OH^- adsorption has been suggested to appear on the surfaces with high energy steps[56,59]. Raciti et al. also reported an OH^- adsorption peak (~ 0.33 V) with a negative shift from Cu{100} peak (~ 0.35 V), which they assigned to Cu(211) (S-[3(111) x (100)])[56]. DFT calculations of Cu-O binding energy by Tian et al. also reported that the stepped surface of Cu(311) (S-[2(100) x (111)]) led to stronger Cu-O binding energy (5.17 eV) compared with 5.13 eV Cu(100) and 4.29 eV Cu(111)[59]. These results are consistent with our observations for A-CuNWs and Syn-CuNWs in figure 3-3d and figure 3-5f.

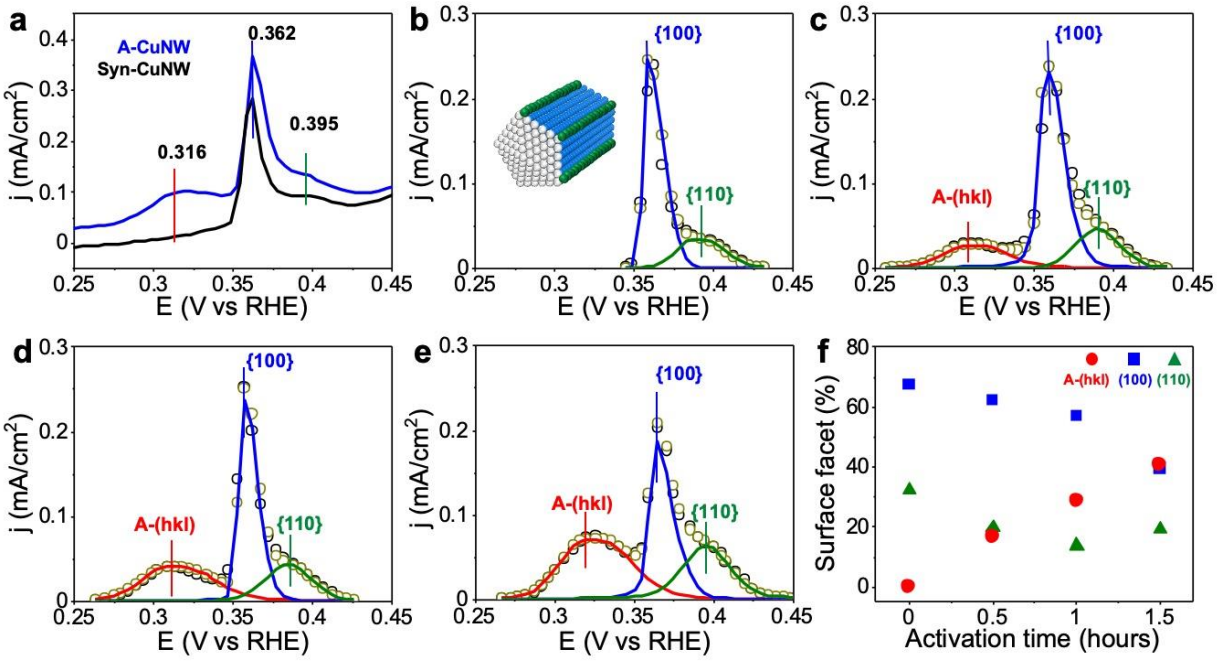

Figure 3-10. Electrochemical characterization of the surfaces of the CuNWs. (a) Redox reaction of Syn-CuNWs and A-CuNWs in 0.1 M KOH, (b-e) Fitted OH^- adsorption peaks of Syn-CuNWs (b, inset is a schematic of the corresponding Syn-CuNW structure) and A-CuNWs with different

activation duration: (c): 0.5 h, (d): 1 h and (e): 1.5h. Peaks of different colors represent different facets on the NW surfaces. Blue color - {100} facets, green color - {110} facets, and red color - A-(hkl) (high energy steps), black open circle (original data), yellow open circle (fitted data); (f) Correlation between the portion of surface facet and the activation duration on A-CuNW surface, showing increasing A-(hkl) with longer activation.

The percentage of surface planes on Syn-CuNWs and A-CuNWs catalyst was calculated by integrating each OH_{ad} peaks. I find that compared to Syn-CuNWs, A-Cu NWs catalysts exhibit a considerably high percentage (28.98%) of A-(hkl) surface, while the expressed Cu{100} and Cu{110} were reduced from 67.49% to 57.16% and from 32.5% to 13.85%, respectively, after CO_2RR at -1.05 V for 1 h in table 3-2. To further illustrate the surface characteristics of the CuNWs. I also conducted charge displacement CO adsorption to confirm the formation of the step sites in 0.1 M K_2HPO_4 + 0.1 M KH_2PO_4 (pH 6.8) saturated with CO or N_2 at 0 °C[37,60,61]. With N_2 purging, there is no visible charge displacement of CO adsorption in figure 3-11.

Table 3-2. The surface portions of OH_{ad} on each facet of all catalysts.

Reaction Time	A-(hkl) (%)	Cu{100} (%)	Cu{110} (%)
Before	0	67.49	32.50
10 min	0	73.83	26.16
30 min	17.03	62.38	20.57
1 h	28.98	57.16	13.85
1.5 h	41.12	39.50	19.37
205 h	46.82	31.58	21.58

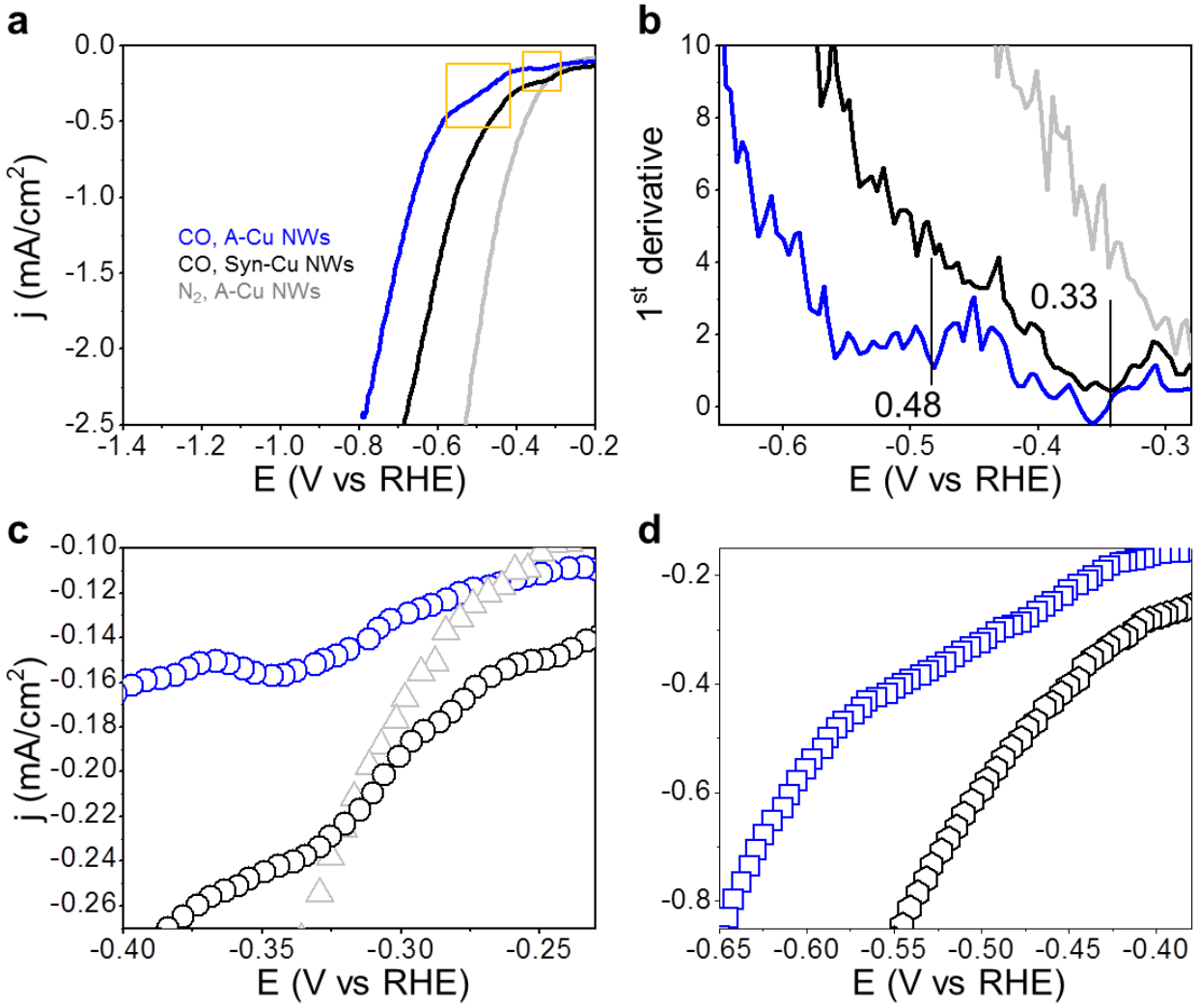

Figure 3-11. (a) CO adsorption on Syn-CuNWs catalyst and A-CuNWs catalyst in CO-saturated 0.1 M HK_2PO_4+H_2KPO_4 (pH 6.8) at 0 °C and HER of A-CuNWs catalyst in N_2 saturated 0.1 M HK_2PO_4+H_2KPO_4 (pH 6.8) at 0°C, (b) 1st derivative CO adsorption of Syn-CuNWs catalyst and A-CuNWs catalyst in 0.1 M HK_2PO_4+H_2KPO_4 (pH 6.8) at 0 °C, (c) Enlarged small orange box in CO adsorption cyclic voltammetry (CV), (d) Enlarged big orange box in CO adsorption in CV.

In contrast, with CO purging, charge displacement of CO adsorption at ~ -0.33 V corresponding to Cu{100} was found for both Syn-CuNWs and A-CuNWs. Besides, on the A-CuNWs catalyst, I also observed the appearance of a new CO adsorption peak ranging from -0.43

~ -0.55 V in figure 3-11b, d, which is consistent with the charge displacement of CO adsorption on the stepped surface of Cu[37,61]. These results all support a strong correlation between the high energy surface steps on A-CuNWs and its high C_2H_4 selectivity.

3.3.3 Electrochemical CO_2RR

I studied the CO_2RR performance for CuNWs catalyst with a gas-tight H cell by analyzing effluent gas and liquid products at different applied potentials between -0.75 and -1.2 V in CO_2-saturated 0.1 M $KHCO_3$ (pH 6.8) at room temperature and under atmospheric pressure. To assess the current density and ECSA, I loaded 0.04 mg of Cu NWs catalyst, measured by inductively coupled plasma atomic emission spectroscopy, onto the rotating disk electrode. Because most of the products from CO_2RR of our catalysts were in the gas phase, we focus our discussions of FEs on gas-phase products in table 3-3, 3-4, and 3-5. The performance of the A-CuNWs was compared to commercial Cu foil, commercial Cu NPs, and Syn-CuNWs, respectively. First, I observed that the A-CuNWs (with one hour activation) showed a considerably higher yield of C_2H_4 with an average peak FE_{C2H4} of 69.79 ± 1.44% at around −1.00 V in figure 3-12c and table 3-3, when compared with the Syn-CuNWs (FE_{C2H4} = 44.65 ± 2.20%) in figure 3-12b and table 3-4 and the polycrystalline Cu foil (FE_{C2H4} = 22.80 ± 4.60%).

Table 3-3. FEs for A-CuNWs. Each point was averaged, and the standard deviation was calculated from three independent measurements.

V (RHE)	**H_2%**	**CO%**	**CH_4 %**	**C_2H_4 %**	**Ethanol %**	**Acetate %**	**Formate %**	**Total %**
-0.76 ±0.01	74.11 ±16.37	15.56 ±11.16	0	8.10 ±3.52	0	0	1.53	99.32 ±4.44
-0.94 ±0.00	25.60 ±5.74	4.05 ±0.98	3.19 ±1.87	53.62 ±1.09	0	0	1.51	87.98 ±6.61
-0.98 ±0.00	28.82 ±2.33	3.35 ±1.47	3.18 ±4.40	67.14 ±1.56	1.50	0	0.73	104.75 ±0.73
-1.00 ±0.00	19.90 ±3.39	3.05 ±1.11	7.09 ±2.71	69.79 ±1.44	2.61	1.35	0.43	104.24 ±1.55
-1.06 ±0.00	16.30 ±4.16	1.65 ±1.28	22.22 ±3.26	59.95 ±2.82	3.39	0	0.24	103.77 ±6.78

Table 3-4. FEs for Syn-CuNWs. Each point was averaged, and the standard deviation was calculated from three independent measurements.

V (RHE)	**H_2%**	**CO%**	**CH_4%**	**C_2H_4%**	**Total%**
-0.89±0.01	63.59±15.01	4.25±0.97	0	22.05±6.02	89.90±9.92
-0.97±0.00	49.02±10.61	4.35±3.06	2.18±1.24	30.76±9.43	86.32±13.64
-1.00±0.00	44.39±7.62	2.23±0.98	6.09±1.49	44.65±2.20	97.38±10.09
-1.03±0.00	51.03±9.74	1.84±1.49	4.29±2.45	34.48±1.75	91.92±7.93
-1.07±0.00	30.44±11.94	1.76±0.69	24.43±11.27	37.25±1.84	93.90±3.00

Table 3-5. FEs for Cu foil. Each point was averaged, and the standard deviation was calculated from three independent measurements

V (RHE)	**H_2%**	**CO%**	**CH_4%**	**C_2H_4%**	**Ethanol %**	**Acetate %**	**Formate %**	**Total%**
-0.75 ±0.01	94.89 ±2.26	2.04 ±2.95	0	0	0	2.08	4.79	103.81 ±3.82
-0.86 ±0.00	73.87 ±3.17	1.51 ±1.40	0.95 ±0.62	2.17 ±1.09	0	1.68	2.91	83.12 ±3.73
-0.93 ±0.00	77.87 ±11.82	6.76 ±5.17	2.42 ±1.22	6.74 ±2.73	0.31	0.46	2.39	96.96 ±8.13
-1.04 ±0.00	46.96 ±4.49	4.36 ±5.59	24.67 ±5.15	22.80 ±4.60	0.91	0.18	0.65	100.53 ±6.71
-1.07 ±0.01	35.59 ±0.62	1.67 ±0.25	40.97 ±2.49	24.81 ±1.38	0.89	0.09	0.22	104.25 ±3.03

I note that the primary CO_2RR products of the polycrystalline Cu foil were found to be CH_4 (24.67 ± 5.15%) and C_2H_4 (22.80 ± 4.60%) around −1.04 V in table 3-5, which is consistent with a previously reported CO_2RR of Cu polycrystalline foil[60].

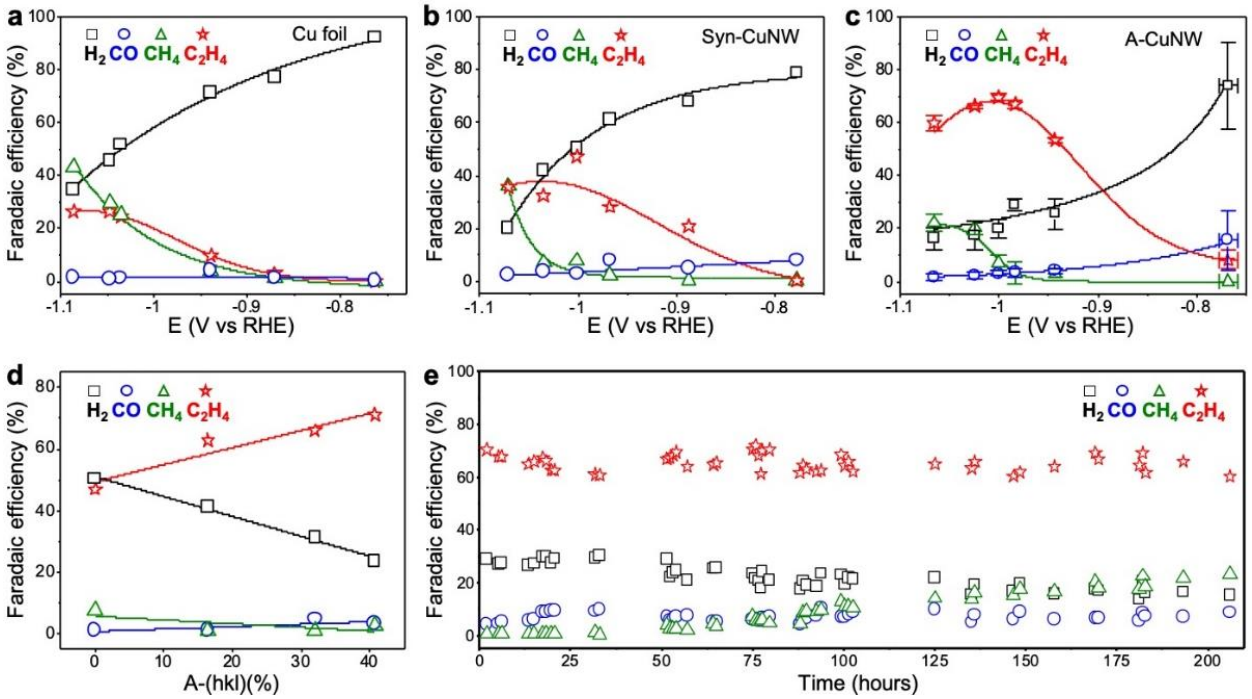

Figure 3-12. Electrochemical CO_2RR performance. (a) FEs of Cu foil, (b) FEs of Syn-CuNWs, (c) FEs of A-CuNWs (The error bars in c in the Y-direction are the standard deviation of each FE. The error bars in the X-direction are the standard deviation of iR-corrected potential. Each error bar was calculated from three independent measurements), (d) Correlation between A-(hkl) and FEs at ~ -0.99 to -1.00 V (RHE), (e) Stability test of A-CuNW catalysts at corrected potentials ranging from ~ -0.97 to ~ -1.07 V (RHE).

Overall, the A-CuNWs catalyst showed better CO_2RR performance with higher partial current densities of CO, CH_4, and C_2H_4 than the Syn-CuNWs. And the A-CuNWs catalyst demonstrates a higher partial current density of FE_{C2H4} at all applied potentials than Syn-CuNWs catalyst in figure 3-13a. On the other hand, the Syn-CuNWs catalyst exhibits a higher partial current density of HER in figure 3-13d.

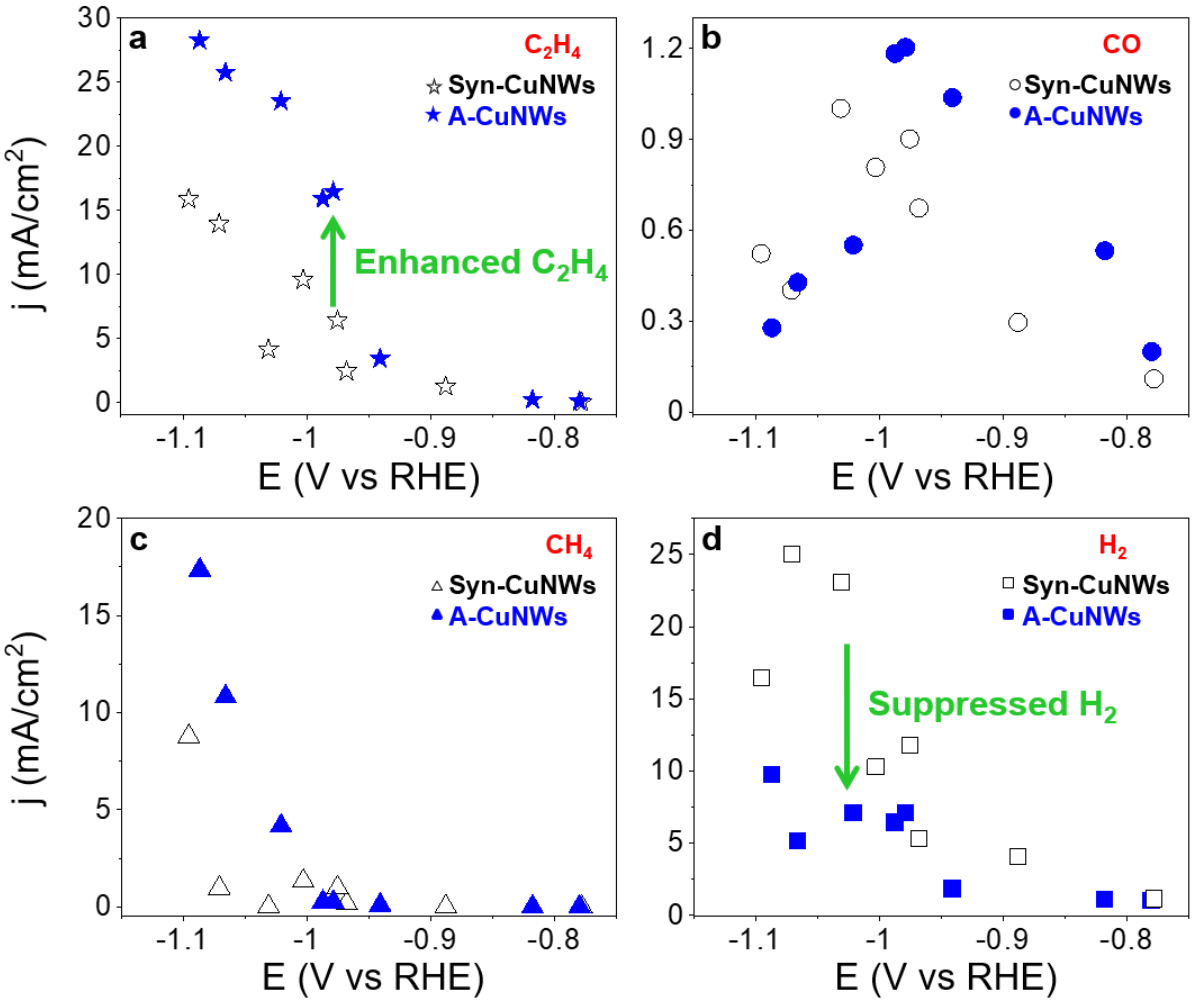

Figure 3-13. (a-d) Partial current density of Syn-CuNW and A-CuNW catalysts for each product.

It has been reported that a high surface roughness could lead to enhanced C_2H_4 production[12], so I further compared the FE_{C2H4} between commercial 25 nm Cu NPs and the A-CuNWs. I found

that A-CuNWs showed less surface roughness but still exhibited a FE_{C2H4} about 30% higher than that of the commercial 25 nm Cu NPs ($37.08 \pm 6.87\%$ FE_{C2H4} at -1.00 ± 0.01 V) in figure 3-14b, which rules out the likely contribution from the sample surface roughness to product selectivity. Hence, I tentatively attribute the high C_2H_4 selectivity observed in A-CuNWs to their highly stepped surface.

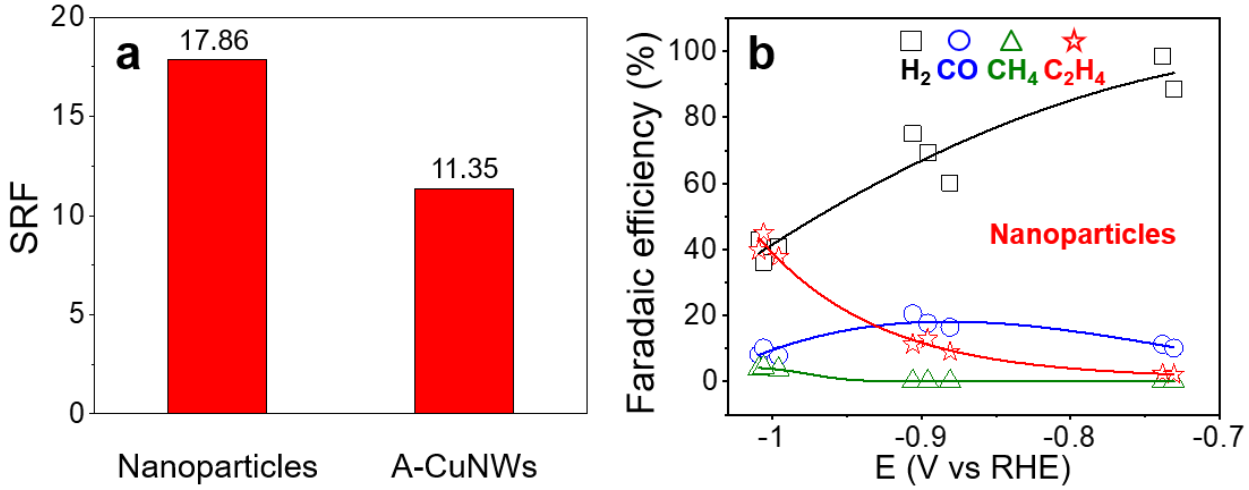

Figure 3-14. (a) Surface roughness factor (SRF) of commercial-Cu nanoparticles and A-CuNWs, (b) FEs for commercial-Cu nanoparticles. The SRF was calculated from CV of electrochemical double-layer from 152 to 202 mV by changing scan rates.

To further confirm the correlation between FE_{C2H4} and the stepped-surface structure A-(hkl), I further compared different products from A-CuNWs with different activation durations and thus different surface portions of A-(hkl). Indeed, a clear correlation was observed between FE_{C2H4} and A-(hkl). Specifically, as the stepped surface A-(hkl) gradually increased from 0 to 40.68%, the FE_{C2H4} correspondingly increased from 47.04 to 71.19% in figure 3-12d. At the same time, I observed decreasing FE_{CH4} and FE_{H2} values with increasing A-(hkl) in figure 3-12d.

Remarkably, these A-CuNWs with stepped surfaces exhibit superior structural and chemical stability during CO_2RR. The A-CuNWs catalyst showed tremendous stability in C_2H_4 production (61% ~ 72% FE_{C2H4} for 205 h at corrected potentials ranging from -0.98 to ~ -1.07 V) in figure 3-12e. In comparison, the Cu foil only showed less than 2 h stability at 20 ~ 34% FE_{CH4} at -1.07 V in figure 3-15.

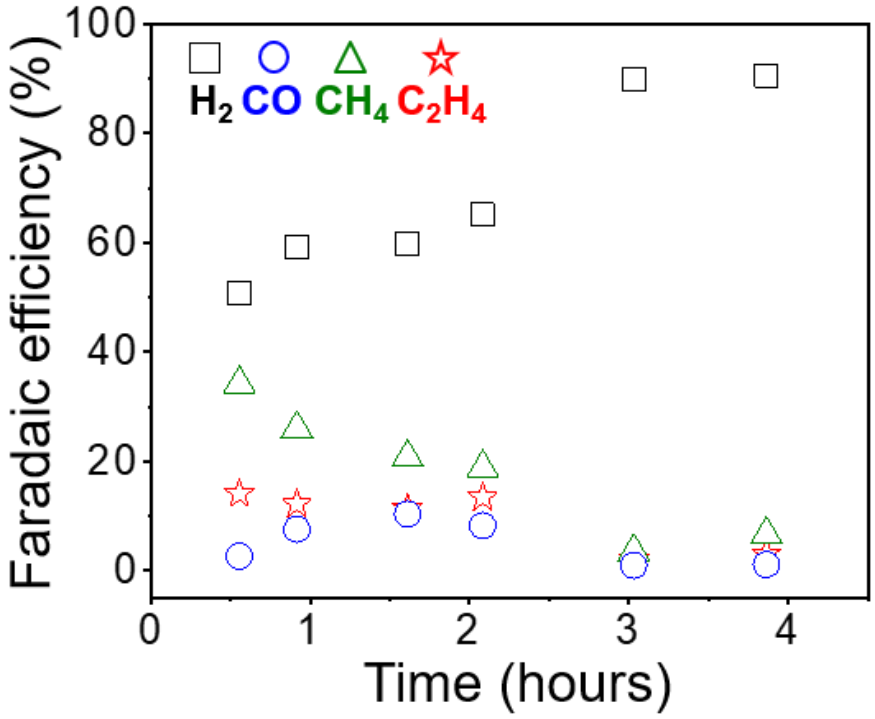

Figure 3-15. Stability of Cu foil at -1.07 V in 0.1 M $KCHO_3$.

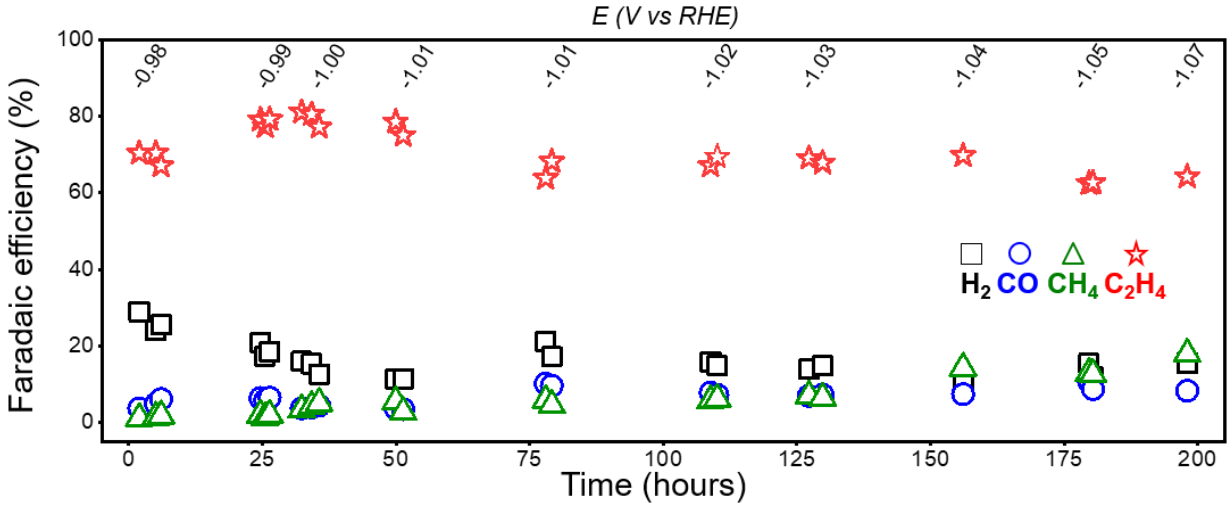

Figure 3-16. Stability test of A-CuNW catalysts at potential ranging from -0.98 to -1.07 V (RHE) for 198 hours, Top axis indicates corrected potential.

A repeated stability test that lasted 198 hours further confirmed the sustainable high performance of A-CuNWs with 64–79% FE_{C2H4} in figure 3-16. The sustained high FE_{C2H4} suggested a high stability of the A-(hkl) surface steps on A-CuNWs. Additionally, the SEI images confirmed that the A-CuNWs retained their one-dimensional morphology and stepped surface topology after the long-term stability tests in figure 3-17a, b, c.

Indeed, the OH_{ad} spectra of A-CuNWs showed that the A-(hkl) portion remained at a stable range within 45.40 ± 5.62% for ~200 hours after the initial activation period (~1.5 hours) in figure 3-18a. I also observed that during the stability test, the A-(hkl) continued to increase slightly with the ongoing CO_2RR after the initial 1.5 hours of activation in figure 3-18a, correspondingly led to a further increase in FE_{C2H4} figure 3-18d. The highest FE_{C2H4} (79%) was hence achieved around 24 hours into the reaction during the stability test, which corresponded to an A-(hkl) of around 50% in figure 3-16 and figure 3-18d. Averaging over 16 FE measurements during the stability tests at a potential of around −1 V, I obtained a remarkably high FE_{C2H4} of ~77.40 ± 3.16% in table 3-6. Together, the A-CuNWs demonstrated a remarkably high FE_{C2H4} while maintaining their exceptional stability for 200 hours of continuous operation in a H-cell in table 3-6 and table 3-7

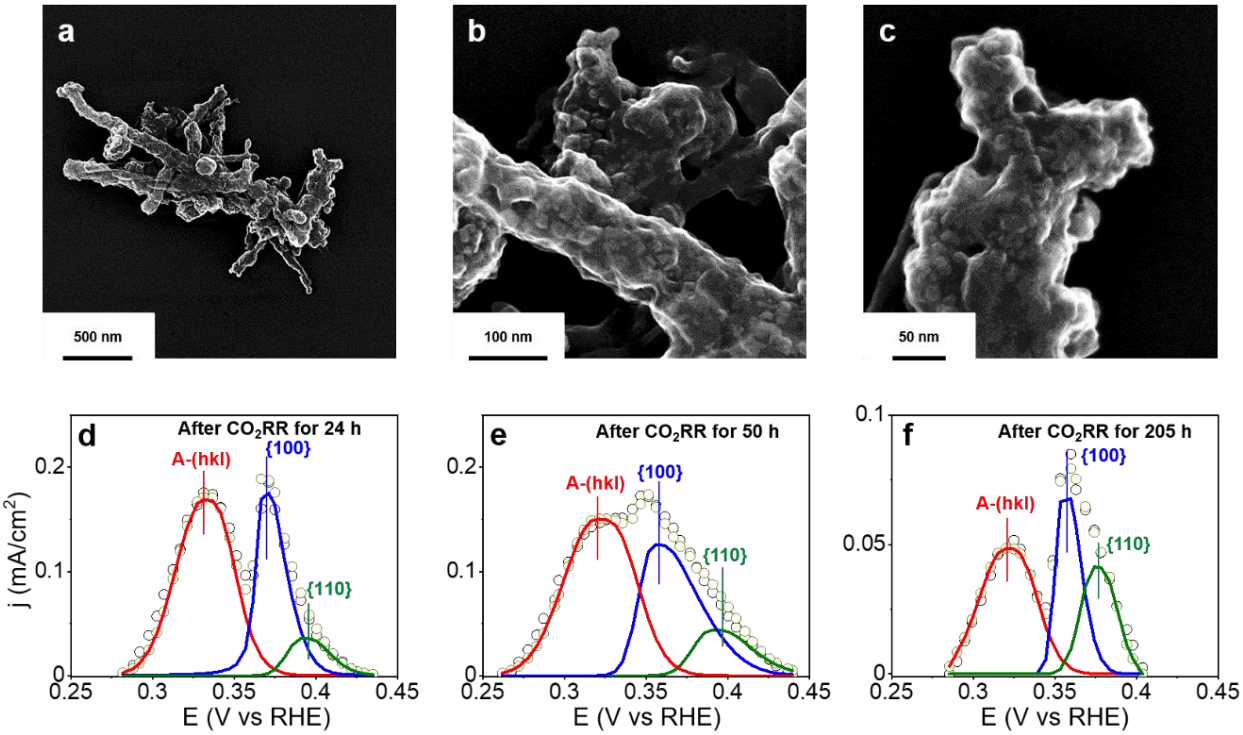

Figure 3-17. (a) Low magnification SEI of A-CuNW catalysts after CO_2RR for 205 h, (b), (c) High magnification SEI of A-CuNW catalysts after CO_2RR for 205 h. (d) OH^- adsorption of CuNWs after CO_2RR for 24 h, (b) after CO_2RR for 50 h, (c) after CO_2RR for 205 h. Cu(100) at ~0.362 V (blue color), Cu(110) at 0.395 – 0.43 V (green color), and A-(hkl) (high energy steps_red color) at a negative shift from Cu(100).

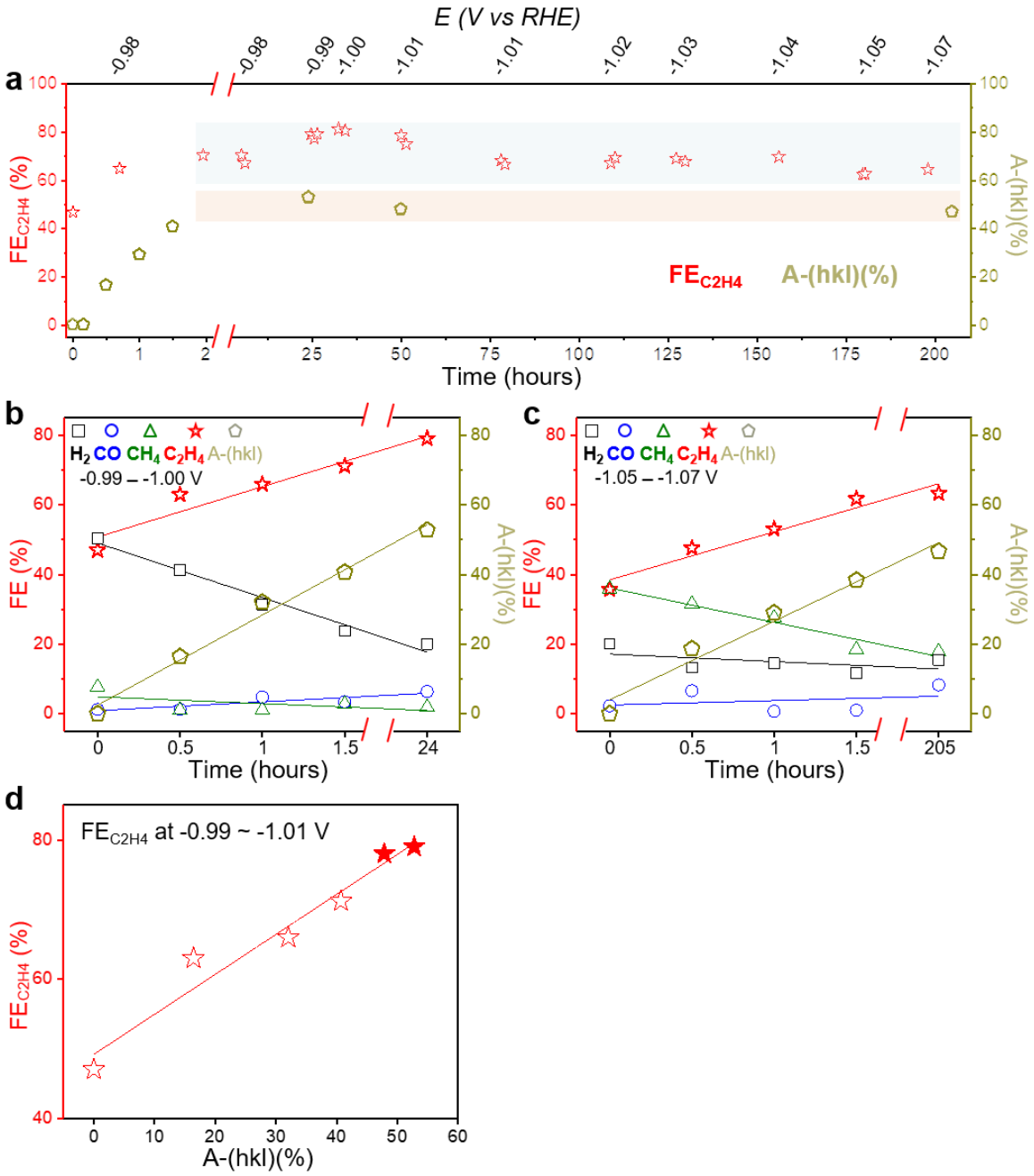

Figure 3-18. (a) Correlation between A-(hkl) and FE$_{C2H4}$ over the long-term stability test (x-axis is broken at 2.1 h, 0 – 1.5 h correspond to activation period); (b) Correlation of both A-(hkl) and FEs with activation times at -0.99 V – -1.00 V (RHE); (c) Correlation of both A-(hkl) and FEs with activation times at -1.05 V – -1.07 V (RHE), (d) Correlation of A-(hkl) and FE$_{C2H4}$ including data points from stability tests (indicated by solid red stars).

Table 3-6. Comparison of CO_2RR in peak C_2H_4 production for different Cu-based catalysts in H-cells. The FE_{C2H4} of A-CuNWs was averaged from 16 measurements in the stability tests.

Catalysts	**Applied potentials V (RHE)**	**J_{C2H4} mA/cm^2**	**Max FE_{C2H4}**	**Electrolyte**	**CO_2 Flow rate (sccm)**	**Source**
A-CuNWs	**-1.01 ±0.01**	**~17.3**	**77.40 ±3.16%**	**0.1 M $KHCO_3$**	**15**	**This work**
Cu Nanocube (250 - 300 nm)	-0.95	11.2	45%	0.1 M $KHCO_3$	20	(62)
Cu Nanocube (10 - 40 nm)	~ -0.86	6.7	33%	0.1 M $KHCO_3$	20	(63)
Plasma treated Cu foil	-0.90	7.2	60%	0.1 M $KHCO_3$	30	(14)
Electro-ReDeposited-Cu	-1.20	22.2	39%	0.1 M $KHCO_3$	20	(64)
Branched CuO NPs	-1.05	~17.0	~70%	0.1 M $KHCO_3$	60	(65)
Cu-based NPs	-1.10	~10.0	57%	0.1 M $KHCO_3$	20	(66)

Table 3-7. Summary of stability of C_2H_4 production in H-cell.

Catalysts	**Applied potential V (RHE)**	**Stable FE_{C2H4}**	**Reported Duration (hours)**	**Electrolyte**	**CO_2 Flow rate (sccm)**	**Source**
A-CuNWs	**-0.97 – -1.07**	**61 – 72%**	**205**	**0.1 M $KHCO_3$**	**15**	**This work**
A-CuNWs	**-0.98 – -1.07**	**64 – 79%**	**198**	**0.1 M $KHCO_3$**	**15**	**This work**
Cu Nanocube (250 – 300 nm)	- 0.95	45%	1	0.1 M $KHCO_3$	20	(62)
Cu Nanocube (10 – 40 nm)	- 0.75	~32%	10	0.1 M $KHCO_3$	20	(63)
Plasma treated Cu foil	- 0.9	60%	5	0.1 M $KHCO_3$	30	(14)
Electro-redeposited Cu	- 1.2	40 – 45%	5	0.1 M $KHCO_3$	20	(64)
CuZn nanoparticles	- 1.3	~30%	8	0.1 M $KHCO_3$	20	(67)

3.3.4 Ethylene production

The observation of a long-term stability of the high-index A-(hkl) surface is rather counterintuitive and intriguing, as high-energy surface steps were generally believed to be less stable than the low-index ones. To this end, we sought to assess the stability of the stepped surface under the working conditions. We performed grand canonical DFT calculations based on the Cu(S)-[n(100) x m(111)] stepped surface to construct the surface phase diagram. In figure 3-19a,b show the surface energies for Cu(100), Cu(111) and Cu(511) (Cu(S)-[3(100) x (111)]) as a function of RHE potential. On Cu(100), we find one monolayer (ML) hydrogen (H) for U < -0.07 V and 2 ML H for U < -0.83 V for most equilibrium H coverage (θ_H). On Cu(511), we find 1 ML H for U < -0.10 V, 1.33 ML H for U < -0.74 V and further increase of H* evoke a severe surface reconstruction. On Cu(111), 1 ML H (U < -0.08 V) is the maximum coverage, which allows a local minimum of H* without any imaginary frequency. At U = -0.98 ~ -1.06 V, Cu(511) with θ_H = 1.33 has the lowest surface energy compared with the Cu(100) with θ_H = 2 and Cu(111) with θ_H = 1 in figure 3-19a, b. Therefore, we expect that once the stepped surface is formed, there is no driving force to reconstruct back to the flat Cu(100) surface at working potential, which provides good stability of stepped surfaces.

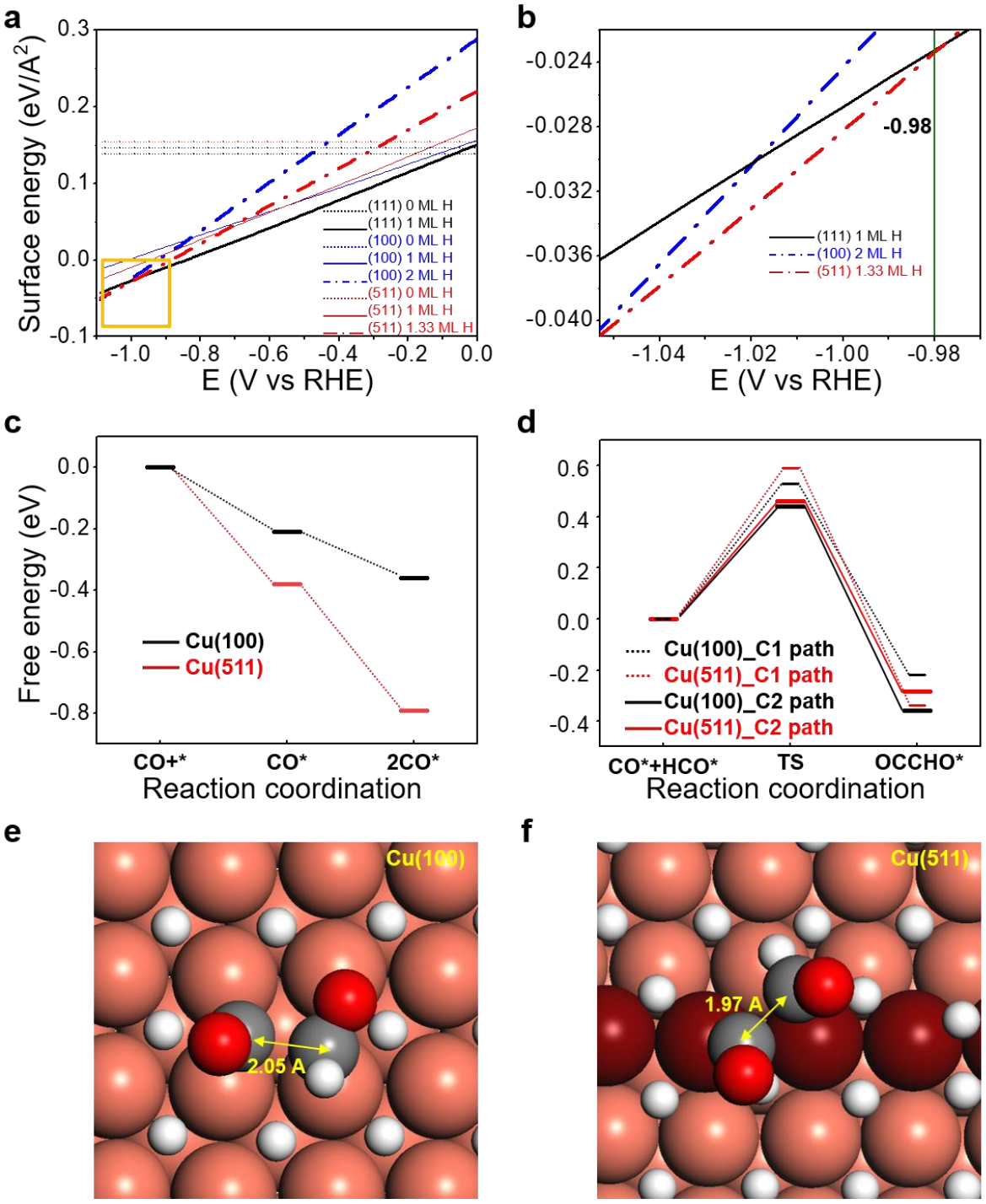

*Figure 3-19. DFT calculations on the stability of the Cu(511) step surface and the formation energy of *OCCHO. (a) Surface phase diagram of Cu(100) and Cu(511) (Cu(S)-[3(100) x (111)]) for 0 ML, 1 ML H and the highest stabilized H coverages as a function of potentials at pH 7, (b)*

Magnified view of the yellow box in figure 3-19a, (c) CO, and 2CO adsorption energies (ΔG_{ads}) on Cu(100) and Cu(511), The CO+ represents CO and an active site on the surface before the adsorption of CO; the CO* represents the active site with CO adsorption. (d) C1 and C2 pathway on Cu(100) and Cu(511), Transition states for C2 pathway on (e) Cu(100) and (f) Cu(511). Orange, gray, red, and white balls stand for Cu, C, O, and H, respectively.*

We also calculated CO adsorption free energies to verify if the stepped surface is beneficial for CO adsorption since the CO population is a key factor for C2+ products. We found that the step on Cu(511) has 0.17 eV higher affinity to a single CO adsorption compared to Cu(100) shown in table 3-8. Besides, the two adjacent molecular CO adsorption can occur cooperatively with 0.44 eV more stable on the step sites on Cu(511) in contrast to Cu(100) where c(2×2)-CO adlayer structure is observed in operando STM study[68]. Therefore, we confirm that the step on Cu(511) can secure a higher local CO surface population, and this facet is also favorable for two adjacent CO adsorption, which is beneficial for C-C coupling.

Table 3-8. CO adsorption energies (ΔG_{ads}), kinetic barriers ($\Delta G^{\ddagger}$) and free energy changes (ΔG) for C1, C2 pathways by 1 ML of H.*

	1CO*	**2CO***	**HCO* → HCOH***		**CO*+HCO* → OCCHO***	
	ΔG_{ads}	**ΔG_{ads}**	**$\Delta G^{\ddagger}$**	**ΔG**	**$\Delta G^{\ddagger}$**	**ΔG**
Cu(100)	-0.21	-0.36	0.53	-0.22	0.44	-0.36
Cu(511)	-0.38	-0.80	0.59	-0.34	0.46	-0.28

Next, we performed DFT to explain the reaction kinetics. The OCCHO* intermediate, an important intermediate toward the production of C2 productions especially at higher overpotentials[69-71], while the HCO* intermediate can branch out to form either HCOH* for the C1 pathway or OCCHO* for the C2 pathway. We calculated the reaction energy barriers ($\Delta G^{\ddagger}$) and reaction free energies (ΔG) for each pathway, as shown in table 3-8. All frequency contributions are listed table 3-1. For kinetic barrier calculations for the protonation of HCO* intermediate into HCOH*, we introduced a surface water molecule as a proton source at pH 6.8. The reduction of HCO* to HCOH* occurs with $\Delta G^{\ddagger}$ = 0.53 eV on Cu(100) and $\Delta G^{\ddagger}$ = 0.59 eV on Cu(511), respectively. So the Cu(511) has 0.06 eV higher reaction barrier from HCO* to HCOH*, which is ten times slower than that on the Cu(100) at 298 K. On the other hand, despite the fact that the high stability of 2CO* configuration, the kinetic barrier for C-C coupling from CO*+HCO* toward OCCHO* (C2 pathway) on Cu(511) is only 0.02 eV higher compared to that on Cu(100), so only two times slower than that on Cu(100). We also performed DFT calculations for hydrogen binding energy (HBE) on Cu(100), and various adsorption sites on Cu(511) to estimate HER activity based on the fact that low HER activity for Cu is attributed to the weak HBE[72]. The HBE for Cu(100) are -0.31 eV (4 fold), respectively. On the other hand, on Cu(511), we considered 8 H* binding sites, and all of them have less HBE compared to Cu(100) in figure 3-20, which indicates the suppression of HER on Cu(511).

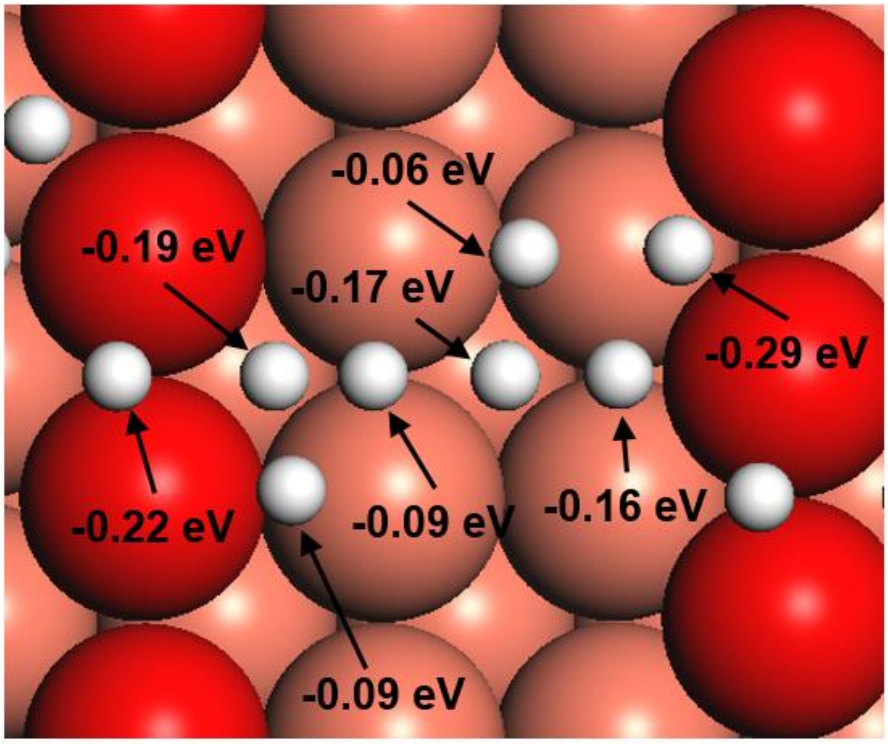

Figure 3-20. The H binding energies of eight possible binding sites on Cu(511). Cu atoms on the step are indicated by red.*

Thus, we suggest that the high local population of 2CO*, the higher barrier for the C1 path on Cu(511) and the slower HER are the key factors that underlie the enhancement in C2 production observed on A-CuNWs. These results are all consistent with the experimental observations that an increasing surface ratio of the stepped surface A-(hkl) led to an increase FE_{C2H4} and a decrease in both FE_{CH4} and FE_{H2} in figure 3-12d and figure 18b,c. In addition, the stronger OH^- adsorption on A-CuNWs can also induce longer H_2O adsorption residence times on the surface of Cu, which leads to the preference of hydrocarbon products (for example, C_2H_4) over alcohol products (for example, ethanol), which share a common intermediate with C_2H_4 (refs.[73,74]). This is consistent with the observed low ethanol production for A-CuNW catalysts in table 3-3.

3.4 Conclusion

In conclusion, I report here that CuNW catalysts with a highly stepped surface exhibit a high FE_{C2H4} ($77.40 \pm 3.16\%$) that is stable for ~200 hours in H-cells. Coupled with structural and electrochemical surface characterizations of A-CuNWs, our DFT calculations showed that the stepped surface [3(100)×(111)]) exhibits a high local population of 2CO* and a higher barrier for the C1 path compared with that for Cu(100), which leads to a higher product selectivity towards C_2H_4. These findings suggest an effective approach to engineer catalyst surfaces for high reactivity, high selectivity and high stability under operando conditions.

3.5 Chapter 3. Reference

[1] Schreier, M. *et al.* Solar conversion of CO_2 to CO using Earth-abundant electrocatalysts prepared by atomic layer modification of CuO. *Nature Energy* **2**, 17087 (2017).

[2] Lin, S. *et al.* Covalent organic frameworks comprising cobalt porphyrins for catalytic CO_2 reduction in water. *Science* **349**, 1208-1213 (2015).

[3] Gao, S. *et al.* Partially oxidized atomic cobalt layers for carbon dioxide electroreduction to liquid fuel. *Nature* **529**, 68 (2016).

[4] Hori, Y., Wakebe, H., Tsukamoto, T., & Koga, O. Electrocatalytic process of CO selectivity in electrochemical reduction of CO_2 at metal electrodes in aqueous media. *Electrochimica Acta* **39**, 1833-1839 (1994).

[5] Hori, Y., Kikuchi, K. & Suzuki, S. Production of CO and CH_4 in electrochemical reduction of CO_2 at metal electrodes in aqueous hydrogen carbonate solution. *Chemistry Letters* **14**, 1695-1698 (1985).

[6] Qiao, J., Liu, Y., Hong, F. & Zhang, J. A review of catalysts for the electro-reduction of carbon dioxide to produce low-carbon fuels. *Chemical Society Reviews* **43**, 631-675 (2014).

[7] Gawande, M. B. *et al.* Cu and Cu-based nanoparticles: synthesis and applications in catalysis. *Chemical reviews* **116**, 3722-3811 (2016).

[8] Kim, D., Resasco, J., Yu, Y., Asiri, A. M. & Yang, P. Synergistic geometric and electronic effects for electrochemical reduction of carbon dioxide using gold-copper bimetallic nanoparticles. *Nature communications* **5**, 4948 (2014).

[9] Lu, Q. *et al.* A selective and efficient electrocatalyst for carbon dioxide reduction. *Nature communications* **5**, 3242 (2014).

[10] Pan, Yuan, *et al*. Design of single-atom Co–N_5 catalytic site: a robust electrocatalyst for CO_2 reduction with nearly 100% CO selectivity and remarkable stability. *Journal of the American Chemical Society* **140,** 4218-4221 (2018).

[11] Mistry, H., Varela, A. S., Kühl, S., Strasser, P. & Cuenya, B. R. Nanostructured electrocatalysts with tunable activity and selectivity. *Nature Reviews Materials* **1**, 16009 (2016).

[12] Angamuthu, R., Byers, P., Lutz, M., Spek, A. L. & Bouwman, E. Electrocatalytic CO_2 conversion to oxalate by a copper complex. *Science* **327**, 313-315 (2010).

[13] Li, Y. *et al.* Structure-sensitive CO_2 electroreduction to hydrocarbons on ultrathin 5-fold twinned copper nanowires. *Nano letters* **17**, 1312-1317 (2017).

[14] Zhang, An, *et al*. Nickel Doping in Atomically Thin Tin Disulfide Nanosheets Enables Highly Efficient CO_2 Reduction. *Angewandte Chemie International Edition* **57**, 10954-10958 (2018).

[15] Saravanan, Karthikeyan, *et al*. Computational investigation of CO_2 electroreduction on tin oxide and predictions of Ti, V, Nb and Zr dopants for improved catalysis. *Journal of Materials Chemistry A* **5,** 11756-11763 (2017).

[16] Liu, Shan Ping, *et al*. Theoretical Studies on the CO_2 Reduction to CH_3OH on Cu (211). *Electrocatalysis* **8**, 647-656 (2017).

[17] Loiudice, A. *et al.* Tailoring copper nanocrystals towards C2 products in electrochemical CO_2 reduction. *Angewandte Chemie International Edition* **55**, 5789-5792 (2016).

[18] Fan, Lei, *et al*. Strategies in catalysts and electrolyzer design for electrochemical CO_2 reduction toward C2+ products. *Science Advances* **6**, eaay3111 (2020).

[19] Li, C. W. & Kanan, M. W. CO_2 reduction at low overpotential on Cu electrodes resulting

from the reduction of thick Cu_2O films. *Journal of the American Chemical Society* **134**, 7231-7234 (2012).

[20] Cheng, T., Xiao, H. & Goddard III, W. A. Reaction mechanisms for the electrochemical reduction of CO_2 to CO and formate on the Cu (100) surface at 298 K from quantum mechanics free energy calculations with explicit water. *Journal of the American Chemical Society* **138**, 13802-13805 (2016).

[21] Mistry, H. *et al.* Highly selective plasma-activated copper catalysts for carbon dioxide reduction to ethylene. *Nature communications* **7**, 12123 (2016).

[22] Lum, Y. & Ager, J. W. Stability of Residual Oxides in Oxide-Derived Copper Catalysts for Electrochemical CO_2 Reduction Investigated with ^{18}O Labeling. *Angewandte Chemie International Edition* **57**, 551-554 (2018).

[23] Lum, Y., Yue, B., Lobaccaro, P., Bell, A. T. & Ager, J. W. Optimizing C–C coupling on Oxide-Derived copper catalysts for electrochemical CO_2 reduction. *The Journal of Physical Chemistry C* **121**, 14191-14203 (2017).

[24] Gao, D. *et al.* Enhancing CO_2 electroreduction with the metal–oxide interface. *Journal of the American Chemical Society* **139**, 5652-5655 (2017).

[25] Favaro, M. *et al.* Subsurface oxide plays a critical role in CO_2 activation by Cu(111) surfaces to form chemisorbed CO_2, the first step in reduction of CO_2. *Proceedings of the National Academy of Sciences* 201701405 (2017).

[26] Xiao, H., Goddard, W. A., Cheng, T. & Liu, Y. Cu metal embedded in oxidized matrix catalyst to promote CO_2 activation and CO dimerization for electrochemical reduction of CO_2. *Proceedings of the National Academy of Sciences* 201702405 (2017).

[27] Choi, C., Cheng, T., Flores Espinosa, M., Fei, H., Duan, X., Goddard III, W. A., & Huang, Y. A Highly Active Star Decahedron Cu Nanocatalyst for Hydrocarbon Production at Low Overpotentials. *Advanced Materials* **31**, 1805405 (2019).

[28] Verdaguer-Casadevall, A. *et al.* Probing the active surface sites for CO reduction on oxide-derived copper electrocatalysts. *Journal of the American Chemical Society* **137**, 9808-9811 (2015).

[29] Feng, X., Jiang, K., Fan, S. & Kanan, M. W. Grain-boundary-dependent CO_2 electroreduction activity. *Journal of the American Chemical Society* **137**, 4606-4609 (2015).

[30] Li, C. W., Ciston, J. & Kanan, M. W. Electroreduction of carbon monoxide to liquid fuel on oxide-derived nanocrystalline copper. *Nature* **508**, 504 (2014).

[31] Mariano, R. G., McKelvey, K., White, H. S. & Kanan, M. W. Selective increase in CO_2 electroreduction activity at grain-boundary surface terminations. *Science* **358**, 1187-1192 (2017).

[32] Weng, Z., Wu, Y., Wang, M., Jiang, J., Yang, K., Huo, S., & Liang, Y. Active sites of copper-complex catalytic materials for electrochemical carbon dioxide reduction. *Nature communications* **9**, 415 (2018).

[33] Dai, L., Qin, Q., Wang, P., Zhao, X., Hu, C., Liu, P., & Mo, S. Ultrastable atomic copper nanosheets for selective electrochemical reduction of carbon dioxide. *Science advances* **3**, e1701069 (2017).

[34] *Research and Markets. "The Ethylene Technology Report 2016 - Research and Markets"*. *www.researchandmarkets.com*. Retrieved 19 June 2016.

[35] Cheng, T., Xiao, H., & Goddard, W. A. Full atomistic reaction mechanism with kinetics for CO reduction on Cu(100) from ab initio molecular dynamics free-energy calculations at 298 K. *Proceedings of the National Academy of Sciences* **114**, 1795-1800 (2017).

[36] Cheng, T., Xiao, H. & Goddard, W. A. Nature of the active sites for CO reduction on copper nanoparticles; suggestions for optimizing performance. *Journal of the American Chemical Society* **139**, 11642-11645 (2017).

[37] Hori, Y., Takahashi, I., Koga, O., & Hoshi, N. Selective formation of C2 compounds from electrochemical reduction of CO_2 at a series of copper single crystal electrodes. *The Journal of Physical Chemistry B* **106**, 15-17, (2002).

[38] DeWulf, David W., Tuo Jin, and Allen J. Bard. Electrochemical and surface studies of carbon dioxide reduction to methane and ethylene at copper electrodes in aqueous solutions. *Journal of the Electrochemical Society* **136,** 1686-1691 (1989).

[39] Engelbrecht, Andreas, *et al*. On the Electrochemical CO_2 Reduction at Copper Sheet Electrodes with Enhanced Long-Term Stability by Pulsed Electrolysis. Journal of The Electrochemical Society **165**, J3059-J3068 (2018).

[40] Zhu, W. et al. Monodisperse Au nanoparticles for selective electrocatalytic reduction of CO_2 to CO. *Journal of the American Chemical Society* **135**, 16833-16836 (2013).

[41] De Chialvo, M. G., Marchiano, S. L., & Arvia, A. J. The mechanism of oxidation of copper in alkaline solutions. *Journal of applied electrochemistry*, **14**, 165-175 (1984).

[42] De Chialvo, M. G., Zerbino, J. O., Marchiano, S. L., & Arvia, A. J. Correlation of electrochemical and ellipsometric data in relation to the kinetics and mechanism of Cu_2O electroformation in alkaline solutions. *Journal of Applied Electrochemistry* **16**, 517-526 (1986).

[43] Baturina, O. A. *et al.* CO_2 electroreduction to hydrocarbons on carbon-supported Cu nanoparticles. *Acs Catalysis* **4**, 3682-3695 (2014).

[44] Kresse, G., Furthmüller, J., & Hafner, J. Theory of the crystal structures of selenium and tellurium: the effect of generalized-gradient corrections to the local-density approximation. *Physical Review B* **50**, 13181 (1994).

[45] Kresse, G., & Furthmüller, J. Efficiency of ab-initio total energy calculations for metals and semiconductors using a plane-wave basis set. *Computational materials science* **6**, 15-50 (1996).

[46] Kresse, G., & Furthmüller, J. Efficient iterative schemes for ab initio total-energy calculations using a plane-wave basis set. *Physical review B* **54**, 11169 (1996).

[47] Perdew, J. P., Burke, K., & Ernzerhof, M. Generalized gradient approximation made simple. *Physical review letters* **77**, 3865 (1996).

[48] Kresse, G., & Joubert, D. From ultrasoft pseudopotentials to the projector augmented-wave method. *Physical Review B* **59**, 1758 (1999).

[49] Grimme, S., Antony, J., Ehrlich, S., & Krieg, H. A consistent and accurate ab initio parametrization of density functional dispersion correction (DFT-D) for the 94 elements H-Pu. *The Journal of chemical physics* **132**, 154104 (2010).

[50] Mathew, Kiran, *et al*. Implicit solvation model for density-functional study of nanocrystal surfaces and reaction pathways. *The Journal of chemical physics* **140**, 084106 (2014).

[51] Henkelman G. & Jo´nsson, H. Improved tangent estimate in the nudged elastic band method for finding minimum energy paths and saddle point. *The Journal of chemical physics* **113**, 9978 (2000).

[52] Jin, M., He, G., Zhang, H., Zeng, J., Xie, Z., & Xia, Y. Shape-controlled synthesis of copper nanocrystals in an aqueous solution with glucose as a reducing agent and hexadecylamine as a

capping agent. *Angewandte Chemie International Edition*, **50**, 10560-10564 (2011).

[53] Yang, H. J., He, S. Y., & Tuan, H. Y. Self -seeded growth of five-fold twinned copper nanowires: mechanistic study, characterization, and SERS applications. *Langmuir* **30**, 602-610, (2014).

[54] Mandal, Lily, *et al*. Investigating the role of copper oxide in electrochemical CO_2 reduction in real time. *ACS applied materials & interfaces* **10**, 8574-8584 (2018).

[55] Droog, J. M., & Schlenter, B. Oxygen electrosorption on copper single crystal electrodes in sodium hydroxide solution. *Journal of Electroanalytical Chemistry*, **112**, 387-390 (1980).

[56] Raciti, David, *et al.* Low-overpotential electroreduction of carbon monoxide using copper nanowires. ACS Catalysis 7 4467-4472 (2017).

[57] Luc, Wesley, *et al.* Two-dimensional copper nanosheets for electrochemical reduction of carbon monoxide to acetate. *Nature Catalysis* **2**, 423-430 (2019).

[58] Zhang, S., Kang, P., & Meyer, T. J. Nanostructured tin catalysts for selective electrochemical reduction of carbon dioxide to formate. *Journal of the American Chemical Society* **136**, 1734-1737 (2014).

[59] Tian, Feng Hui, and Ze Xin Wang. "Adsorption of an O atom on the Cu (311) step defective surface." *The Journal of Physical Chemistry B* **108,** 1392-1395 (2004).

[60] Hori, Y., Wakebe, H., Tsukamoto, T., & Koga, O. Adsorption of CO accompanied with simultaneous charge transfer on copper single crystal electrodes related with electrochemical reduction of CO_2 to hydrocarbons. *Surface science* **335**, 258-263 (1995).

[61] Koga, O., Teruya, S., Matsuda, K., Minami, M., Hoshi, N., & Hori, Y. Infrared spectroscopic and voltammetric study of adsorbed CO on stepped surfaces of copper

monocrystalline electrodes. *Electrochimica acta* **50**, 2475-2485 (2005).

[62] Gao, D. *et al*. Plasma-activated copper nanocube catalysts for efficient carbon dioxide electroreduction to hydrocarbons and alcohols. *ACS nano* **11**, 4825-4831, (2017).

[63] Kim, Dohyung, *et al.* Copper nanoparticle ensembles for selective electroreduction of CO_2 to C2–C3 products. *Proceedings of the National Academy of Sciences* **114**, 10560-10565 (2017).

[64] De Luna, P. *et al.* Catalyst electro-redeposition controls morphology and oxidation state for selective carbon dioxide reduction. *Nature Catalysis* **1**, 103 (2018).

[65] Kim, Jinmo, *et al*. Branched Copper Oxide Nanoparticles Induce Highly Selective Ethylene Production by Electrochemical Carbon Dioxide Reduction. *Journal of the American Chemical Society* **141**, 6986-6994 (2019).

[66] Jung, Hyejin, *et al*. Electrochemical Fragmentation of Cu_2O Nanoparticles Enhancing Selective C–C Coupling from CO_2 Reduction Reaction. *Journal of the American Chemical Society* **141**, 4624-4633 (2019).

[67] Reller, C. et al. Selective electroreduction of CO_2 toward ethylene on nano dendritic copper catalysts at high current density. *Advanced Energy Materials* **7**, 1602114 (2017).

[68] Baricuatro, Jack H., *et al*. Seriatim ECSTM-ECPMIRS of the adsorption of carbon monoxide on Cu (100) in alkaline solution at CO_2-reduction potentials. Electrochemistry *Communications* **91**, 1-4 (2018).

[69] Resasco, Joaquin, *et al*. Promoter effects of alkali metal cations on the electrochemical reduction of carbon dioxide. *Journal of the American Chemical Society* **139,** 11277-11287 (2017).

[70] Montoya, Joseph H., *et al*. Theoretical insights into a CO dimerization mechanism in CO_2 electroreduction. *The journal of physical chemistry letters* **6,** 2032-2037 (2015).

[71] Bertheussen, Erlend, *et al*. Acetaldehyde as an intermediate in the electroreduction of carbon monoxide to ethanol on oxide-derived copper. *Angewandte Chemie International Edition.* **55**, 1450-1454 (2016).

[72] Zhi Wei Seh, *et al*. Combining theory and experiment in electrocatalysis: Insights into materials design. *Science* **13**, 4998 (2017).

[73] Yamamoto, S., *et al*. In situ x-ray photoelectron spectroscopy studies of water on metals and oxides at ambient conditions. *Journal of Physics: Condensed Matter* **20**, 184025 (2008).

[74] Xiao, Hai, Tao Cheng, and William A. Goddard III. Atomistic mechanisms underlying selectivities in C1 and C2 products from electrochemical reduction of CO on Cu (111). *Journal of the American Chemical Society* **139**, 130-136 (2016).

4 Chapter 4. Summary and Outlook

4.1 Concluding remarks

This dissertation demonstrates highly active defect sites on the copper catalysts for the electrochemical CO_2 reduction reaction. Electrochemical CO_2 reduction to value-added chemical feedstocks is of considerable interest for renewable energy storage and renewable source generation while mitigating CO_2 emission from human activity.

Copper represents an effective catalyst in reducing CO_2 to hydrocarbons or oxygenates but is often plagued by low product selectivity and limited long-term stability. Thus, the development of highly active catalysts at low overpotential is desired for electrochemical CO_2 reduction.

In chapter two, the high-yield synthesis of unique star decahedron copper nanoparticles electrocatalysts displaying twin boundaries and multiple stacking faults leads to low overpotentials for methane and high efficiency for ethylene production. Particularly, star decahedron copper nanoparticles show an onset potential for CH_4 production lower by 0.149 V than commercial copper nanoparticles. More impressively, star decahedron copper nanoparticles demonstrate a Faradaic efficiency of 52.43%±6.87 for C_2H_4 production at -0.993±0.0129 V. Quanterm mechanic theory indicates that the surface stacking faults and twin defects increase CO binding energy, leading to the enhanced CO_2RR performance on star decahedron copper nanoparticles.

In chapter three, the stepped surfaces on the activated copper nanowires have been generated via a simple in-situ electrochemical activation. The copper nanowires with rich surface steps exhibit remarkably high faradaic efficiency for C_2H_4 that shows Faradaic efficiency toward ethylene (FE_{C2H4}>70%), as well as exceptionally high stability for ~200 hours. Moreover, our comprehensive experimental measurement and theoretical analysis demonstrate that stepped sites having n rows of (100) terraces next to n rows of (111) steps on the surface of A-CuNWs catalyst

are responsible the observed dramatic performance enhancement. These steps are thermodynamically favored compared to Cu(100) under operating conditions, and the stepped surface favors C2 products by suppressing C1 pathway and hydrogen production.

4.2 Future outlook

Electrochemical and photocatalytic systems have been rising to reduce CO_2 to alternative fuels such as ethylene and ethanol. The electrochemical CO_2 reduction system remains a few steps more to reach the industrial level electrochemical CO_2 reduction. However, the photocatalyst system for artificial photosynthesis is still at the initial stage even though the photocatalyst system is considering the best candidate for CO_2 conversion in our society because of no need for applied potentials and electrolytes. The extremely low efficiency of CO_2 conversion(~μmol g^{-1} h^{-1}) from the photocatalyst system at cutting edge technology is a primary challenge to develop the closed-loop artificial photosynthetic system.

Improving catalysts research categorizes into three main parts: 1) design catalysts and test catalysis, 2) characterize catalysts and catalysis, 3) proving the catalysis principle. The balanced those three parts have made significant progress in catalysts research. #1 and #2 depends on in-situ and ex-situ experiments. The proving principle is mainly based on quantum mechanic theory because catalysis is all at the atomic scale. However, there is always a gap between complex experimental catalysis and simple theoretical quantum mechanics because we can take only a small part of experimental data for modeling quantum mechanics and stipulate experimental variations as fixed.

Thus, we can understand parts of catalysis or misunderstand catalysis, which are chronic problems in catalysts research. Embodying all possible experimental variables of catalysis into

quantum mechanics theory is a solution to reduce the gap between experiments and theory. However, the computational capacity and required calculation time at the current level theory limit the numbers of considering variables in quantum mechanics theory. The effective way to establish feasible quantum mechanics calculations as experimental environments scales is to divide experiments into small pieces of quantum mechanics conditions. Furthermore, by combining the experimentally confirmed quantum mechanics data into a whole complete piece again, we can reflect all possible experimental variables in quantum mechanics theory. Deep learning could be a method to build the entire work from divided small pieces of quantum mechanics data and experimental data. The well developed deep learning model could directly correlate the anticipation from quantum mechanics theory with complex experimental conditions. This model will uncover the hidden catalysis reactions and variables, enhancing our understanding of the complicated CO_2 conversion reaction. Thus, the trained deep learning model could drive challenging photocatalyst for the artificial photosynthetic system to the well organized industrial level photocatalysis because the chance to solve scientific issues of catalysis has taken root in the level of understanding them.